

Příloha č. 1 – Spoluautorská publikace

Čermák, V.; Gandalovičová, A.; Merta, L.; Fučíková, J.; Špišek, R.; Rösel, D.; Brábek, J.
RNA-seq of macrophages of amoeboid or mesenchymal migratory phenotype due to
specific structure of environment. *Sci. Data* **2018**, *5*, 180198.

5-letý impakt faktor dle Web of Science: 7,670

Krátké shrnutí obsahu publikace:

V této práci byla provedena transkriptomická analýza M2 makrofágů v 3D prostředí kolagenové matrix pomocí RNA-seq metody s využitím IlluminaHiSeq. Zvolené buňky k migraci využívají mezenchymální nebo améboidní mód invazivity v závislosti na koncentraci použitého kolagenu. Při koncentraci kolagenu 1,7 mg/ml („řidký kolagen“) zaujímají makrofágy améboidní morfologii, při koncentraci 4,8 mg/ml („hustý kolagen“) pak morfologii mezenchymální.

Jelikož se jedná o článek v časopise Scientific Data, byl důraz kladen hlavně na důkaz kvality ve všech krocích postupu přípravy vzorků, aby bylo možné konstatovat, že uložená transkriptomická data jsou spolehlivá. Data jsou veřejně přístupná v databázi ArrayExpress pod kódem E-MTAB-6643.

V rámci ověření transkriptomických výsledků byla provedena validace třech vybraných cílů pomocí metody RT-qPCR. Tyto cíle reprezentovaly jak sekvence kódující proteiny (ITGB3 a CD74), tak dlouhé nekódující RNA – konkrétně MALAT1. Hladina integrinu $\beta 3$ (ITGB3) byla zvýšena při améboidní migraci stejně jako úroveň exprese lncRNA MALAT1. Naopak protein CD74 (má funkci při formování a transportu antigen prezentujícího komplexu MHC glykoproteinu třídy II) měl expresi v améboidní formě makrofágů sniženu. Výsledky vykazovaly stejný expresní profil s využitím obou metod (RNA-seq a RT-qPCR), metoda RT-qPCR však zaznamenala vyšší rozdíly než metoda RNA-seq.

SCIENTIFIC DATA

OPEN

Data Descriptor: RNA-seq of macrophages of amoeboid or mesenchymal migratory phenotype due to specific structure of environment

Received: 12 April 2018
Accepted: 26 July 2018
Published: 2 October 2018

Vladimír Čermák^{1,2}, Aneta Gandalovičová^{1,2}, Ladislav Merta^{1,2}, Jitka Fučíková^{3,4}, Radek Špišák^{3,4}, Daniel Rösel^{1,2} & Jan Brábek^{1,2}

M2-polarized macrophages have been shown to adapt their 3D migration mode to physical properties of surrounding extracellular matrix. They migrate in the integrin-mediated adhesion and proteolytic activity-dependent “mesenchymal” mode in stiff matrices and in the integrin and protease-independent “amoeboid” mode in low density, porous environments. To find out what impact the switching between the migration modes has on expression of both protein-coding and non-coding genes we employed RNA sequencing of total RNA depleted of ribosomal RNA isolated from macrophages migrating in either mode in 3D collagens. Differentially expressed genes from both categories have been detected and the changes in expression of selected genes were further validated with RT-qPCR. The acquired data will facilitate better understanding of how mechanical properties of tissue microenvironment reflect in macrophage immune function and how the transitions between mesenchymal and amoeboid migratory modes are regulated at the gene expression level.

Design Type(s)	factorial design • transcription profiling design
Measurement Type(s)	transcription profiling assay
Technology Type(s)	RNA sequencing
Factor Type(s)	Blood Donor • collagen-containing extracellular matrix
Sample Characteristic(s)	Homo sapiens • macrophage

¹Department of Cell Biology, Charles University, Viničná 7, Prague, Czech Republic. ²Biotechnology and Biomedicine Centre of the Academy of Sciences and Charles University (BIOCEV), Průmyslová 595, 25242, Vestec u Prahy, Czech Republic. ³Department of Immunology, Charles University, 2nd Faculty of Medicine and University hospital Motol, Prague, Czech Republic. ⁴Sotio, Prague, Czech Republic. Correspondence and requests for materials should be addressed to J.B. (email: jan.brabek@natur.cuni.cz)

Background & Summary

Cell invasion is required for many physiological processes such as development, immune response or wound healing, and, in effect, many cell types possess the capability to invade¹. Immune cells have developed very effective invasion strategies that enable them to perform immune surveillance even deep in tissues. However, cell invasion also facilitates dangerous pathological states such as cancer metastasis, and cancer cells are often considered to be masters of invasion. A key feature underlying effective invasion, shared by both immune cells and cancer cells, is the ability to adapt to different conditions by adjusting the mode of invasion, often referred to as invasion plasticity^{2–5}.

The various invasion modes cells can adopt include two distinct individual invasion modes – the protease-dependent mesenchymal mode and protease-independent amoeboid mode. Generally, mesenchymal migration relies on the formation of adhesions to the extracellular matrix (ECM) and proteolytic degradation of adjacent fibres^{6,7}. On the contrary, amoeboid cells do not rely on fibre degradation and instead dynamically deform their cell body (including the nucleus), to squeeze through pores in the ECM^{8,9}. These invasion modes are interchangeable and cells can undergo the mesenchymal-amoeboid (MAT) or amoeboid-mesenchymal transitions (AMT) in response to intracellular and/or extracellular cues^{6,10–14}. While processes of MAT and AMT in cancer cells have been extensively studied during the past years, little information is available on the molecular mechanisms behind the invasion plasticity of immune cells^{3,15}.

An elaborate study by Cougole *et al.* tested the invasion plasticity of various immune cells in response to different ECM conditions and showed that these cells differ in their capability to adjust to soft or stiff matrices. They conclude that all leukocytes use the amoeboid mode, but only M2 macrophages possessed the ability to adjust their morphology according to the extracellular matrix conditions and switch between the amoeboid and mesenchymal phenotype¹⁵.

This phenomenon was described in detail by Van Goethem *et al.*, which showed that M2 macrophages modulate their invasion mode according to the ECM architecture³. In Matrigel and gelled collagen, both dense environments with small pores, M2 macrophages utilize the mesenchymal mode and form podosomes – membrane protrusions with proteolytic activity. Interestingly, this invasion mode can be inhibited by a protease inhibitor mix, but not by a selective inhibitor of matrix metalloproteinases alone, indicating other proteases to be involved. Moreover, protease inhibition does not result in MAT, as described in cancer cells. In fibrillar collagen, which permits cells to take advantage of larger pre-existing pores, macrophages are amoeboid and do not form podosomes. Amoeboid macrophage invasion is unaffected by protease inhibitors but is decreased in the presence of ROCK inhibitors, which is in line with observations of amoeboid cancer cells.

To elucidate signalling driving this invasion adaptability of macrophages and potentially reveal candidate marker genes of the amoeboid and mesenchymal phenotype, we performed RNA sequencing of three independent primary samples of human M2-polarized macrophages embedded in both low and high-density collagen (Fig. 1), as described by Van Goethem *et al.*³ In agreement with their results, if we embedded M2 macrophages in 1.7 mg/ml collagen, they adopted the amoeboid phenotype in over 86% (SE 4.36%). In dense collagen (4.8 mg/ml), the majority (83%, SE 2.65%) of macrophages was mesenchymal (Fig. 2). To verify the migratory potential of both amoeboid and mesenchymal macrophage invasion modes, we performed time-lapse live cell imaging. Supplementary videos clearly demonstrate amoeboid locomotion in fibrillar collagen (Macrophage phenotype in fibrillar collagen, Data Citation 1) and document mesenchymal invasion of M2 macrophages in high-density environment (Macrophage phenotype in dense collagen, Data Citation 1).

A substantial advantage of primary M2 macrophages as a model system is their inherent invasion plasticity that enables to study mechanisms of MAT and AMT without any genetic manipulation or chemical treatment. The presented data will help to better comprehend the *in vivo* plasticity of cellular invasion caused by ECM diversity. In addition, analysis of the data revealed that the immune function of macrophages is also affected by mechanical properties of the ECM, hence reuse of the data by the immunological community could be beneficial.

Methods

Differentiation and M2 polarization of primary human macrophages

Primary human macrophages derived from CD14⁺ subpopulation of peripheral blood mononuclear cells from healthy donors aged between 25–40 years were differentiated and M2-polarized with M-CSF (100 ng/ml) in RPMI-1640 medium supplemented with 10% fetal bovine serum for 5–6 days before the experiments. Informed consent was obtained from all subjects. The experiments were approved by the Ethical Committee of the Second Faculty of Medicine at Charles University in Prague.

Three-dimensional cell culture and RNA isolation

Five million M2 macrophages were cultured in 500 µl of three-dimensional gel made of bovine skin collagen (Nutragen, Advanced BioMatrix, 1.7 or 4.8 mg/ml) in RPMI-1640 with 1% fetal bovine serum and 100 ng/ml M-CSF (Peprotech) for 48 hours in a 24-well plate. Gels from two wells were transferred into one 2 ml tube and homogenized with Tissue Tearor (BioSpec Products) in 600 µl of RNA extraction solution (60% v/v water-saturated phenol, 3.25 M guanidine thiocyanate, 400 mM sodium acetate buffer pH 4.0, 0.4% w/v N-lauroylsarcosine, 160 mM 2-mercaptoethanol) plus 100 µl of 6.1 M sodium chloride.

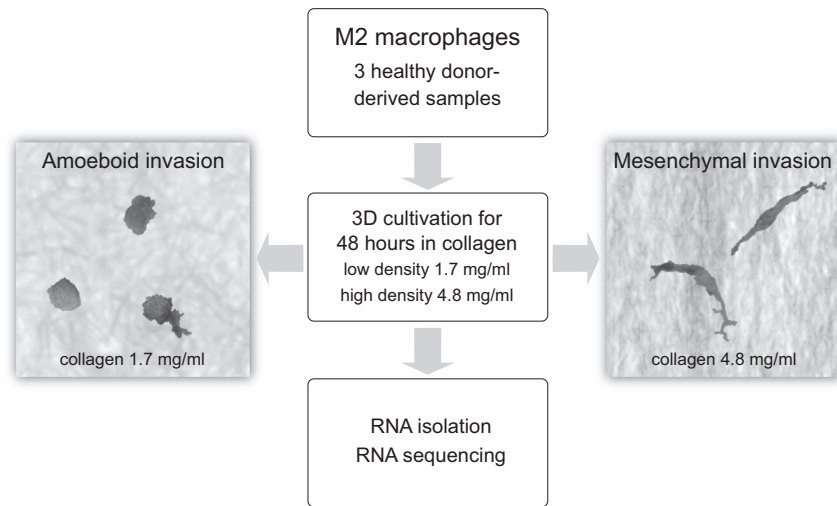


Figure 1. Schematic overview and experimental design of the study.

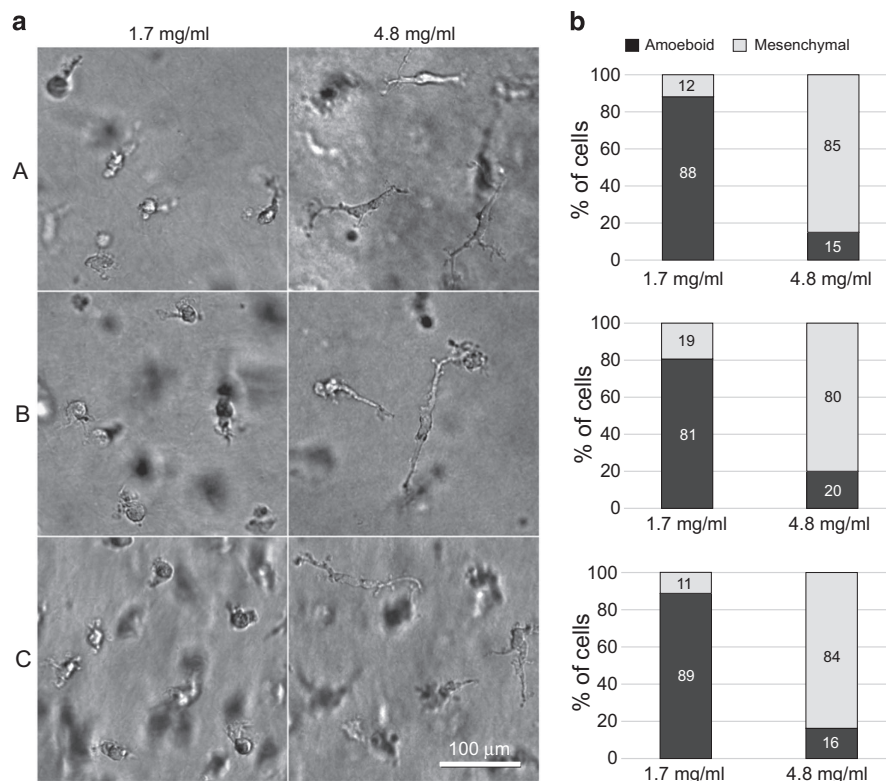


Figure 2. Morphology analysis of M2 macrophage samples embedded in low- and high-density collagen.

(a) Representative images of the three analysed samples of M2 macrophages (A–C) embedded in 1.7 mg/ml or 4.8 mg/ml collagen. Images were acquired using Nikon-Eclipse TE2000-S, 10x objective with Hoffman modulation contrast. (b) Quantification of cell phenotype of the three analysed samples of M2 macrophages (a–c) embedded in 1.7 mg/ml or 4.8 mg/ml collagen.

200 μ l of chloroform was added to approx. 1 ml of the lysate and the mixture was vortexed vigorously for 10 seconds. After 30-minute centrifugation at 18,000 g at 4 $^{\circ}$ C, the polar upper phase was transferred into a new tube, volume adjusted to 800 μ l with RNase-free water, RNA was precipitated with 600 μ l of isopropanol at –20 $^{\circ}$ C overnight and recovered by centrifugation at 18,000 g for 30 minutes at 4 $^{\circ}$ C. The RNA pellet was washed three times with 600 μ l of 75% ethanol and air-dried. Next, the RNA was treated with DNase I to remove possible genomic DNA contamination. To this end, the pellet was

Subjects	Gender	Condition	Protocols	ENA	BioSD
Donor A	male	1.7 mg/ml collagen	P-MTAB-73510 to P-MTAB-73516	ERS2359742	SAMEA1054135
Donor A	male	4.8 mg/ml collagen	P-MTAB-73510 to P-MTAB-73516	ERS2359739	SAMEA1054132
Donor B	female	1.7 mg/ml collagen	P-MTAB-73510 to P-MTAB-73516	ERS2359743	SAMEA1054136
Donor B	female	4.8 mg/ml collagen	P-MTAB-73510 to P-MTAB-73516	ERS2359740	SAMEA1054133
Donor C	male	1.7 mg/ml collagen	P-MTAB-73510 to P-MTAB-73516	ERS2359744	SAMEA1054137
Donor C	male	4.8 mg/ml collagen	P-MTAB-73510 to P-MTAB-73516	ERS2359741	SAMEA1054134

Table 1. Summary of sequencing data.

directly dissolved in 100 μ l of a solution containing 4 units of DNase I (Thermo Fisher Scientific) and manufacturer-provided reaction buffer, and incubated at 37 °C for 30 minutes. After that, the RNA was re-purified with RNeasy Protect Mini Kit (Qiagen) according to the manufacturer's instructions and eluted in 50 μ l of RNase-free water (Invitrogen).

Analysis of cell morphology in 3D collagen

Cell morphology was analysed with ImageJ software by measuring longest axis to shortest axis ratios. Cells with the ratio equal to 2.5 or larger were considered mesenchymal, as determined earlier by Van Goethem *et al.*³. For each condition a minimum of 100 cells was analysed.

RNA sequencing and data processing

Stranded, Illumina HiSeq-compatible library was constructed with ScriptSeq Complete (Human/Mouse/Rat) library preparation kit (Epicentre) according to the manufacturer's instructions. An equimolar pool of 6 sample libraries (three donor-matched pairs) was sequenced on one whole lane of Illumina HiSeq 2500 sequencer in high output, paired (2 \times 125 cycles) mode by Beckman Coulter Genomics.

Raw reads were trimmed of adapter sequences with Cutadapt¹⁶ (version 1.15) and mapped to human genome version GRCh38.91 with the STAR short read aligner¹⁷ version 2.5.4b with default settings and output extended with read counts per gene.

Adapter-trimmed reads were deposited in the ArrayExpress database (Data Citation 2). The samples and related files are summarized in Table 1.

Differential Gene Expression Analysis

To find differentially expressed genes R package DESeq2¹⁸ (version 1.18.1) was used with the raw read count output of the STAR aligner as the input. Default workflow with a design formula reflecting paired nature of the samples was applied. Differentially expressed genes with FDR < 0.1 (874 upregulated and 1,676 downregulated genes) are available in the file Differentially_expressed_genes.xlsx (Data Citation 1) and their distribution by gene expression level is depicted as MA plot in Fig. 3d. Principle component analysis of the gene expression profiles showed dominant clustering of the samples by individual donors (Fig. 3e). This obviously reflects the well-known high variation of primary cell samples that can much exceed the variation brought about by experimental treatment as in this case. The use of two-factor design (cell donor and collagen concentration) in the statistical analysis is thus crucial.

Analysis of ribosomal cDNA content and strandedness of libraries

Adapter-trimmed reads were mapped to human ribosomal RNA coding sequences (NR_023379, NR_003285, NR_003286, NR_003287, NR_137294, and NR_137295) with BMap aligner¹⁹ in local alignment mode. Ribosomal cDNA content in the libraries was expressed as percentage of reads mapped to nuclear or mitochondrial rRNA transcripts (the larger number from the paired mates). Strandedness of libraries was assessed from ratios of read counts mapped (by STAR) to annotated genomic loci in sense and antisense orientation. To eliminate the noise associated with low-expressed genes we limited the calculations to genes with lognormal mean or higher expression (approx. 6,000 genes). We also excluded genes with more antisense transcripts than those in sense orientation. The mean sense/antisense ratio was calculated as a geometric mean of all included gene ratios across all samples.

Reverse Transcription – Quantitative polymerase chain reaction (RT-qPCR)

All the RT-qPCR experiments were performed according to MIQE guidelines²⁰. Briefly, total RNA was extracted from cells embedded in 3D collagen matrix as described above. RNA reverse transcription was performed using M-MuLV Reverse Transcriptase (NEB) with 1 μ M oligo-dT and 0.2 μ M MALAT1-specific primer and 700 ng of total RNA. RT-qPCR was performed using SYBR green mix (1x Standard Taq buffer (NEB) with 3.0 mM MgCl₂, 2 U/100 μ l Hot Start Taq DNA Polymerase (NEB), 10% glycerol (Carl Roth), 6% DMSO (Sigma), 200 μ M dNTPs (Thermo Fischer Scientific), 0.05% Triton X-100 (Sigma), 1x SYBR® Green I Nucleic Acid Stain (Lonza), and Ultrapure Water (Invitrogen)) and CFX384 Real Time PCR Instrument (Bio-Rad). Annealing and elongation temperatures were 63 °C and 68 °C, respectively. The RT-qPCR reaction volume was 10 μ l with 0.5 μ l of cDNA and 200 nM primers (for

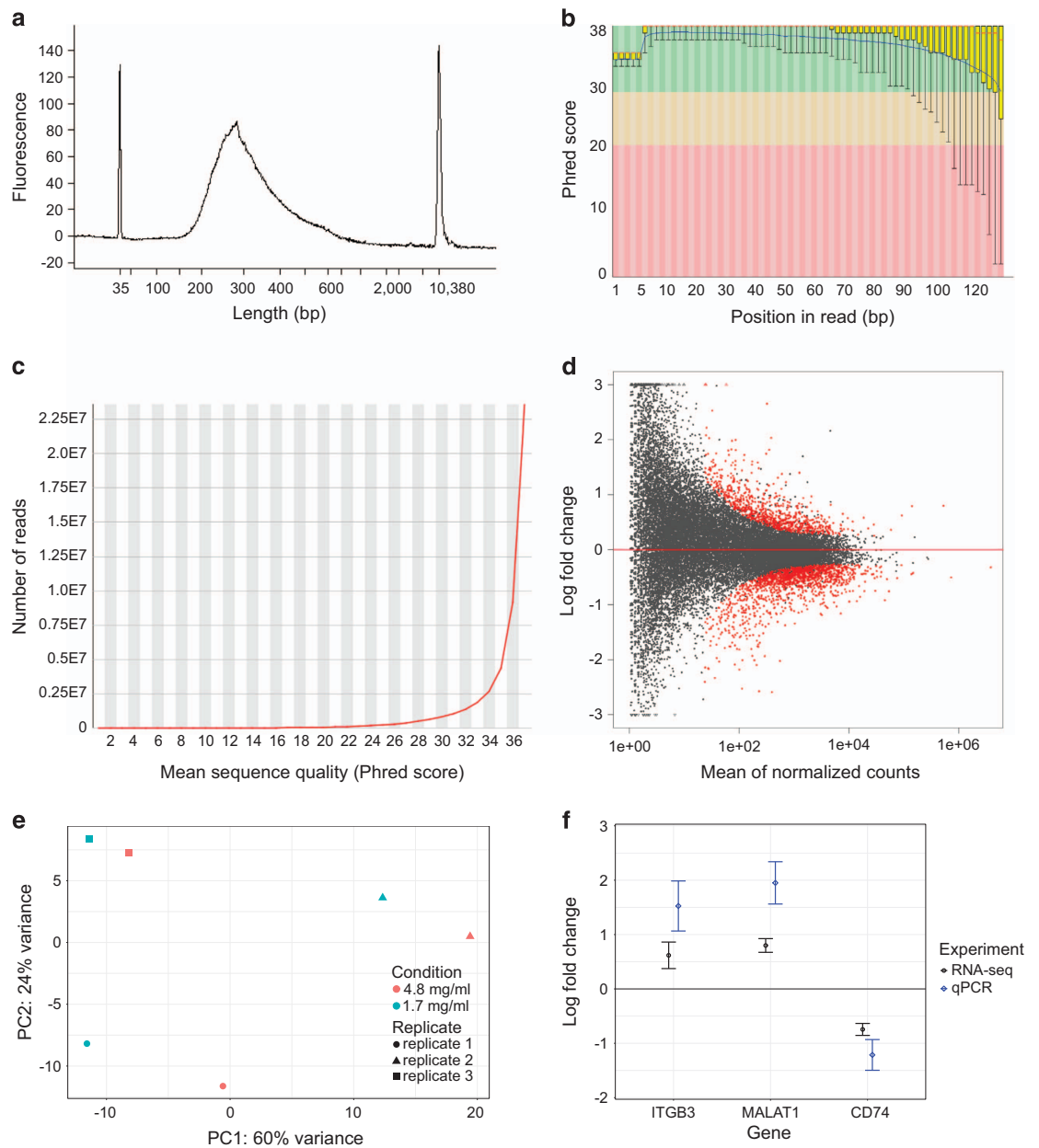


Figure 3. RNA-seq results validation. (a) Sequencing library fragment size distribution of sample 1. (b) Per base sequence quality expressed as Phred score by position, sample 1, first reads. (c) Quality score distribution over all reads of sample 1. (d) MA plot of log₂ fold change values against normalized counts for each gene in the analysis. Red points mark genes with FDR < 0.1. (e) Principal component analysis of gene expression profiles. (f) Comparison of log₂ fold change values detected by RNA-seq and RT-qPCR, respectively for the indicated genes.

primer details see Table 2). Samples were run as technical quadruplicates using FrameStar® 480/384 with RT-qPCR Adhesive seal (4titude) 384-well plates. C_q and relative expression values were calculated by setting single threshold value for each target and further analysed by qBase + software (Biogazelle)²¹ using EIF4H, HNRNPL and PPIA as reference gene index (based on geNORM analysis²²). Amplification efficiencies were determined by the standard curve analysis. Log₂ fold change values were calculated from relative expression values.

Data Records

Time-lapse movies documenting migratory phenotypes of the cells and a table listing all the differentially expressed genes detected in the study were deposited in the Figshare repository (Data Citation 1).

RNA-seq data have been deposited in the ArrayExpress database at EMBL-EBI (Data Citation 2).

Transcript	Acc. Number	Primer	Sequence	Product (bp)	Eff. (%)
MALAT1	NR_002819	MALAT1_5s	GAATTGCGTCATTTAAAGCCTA	85	92.2
		MALAT1_5a	GTTTCATCCTACCACTCCCAAT		
ITGB3	NM_002211	ITGB3f	CACCATCCACGACCGAAAAG	82	99.5
		ITGB3r	CAGTGGGTTGTTGGCTGTGT		
CD74	NM_001025159	CD74f	GGAAGGCTTTGAGAGCTGGAT	114	111.0
		CD74r	CTTCTGGCACTGGTCAGTA		
HNRNPL	NM_001533	HNRNPLs	CTGGAGGTGACCGAGGAGAA	96	99.3
		HNRNPLa	GCGCTCACTTTTGCCTGAGAA		
EIF4H	NM_022170	EIF4Hs	CTTCGACACCTACGACGATCG	95	97.7
		EIF4Ha	CCTTCTGGCTACGGGAACCAT		
PPIA	NM_021130	PPIAf	GCCGAGGAAAACCGTACTA	106	94.1
		PPIAr	CTGCAACAGCTCAAAGGAGAC		

Table 2. Primers used for RT-qPCR.

Sample		Nuclear-encoded rRNA	Mitochondrial rRNA
Donor A	1.7 mg/ml collagen	0.9%	9.5%
	4.8 mg/ml collagen	0.7%	11.8%
Donor B	1.7 mg/ml collagen	0.3%	9.8%
	4.8 mg/ml collagen	0.4%	16.0%
Donor C	1.7 mg/ml collagen	1.1%	11.0%
	4.8 mg/ml collagen	0.6%	13.5%

Table 3. Percentage of rRNA matching reads in RNA-seq data.

Technical Validation

Viability and morphological phenotype of the cells was verified by wide field microscopy (Fig. 2). The integrity of isolated total RNA was confirmed with agarose gel electrophoresis of denatured RNA samples. The quality and size distribution of sequencing libraries was analysed with Agilent BioAnalyzer 2100 (Fig. 3a). The profiles, according to expectation, showed peak position around 280 bp and a longer right tail. The output statistics of STAR aligner showed an average paired read length of 230 bases. Raw reads trimmed of adapter sequences, approx. 2×40 million reads per sample, were quality-checked with FastQC software²³. FastQC's plots of Phred scores by position (Fig. 3b) showed typical profiles with decreasing quality towards the ends of reads. The overall quality was analysed with BBTools' Reformat utility¹⁹ detecting approx. 91% bases having Phred score 30 or better. The distribution of quality scores is presented in Fig. 3c. Figure 3 displays quality assessment results for sample 1. Complete results for all six samples are provided in Supplementary Figure 1. FastQC analysis also detected a significant presence of duplicate reads, which was expected as the library construction involved a PCR amplification step. The STAR aligner uniquely mapped approx. 90% of the fragments to human genome, approx. 6% fragments were multi-mapped, and approx. 4% fragments were excluded as too short. We further analysed residual rRNA content after ribodepletion expressed as proportion of reads mapped to rRNA sequences. Only 0.3–1.1% reads could be mapped to nuclear encoded rRNA. However, 9.5–16% of all reads were mapped to mitochondrial 12S and 16S rRNA sequences with higher mtrRNA content in all high-concentration collagen samples (Table 3). The Ribo-Zero component of the library construction kit used in this work does not deplete total RNA of mitochondrial rRNA, so this is not unexpected.

The libraries were prepared as strand-specific. To analyse the level of strandedness in the sequencing data we compared proportions of sense and antisense reads mapped to known genes of intermediate to high expression. The average sense/antisense ratio was 18.4 ± 1.87 (geometric mean and standard deviation). This might appear slightly less than expected, however a few factors lowering apparent strandedness should be taken into account. The ribodepleted total RNA is much more complex than mRNA isolated with oligo-dT probes. It contains unprocessed primary transcripts that may partly span neighbouring genes in opposite orientation. It also contains large proportion of non-coding sequences

that sometimes arise from antisense transcription of coding genes. Another source of partial loss of strandedness is the DNA-dependent DNA polymerase activity of reverse transcriptase.

To validate the results of differential gene expression analysis, RT-qPCR was performed with the RNA samples used for sequencing to compare changes in expression of three selected genes – ITGB3, MALAT1 and CD74 as detected by RNA-seq and RT-qPCR. These genes were chosen in order to represent different functional categories (cell adhesion, antigen presentation) and also both protein-coding and non-coding (MALAT1) genes. The results showed essentially the same expression pattern with RT-qPCR detecting greater fold-changes than RNA-seq (Fig. 3f).

References

- Binamé, F., Pawlak, G., Roux, P. & Hibner, U. What makes cells move: requirements and obstacles for spontaneous cell motility. *Mol. Biosyst.* **6**, 648–661 (2010).
- Friedl, P. & Alexander, S. Cancer invasion and the microenvironment: plasticity and reciprocity. *Cell* **147**, 992–1009 (2011).
- Van Goethem, E., Poincloux, R., Gauffre, F., Maridonneau-Parini, I. & Le Cabec, V. Matrix architecture dictates three-dimensional migration modes of human macrophages: differential involvement of proteases and podosome-like structures. *J. Immunol.* **184**, 1049–1061 (2010).
- Taddei, M. L., Giannoni, E., Comito, G. & Chiarugi, P. Microenvironment and tumor cell plasticity: an easy way out. *Cancer Lett.* **341**, 80–96 (2013).
- Charras, G. & Sahai, E. Physical influences of the extracellular environment on cell migration. *Nat. Rev. Mol. Cell Biol.* **15**, 813–824 (2014).
- Wolf, K. *et al.* Compensation mechanism in tumor cell migration: mesenchymal-amoeboid transition after blocking of pericellular proteolysis. *J. Cell Biol.* **160**, 267–277 (2003).
- Nagano, M., Hoshino, D., Koshikawa, N., Akizawa, T. & Seiki, M. Turnover of focal adhesions and cancer cell migration. *Int. J. Cell Biol.* **2012**, 310616 (2012).
- Lämmermann, T. & Sixt, M. Mechanical modes of ‘amoeboid’ cell migration. *Curr. Opin. Cell Biol.* **21**, 636–644 (2009).
- Charras, G. & Paluch, E. Blebs lead the way: how to migrate without lamellipodia. *Nat. Rev. Mol. Cell Biol.* **9**, 730–736 (2008).
- Friedl, P. & Wolf, K. Plasticity of cell migration: a multiscale tuning model. *J. Cell Biol.* **188**, 11–19 (2010).
- Liu, Y. J. *et al.* Confinement and low adhesion induce fast amoeboid migration of slow mesenchymal cells. *Cell* **160**, 659–672 (2015).
- Paňková, K., Rösel, D., Novotný, M. & Brábek, J. The molecular mechanisms of transition between mesenchymal and amoeboid invasiveness in tumor cells. *Cell. Mol. Life Sci.* **67**, 63–71 (2010).
- Paňková, D. *et al.* NG2-mediated Rho activation promotes amoeboid invasiveness of cancer cells. *Eur. J. Cell Biol.* **91**, 969–977 (2012).
- Ladhani, O., Sanchez-Martinez, C., Orgaz, J. L., Jimenez, B. & Volpert, O. V. Pigment epithelium-derived factor blocks tumor extravasation by suppressing amoeboid morphology and mesenchymal proteolysis. *Neoplasia* **13**, 633–642 (2011).
- Cougoule, C. *et al.* Blood leukocytes and macrophages of various phenotypes have distinct abilities to form podosomes and to migrate in 3D environments. *Eur. J. Cell Biol.* **91**, 938–949 (2012).
- Martin, M. Cutadapt removes adapter sequences from high-throughput sequencing reads. *EMBnet.journal* **17**, 10–12 (2011).
- Dobin, A. *et al.* STAR: ultrafast universal RNA-seq aligner. *Bioinformatics* **29**, 15–21 (2013).
- Love, M. I., Huber, W. & Anders, S. Moderated estimation of fold change and dispersion for RNA-seq data with DESeq2. *Genome Biol.* **15**, 550 (2014).
- Bushnell, B. BBTools software package. BBTools - DOE Joint Genome Institute <https://jgi.doe.gov/data-and-tools/bbtools> (2014).
- Bustin, S. A. *et al.* The MIQE Guidelines: Minimum Information for Publication of Quantitative Real-Time PCR Experiments. *Clin. Chem.* **55**, 611–622 (2009).
- Hellemans, J., Mortier, G., De Paepe, A., Speleman, F. & Vandesompele, J. qBase relative quantification framework and software for management and automated analysis of real-time quantitative PCR data. *Genome Biol.* **8**, R19 (2007).
- Vandesompele, J. *et al.* Accurate normalization of real-time quantitative RT-PCR data by geometric averaging of multiple internal control genes. *Genome Biol.* **3**, research0034.1–0034.11 (2002).
- Andrews, S. FastQC: a quality control tool for high throughput sequence data. *Babraham Bioinformatics* <https://www.bioinformatics.babraham.ac.uk/projects/fastqc> (2010).

Data Citations

- Čermák, V. *et al.* *figshare* <https://doi.org/10.6084/m9.figshare.c.4140770> (2018).
- ArrayExpress* E-MTAB-6643 (2018).

Acknowledgements

This work was funded by Czech Science Foundation grant 18-15684J, by the Charles University, project GA UK No 712217 and 1292217, by the Ministry of Education, Youth and Sports of CR within the LQ1604 National Sustainability Program II (Project BIOCEV FAR) and by the project “BIOCEV” (CZ.1.05/1.1.00/02.0109). We acknowledge the IMCF at BIOCEV supported by the MEYS CR (LM2015062 Czech BioImaging). We acknowledge the BIOCEV Gene Core facility. This publication is a result of the project implementation: “The equipment for metabolomic and cell analyses”, registration number CZ.1.05/2.1.00/19.0400, supported by Research and Development for Innovations Operational Programme (RDIOP) co-financed by European regional development fund and the state budget of the Czech Republic.

Author Contributions

V.Č. prepared sequencing libraries and analysed the data. A.G. performed 3D cell culture experiments. L.M. performed RT-qPCR experiments. J.F. prepared human donor-derived macrophages. R.Š. conceived the study and supervised experiments. D.R. conceived the study and supervised experiments. J.B. conceived the study and supervised experiments. All authors reviewed the manuscript.

Additional Information

Supplementary information accompanies this paper at <http://www.nature.com/sdata>

Competing interests: The authors declare no competing interests.

How to cite this article: Čermák, V. *et al.* RNA-seq of macrophages of amoeboid or mesenchymal migratory phenotype due to specific structure of environment. *Sci. Data.* 5:180198 doi: 10.1038/sdata.2018.198 (2018).

Publisher's note: Springer Nature remains neutral with regard to jurisdictional claims in published maps and institutional affiliations.



Open Access This article is licensed under a Creative Commons Attribution 4.0 International License, which permits use, sharing, adaptation, distribution and reproduction in any medium or format, as long as you give appropriate credit to the original author(s) and the source, provide a link to the Creative Commons license, and indicate if changes were made. The images or other third party material in this article are included in the article's Creative Commons license, unless indicated otherwise in a credit line to the material. If material is not included in the article's Creative Commons license and your intended use is not permitted by statutory regulation or exceeds the permitted use, you will need to obtain permission directly from the copyright holder. To view a copy of this license, visit <http://creativecommons.org/licenses/by/4.0/>

The Creative Commons Public Domain Dedication waiver <http://creativecommons.org/publicdomain/zero/1.0/> applies to the metadata files made available in this article.

© The Author(s) 2018

Příloha č. 2 – Ko-prvoautorská publikace

Čermák, V.*; Gandalovičová, A.*; Merta, L.*; Harant, K.; Rösel, D.; Brábek, J. High-throughput Transcriptomic and Proteomic Profiling of Mesenchymal-Amoeboid Transition in 3D Collagen. *Sci. Data* **2020**, 7, 160.

5-letý impakt faktor dle Web of Science: 7,670

* takto označení autoři přispěli stejným dílem k práci na článku

Krátké shrnutí obsahu publikace:

V této práci byl představen námi zavedený model pro analýzu MAT ve 3D prostředí kolagenové matrix. Vytvořili jsme buněčnou linii odvozenou od fibrosarkomové linie HT1080 (ve 3D prostředí vykazuje výraznou mezenchymální morfologii), ve které bylo možné indukovat konstitutivně aktivní RhoA (icaRhoA) po indukci buněk doxycyklinem. Jako komplementární přístup pro vyvolání MAT bylo zvoleno použití inhibitoru dasatinibu (inhibuje kinázu Src zásadní pro formování fokálních adhezí typických pro mezenchymální invazivitu). Oba modely byly nejprve charakterizovány a byla prezentována jejich funkčnost. Dále byla prezentována transkriptomická a proteomická data získaná s využitím popsaných experimentálních modelů ve 3D prostředí.

Jelikož se jedná o článek v časopise Scientific Data, byl důraz kladen hlavně na důkaz kvality ve všech krocích postupu přípravy vzorků, aby bylo možné konstatovat, že uložená transkriptomická i proteomická data jsou spolehlivá. Transkriptomická data jsou veřejně přístupná v databázi ArrayExpress pod kódem E-MTAB-6823, proteomická data jsou přístupná v databázi PRIDE pod kódem PXD010425.



V závěrečné části publikace jsou graficky prezentovány cíle se signifikantně změněnou (sníženou či zvýšenou) expresí na úrovni transkriptů či proteinů. Změny exprese vybraných cílů byly z technického hlediska ověřeny pomocí imunoblotů.



OPEN

DATA DESCRIPTOR

High-throughput transcriptomic and proteomic profiling of mesenchymal-amoeboid transition in 3D collagen

Vladimír Čermák^{1,2,4}, Aneta Gandalovičová^{1,2,4}, Ladislav Merta^{1,2,4}, Karel Harant^{2,3}, Daniel Rösel^{1,2} & Jan Brábek^{1,2}  

The plasticity of cancer cell invasion represents substantial hindrance for effective anti-metastatic therapy. To better understand the cancer cells' plasticity, we performed complex transcriptomic and proteomic profiling of HT1080 fibrosarcoma cells undergoing mesenchymal-amoeboid transition (MAT). As amoeboid migratory phenotype can fully manifest only in 3D conditions, all experiments were performed with 3D collagen-based cultures. Two previously described approaches to induce MAT were used: doxycycline-inducible constitutively active RhoA expression and dasatinib treatment. RNA sequencing was performed with ribo-depleted total RNA. Protein samples were analysed with tandem mass tag (TMT)-based mass spectrometry. The data provide unprecedented insight into transcriptome and proteome changes accompanying MAT in true 3D conditions.

Background & Summary

Cancer is the result of deregulation of cellular processes, namely of cell proliferation, differentiation, survival/apoptosis, metabolism and migration¹. Aberrant invasive behaviour of cancer cells can result in metastasis, a process responsible for tumour dissemination and related mortality, accounting for approx. 90% deaths from cancer. Using ancient, evolutionary conserved mechanisms, cancer cells invade the extracellular matrix (ECM) either as cell clusters or sheets, described as collective invasion, or alternatively, migrate as individual cells². When migrating individually, cells can adopt either the protease-dependent mesenchymal mode or the protease-independent amoeboid mode. In general, mesenchymally invading cells display a fibroblast-like morphology with a distinct leading and trailing edge³. They form actin-rich protrusions that engage in stable cell-ECM contacts mediated mostly by integrins⁴. Mesenchymal cells further form invasive structures, such as invadopodia and podosomes, that produce proteolytically active enzymes, most commonly matrix metalloproteinases^{5,6}. The secretion of such enzymes serves to digest the surrounding ECM and form tracks large enough for cell body translocation⁷.

Unlike mesenchymal invasion, amoeboid invasion does not fully depend on proteolytic digestion and formation of stable cell-ECM adhesions. The cells rather take advantage of pre-existing pores in the ECM and dynamically change their cell body to squeeze through^{8,9}. Amoeboid cells may display enhanced actomyosin contractility due to persistent activation of the RhoA/ROCK pathway, leading to increased hydrostatic pressure that drives formation of membrane blebs^{10,11}. However, a few different subtypes of the amoeboid migratory phenotype have been described and diverse theories explaining the physical mechanism of cell translocation in amoeboid cells have been suggested¹². So far, no specific biochemical marker of the phenotype has been shown to be a universal feature of amoeboid cells arising from different cell types. Importantly, cancer cell invasion is responsive to surrounding conditions and transitions between the individual modes can occur. The mesenchymal-amoeboid (MAT) or amoeboid-mesenchymal (AMT) transitions can be induced by modulating the activity of key signalling hubs, such as the Rho GTPases, or by targeting necessary mechanisms of either invasion mode^{13,14}. The plasticity of invasion is presumably the main reason why clinically usable anti-metastatic treatment strategies are

¹Department of Cell Biology, Charles University, Viničná 7, Prague, Czech Republic. ²Biotechnology and Biomedicine Centre of the Academy of Sciences and Charles University (BIOCEV), Průmyslová 595, 25242, Vestec u Prahy, Czech Republic. ³Proteomics Core Facility, Faculty of Science, Charles University, Prague, Czech Republic. ⁴These authors contributed equally: Vladimír Čermák, Aneta Gandalovičová, Ladislav Merta. ✉e-mail: jan.brabek@natur.cuni.cz

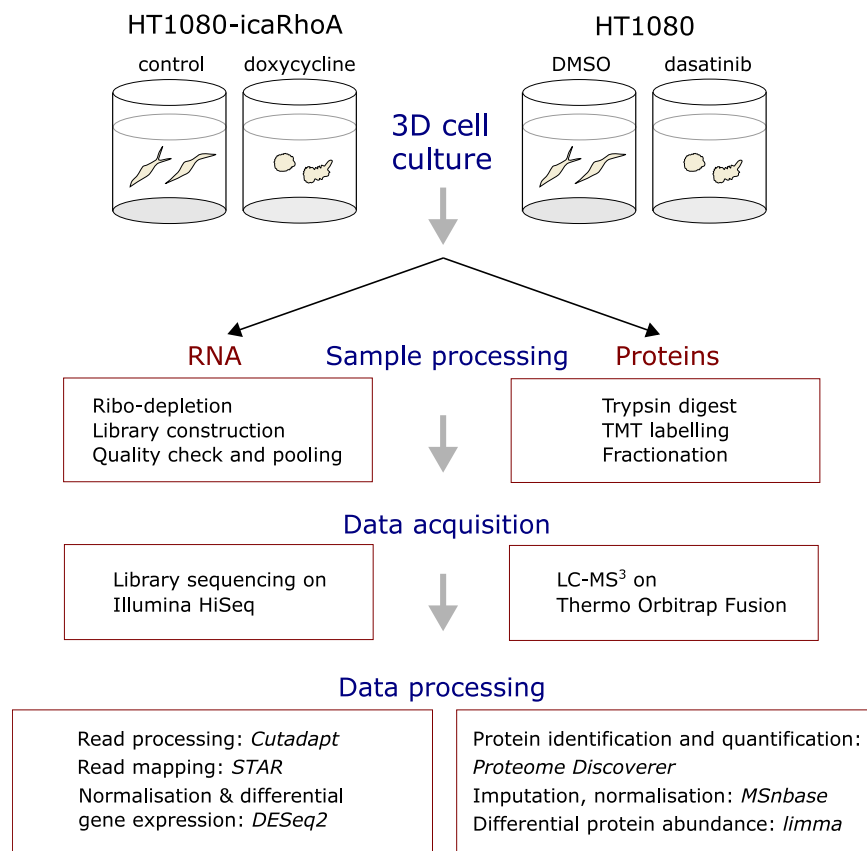


Fig. 1 Schematic overview and experimental design of the study.

still unavailable¹⁵. Despite the large effort to reveal signalling underlying invasive behaviour of cells, understanding of cancer cell invasion plasticity is still insufficient, mainly due to the scarcity of results obtained from more *in vivo*-like 3D cell culture conditions. To date, there are only three published works reporting gene expression profiling of amoeboid cells^{16–18}. While these data provided the first insight into the transcriptome of amoeboid cells, they were not obtained from three-dimensional (3D) cultures, an essential requirement to get the most relevant results.

To gain more insight into molecular level adaptation of cancer cells to the amoeboid state, we performed large scale transcriptomic and proteomic profiling of HT1080 fibrosarcoma cells after MAT in 3D cell culture (Fig. 1). In order to discern treatment-specific effects, we used two experimental treatments that are sufficiently effective in inducing MAT and compatible with cell viability in 3D collagen gels. The first treatment was doxycycline-inducible constitutively active RhoA (icaRhoA) gene expression; RhoA-ROCK pathway is known to play a key role in amoeboid migration^{13,19} and constitutively active RhoA expression has been shown to induce amoeboid morphology in glioblastoma cells and effective MAT in HT1080^{3,20}. The second, very different treatment was that with dasatinib, a Src kinase inhibitor, that has been previously also shown to induce MAT^{21,22}. The cells were kept for 48 hours in 3D collagen without or with the MAT-inducing treatment and then the whole samples including the collagen and any extracellular material were homogenized and further processed for RNA sequencing or mass spectrometry analysis. Total RNA was depleted of rRNA, converted into a stranded cDNA library and sequenced with Illumina HiSeq sequencer. Protein lysates were trypsin-digested, TMT-labelled, fractionated and analysed on Thermo Orbitrap Fusion mass spectrometer.

Overall, our work provides data for an unprecedented comparison of parallel mesenchymal and amoeboid transcriptomes and proteomes obtained from 3D conditions to reveal new details of the transition regulation, the impact of the transition on biological properties of the cells in terms of gene expression and protein abundance, and possibly discover potential new therapeutic opportunities.

Methods

Cells, DNA constructs and transfection. HT1080 cells were maintained in DMEM (4.5 g/l glucose, pyruvate) supplemented with 10% fetal bovine serum and 50 µg/ml gentamicin (all from Sigma) at 37 °C in humidified atmosphere with 5% CO₂. The cultures were regularly tested for mycoplasma contamination. 3D cell culture experiments were performed with rat tail collagen (SERVA) at concentration 1 mg/ml and DMEM supplemented with 1% fetal bovine serum, 15 mM HEPES and 50 µg/ml gentamicin. Stably transfected cells were prepared by lentiviral transduction using the second-generation packaging system (pLVX constructs, Tet-On Advanced Gene expression system, Clontech). The DNA transfections were performed with polyethylenimine (Polysciences, Inc.). All populations of stably transfected cells were further enriched for the respective encoded fluorescence with a

cell sorter. Cells bearing inducible constructs were transiently induced with doxycycline before the sorting. In all experiments, cells stably transfected with the doxycycline-inducible EGFP-RhoA G14V fusion construct were treated with 250 ng/ml doxycycline (Sigma). In dasatinib experiments, HT1080 cells stably expressing LifeAct-mCherry exogene²³ (further referenced just as HT1080) were treated with 1 μ M dasatinib (LC Laboratories) in DMSO or equivalent volume of DMSO only (0.1% final concentration). All plasmids used in the study were constructed in the lab with standard molecular cloning procedures; details as well as the plasmids themselves are available upon request.

Time-lapse microscopy in 3D collagen matrix. To record cell invasion in 3D collagen, control and doxycycline- and dasatinib-treated cells with or without protease inhibitor GM6001 (10 μ M) were imaged every 5 minutes using JuLI FL, an in-incubator microscope (NanoEnTek Inc.). For digital holographic microscopy, cells were embedded in collagen as stated above and left to adjust to 3D conditions for at least 12 hours. Images were acquired automatically in 80–90 second intervals. Cells were imaged using QPHASE (TESCAN Brno, s.r.o.) a multimodal holographic microscope based on CCHM technology as described previously³.

Cell morphology in 3D collagen matrix. 100,000 cells were seeded in 250 μ l of collagen matrix in a 48-well plate. Hoffman modulation contrast microscopy images were taken 48 hours later from approx. 20 planes along z-axis. Cell morphology was assessed by measuring the ratio of the maximum length and maximum width manually using Fiji software²⁴. At least 300 cells were analysed for each condition.

RNA extraction and sequencing. One million HT1080 cells were cultured in a 500 μ l 3D collagen gel for 48 hours in a 24-well plate. Gels from two wells were transferred into one 2 ml tube and homogenized with Tissue Tearor (BioSpec Products) in 600 μ l of RNA extraction solution (60% v/v water-saturated phenol, 3.25 M guanidine thiocyanate, 400 mM sodium acetate buffer pH 4.0, 0.4% w/v N-lauroylsarcosine, 160 mM 2-mercaptoethanol) plus 100 μ l of 6.1 M sodium chloride. 200 μ l of chlorophorm was added to approx. 1 ml of the lysate and the mixture was vortexed vigorously for 10 seconds. After 30-minute centrifugation at 18,000 g at 4 °C, the polar upper phase was transferred to a new tube, volume adjusted to 800 μ l with RNase-free water, RNA was precipitated with 600 μ l of isopropanol and recovered by centrifugation at 18,000 g for 30 min at 4 °C. The RNA pellet was washed three times with 600 μ l of 75% ethanol and air-dried. Next, the RNA was treated with DNase I to remove any possible genomic DNA contamination. To this end, the pellet was directly dissolved in 100 μ l of solution containing 4 units of DNase I (Thermo Fisher Scientific) in manufacturer-provided reaction buffer and incubated at 37 °C for 30 min. After that, the RNA was re-purified with RNeasy Protect Mini Kit (Qiagen) according to the manufacturer's instructions and eluted in 50 μ l of RNase-free water. Stranded, Illumina HiSeq-compatible library was constructed with ScriptSeq Complete (Human/Mouse/Rat) library preparation kit (Epicentre) according to the manufacturer's instructions. The quality and size distribution of sequencing libraries was analysed with Agilent BioAnalyzer 2100. An equimolar pool of 6 sample libraries was sequenced on one whole lane of Illumina HiSeq 2000/2500 series sequencer in high output, paired mode (2 \times 100 cycles in case of the inducible caRhoA cells and 2 \times 125 cycles in case of the DMSO/dasatinib treated cells). Raw reads were trimmed of adapter sequences with Cutadapt²⁵ (version 1.15), quality-checked with fastqc and mapped to human genome version GRCh38.91 with the STAR short read aligner²⁶ version 2.5.4b with default settings and output extended with read counts per gene. Complete adapter-trimmed fastq data are available from the ArrayExpress database at EMBL-EBI under accession number E-MTAB-6823²⁷. The samples and related files are summarized in Table 1.

High-throughput proteomic profiling. One million HT1080 cells were cultured in a 500 μ l 3D collagen gel for 48 hours in a 24-well plate. Gels from two wells were transferred into one 2 ml tube, mixed with equal volume of 2x TEAB buffer (200 mM triethylammonium bicarbonate pH 8.5, 4% sodium deoxycholate, both from Sigma) and homogenized with Tissue Tearor (BioSpec Products). After 15-minute centrifugation at 18,000 g at 4 °C, supernatant was transferred into a new tube and kept frozen at –80 °C before further processing. Protein samples were trypsin-digested, TMT-labeled, fractionated and analysed on Orbitrap Fusion mass spectrometer (Thermo Fisher Scientific) as described previously^{28–30}. Specifically, sample volume containing 100 μ g of proteins was precipitated by four volumes of cold acetone (overnight at –20 °C). After centrifugation the pellets were washed with 80% acetone and let dry. Samples were resuspended in 100 mM TEAB (Triethylammonium bicarbonate, Thermo #90114) reduced with 5 mM TCEP (Tris(2-carboxyethyl)phosphine hydrochloride, Sigma #4706) for 30 min at 60 °C and alkylated with 10 mM MMTS (S-Methyl methanethiosulfonate, Sigma #64306) for 10 min at room temperature. Proteins were digested with trypsin (trypsin:protein ratio 1:50) overnight at 37 °C. TMT label was added according to manufacturer protocol. After 60 min, the labelling reaction was stopped by addition of hydroxylamine. All samples were pooled and vacuum dried. Samples were desalted on Michrom C18 Opti Trap Macro (Optimize Technologies 10-04818-TN). Peptides were fractionated as follows. 100 μ l volume of a sample containing approx. 250 μ g of peptides was injected onto a C18 column (kinetex 1.7 μ m, EVOC18, 150 \times 2.1 mm) and separated with linear gradient from 0% A (20 mM ammonium formate, 2% acetonitrile pH 10) to 50% B (20 mM ammonium formate, 80% acetonitrile pH 10) in 32 min with flow rate 300 μ l/min 32 fractions were collected and pooled into 8 fractions. Resulting fractions were dried and resuspended in 20 μ l of 1% TFA. Nano reversed phase column (EASY-Spray column, 50 cm \times 75 μ m ID, PepMap C18, 2 μ m particles, 100 Å pore size) was used for LC/MS analysis. Mobile phase buffer A was composed of water, 2% acetonitrile and 0.1% formic acid. Mobile phase buffer B was composed of 80% acetonitrile in water and 0.1% formic acid. Samples were loaded onto the trap column (AcclaimPepMap300, C18, 5 μ m, 300 Å wide pore, 300 μ m \times 5 mm) at a flow rate of 15 μ l/min. Loading buffer was composed of water, 2% acetonitrile and 0.1% trifluoroacetic acid. Peptides were eluted with gradient of B from 2% to 60% over 240 min at a flow rate of 300 nl/min. Eluting peptide cations were

Sample	Cells	Treatment	Protocols	ENA	BioSD
1	HT1080-icaRhoA	none	P-MTAB-75206 to P-MTAB-75211	ERS2515967	SAMEA4695791
2	HT1080-icaRhoA	doxycycline	P-MTAB-75206 to P-MTAB-75211	ERS2515964	SAMEA4695788
3	HT1080-icaRhoA	none	P-MTAB-75206 to P-MTAB-75211	ERS2515968	SAMEA4695792
4	HT1080-icaRhoA	doxycycline	P-MTAB-75206 to P-MTAB-75211	ERS2515966	SAMEA4695790
5	HT1080-icaRhoA	none	P-MTAB-75206 to P-MTAB-75211	ERS2515969	SAMEA4695793
6	HT1080-icaRhoA	doxycycline	P-MTAB-75206 to P-MTAB-75211	ERS2515965	SAMEA4695789
7	HT1080-LifeAct-mCherry	DMSO	P-MTAB-75206 to P-MTAB-75211	ERS2515962	SAMEA4695786
8	HT1080-LifeAct-mCherry	dasatinib	P-MTAB-75206 to P-MTAB-75211	ERS2515960	SAMEA4695784
9	HT1080-LifeAct-mCherry	DMSO	P-MTAB-75206 to P-MTAB-75211	ERS2515963	SAMEA4695787
10	HT1080-LifeAct-mCherry	dasatinib	P-MTAB-75206 to P-MTAB-75211	ERS2515958	SAMEA4695782
11	HT1080-LifeAct-mCherry	DMSO	P-MTAB-75206 to P-MTAB-75211	ERS2515961	SAMEA4695785
12	HT1080-LifeAct-mCherry	dasatinib	P-MTAB-75206 to P-MTAB-75211	ERS2515959	SAMEA4695783

Table 1. Summary of RNA sequencing data.

Sample	Cells	Treatment	PRIDE RAW file
R1	HT1080-icaRhoA	none	D1_170107152223
R2	HT1080-icaRhoA	doxycycline	D2_170107195536
R3	HT1080-icaRhoA	none	D3_170108002847
R4	HT1080-icaRhoA	doxycycline	D4_170107104914
R5	HT1080-icaRhoA	none	D5_170108050200
R6	HT1080-icaRhoA	doxycycline	D6_170108093514
D1	HT1080-LifeAct-mCherry	DMSO	R1_170110145546
D2	HT1080-LifeAct-mCherry	dasatinib	R2_170110192857
D3	HT1080-LifeAct-mCherry	DMSO	R3_170111000208
D4	HT1080-LifeAct-mCherry	dasatinib	R4_170111043519
D5	HT1080-LifeAct-mCherry	DMSO	R5_170111090830
D6	HT1080-LifeAct-mCherry	dasatinib	R6_170111134141

Table 2. Summary of mass spectrometry proteomic data.

converted to gas-phase ions by electrospray ionization and analyzed on a Thermo Orbitrap Fusion (Q-OT-qIT, Thermo) mass spectrometer. Spectra were acquired with 4 seconds duty cycle. Full MS spectra were acquired in orbitrap within mass range 350–1,400 m/z with resolution 120,000 at 200 m/z and maximum injection time 50 ms. Most intense precursors were isolated by quadrupole with 1.6 m/z isolation window and fragmented using CID with collision energy set to 30%. Fragment ions were detected in ion trap with scan range mode set to normal and scan rate set to rapid with maximum injection time 50 ms. Fragmented precursors were excluded from fragmentation for 60 seconds. For quantification information of a TMT label 10 most intense fragments were isolated (simultaneous precursor selection) and fragmented in HCD on 65% energy, maximum accumulation time 140 ms, and fragments were measured in orbitrap on 60 K resolution. Raw data were processed in Proteome Discoverer 2.1. TMT reporter ions ratios were used for estimation of relative amount of each protein. Searches were done with the Human Uniprot reference database and a common contaminant database. Modification were set: peptide N terminus, lysine (unimod #737) and cysteine (unimod #39) as static, and methionine oxidation (unimod #1384) and protein N-terminus acetylation (unimod #1) as variable. Raw data are available from the PRIDE database³¹ under identifier PXD010425³². The samples and related files are summarized in Table 2.

Immunoblotting. One million cells were cultured in a 500 μ l 3D collagen gel for 48 hours in a 24-well plate. Gels from two wells were transferred to tubes containing 500 μ l of 2x SDS lysis buffer (2% SDS, 20% glycerol, 120 mM Tris, pH = 6.8) and homogenized using Tissue Tearor (BioSpec Products). After 10-minute centrifugation (18,000 rcf, 10 °C) 900 μ l of the solution was transferred to a fresh tube and protein concentration in the lysate was determined using the DCTM Protein Assay (Bio-Rad Laboratories). The lysates in each series were adjusted to the same protein concentration with 1x SDS lysis buffer. DTT (final concentration 50 mM) and bromophenol blue (final concentration 30 μ M) were added, and the samples were incubated at 95 °C for 10 min. Samples were separated on 10% or 12% SDS-polyacrylamide gels and transferred onto nitrocellulose membrane. Non-specific binding was blocked by incubation of the membranes for 60 min at room temperature in Tris-buffered saline (TBS) containing 4% BSA or 5% non-fat dry milk. The membranes were incubated with a primary antibody in 4 °C overnight, washed three times in Tris-buffered saline with Tween-20 (TBST) and incubated for 75 min with HRP-conjugated secondary antibody at room temperature. Membranes were washed with TBST two times, with TBS one time and developed using AmershamTM Imager 600 (GE Healthcare) and

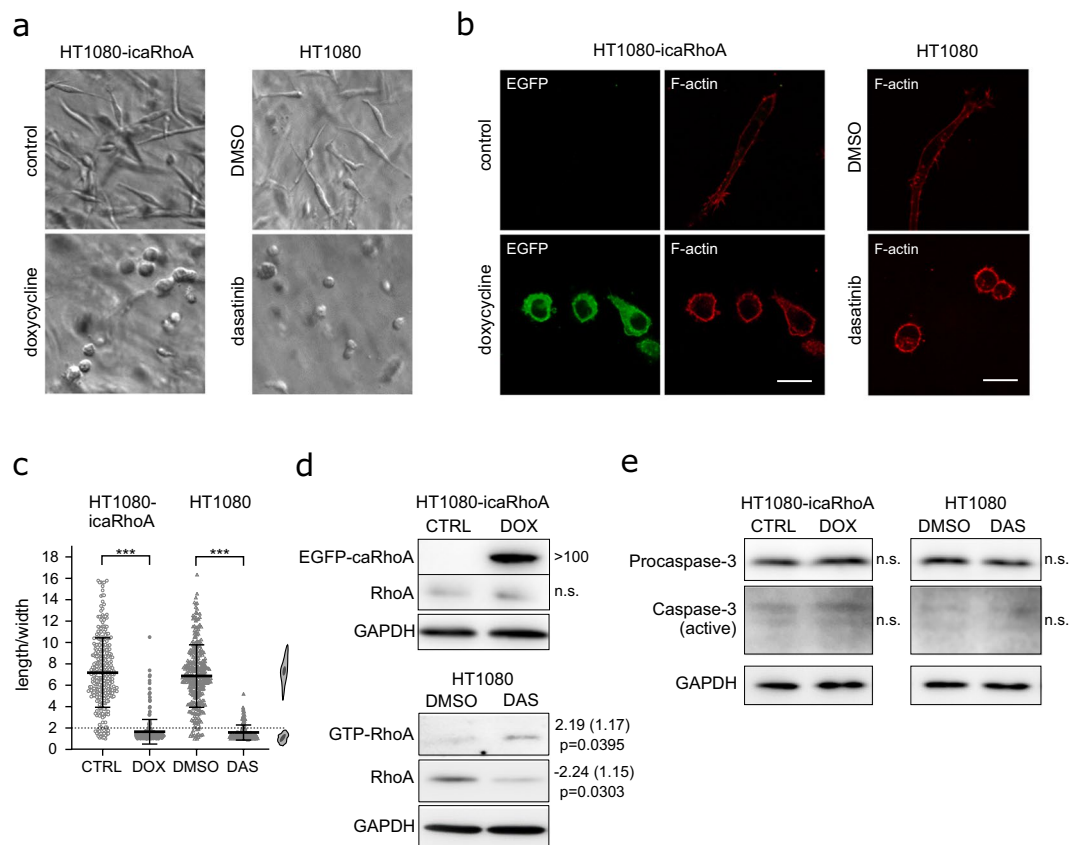


Fig. 2 Characterization of HT1080 cells induced to undergo MAT. **(a)** Representative wide-field images of cells in 3D collagen without or with induction of MAT. **(b)** Confocal microscopy of cells stained with fluorescently labelled phalloidin. **(c)** Quantification of cell morphology in 3D collagen (Student's t-test, p-values: *** $p < 0.001$, ** $p < 0.01$, * $p < 0.05$). **(d)** Immunoblotting detection of RhoA protein in cell lysates. In cells treated with DMSO or dasatinib, the active, GTP-bound RhoA was separated using GST-Rhotekin 1 RBD pulldown. Numbers next to blots indicate average fold change, standard error (both geometric) and p-value of paired t-test. **(e)** Immunoblotting detection of Caspase-3 in cell lysates. All results come from 48-hour experiments. Scale bar 20 μm in all cases. Abbreviations: CTRL – control, DOX – doxycycline, DAS – dasatinib, n.s. – not significant.

SuperSignal™ Femto Maximum Sensitivity Substrate (Thermo Fisher Scientific) or Western Bright TMECL (Advansta) HRP substrates. For probing the total protein level after a phosphoprotein detection and for loading control (GAPDH) detection, membranes were stripped in stripping buffer (200 mM NaOH) at 42 °C for 10 min. The primary antibodies used were as follows: GAPDH (Thermo Fisher Scientific MA5-15738), Caspase-3 (Cell Signaling Technology #9662), Fra-1 (Developmental Studies Hybridoma Bank PCR-FOSL1-1E3), C/EBP β (Abcam Ab32358), RhoA (Cell Signaling Technology #2117), GDF15 (Thermo Fisher Scientific PA5-17065) and MX1 (Cell Signaling Technology #37849). Quantification of band signals was performed using Multi Gauge software (Fujifilm, Tokyo, Japan). Band intensities of specific proteins were normalized to the GAPDH protein signal. Log-transformed signal values from at least three experiments were analyzed with paired Student's t-test. The results were presented as geometric means of fold change values with respect to control samples and the uncertainty was expressed as geometric standard errors.

Activated RhoA detection. One million cells were cultured in a 500 μl 3D collagen gel for 48 hours in a 24-well plate. Gels from two wells were transferred to tubes containing 500 μl of 2x Triton-X100 lysis buffer (2% Triton X-100, 100 mM Tris, 300 mM NaCl, pH = 7.1, protease inhibitors) and homogenized using Tissue Tearor (BioSpec Products) on ice. After 10-minute centrifugation (18,000 g, 10 °C) 800 μl of the solution was transferred to a fresh tube, protein concentration in the lysate was determined using the DCTM Protein Assay (Bio-Rad Laboratories) and adjusted to the same value in each series with 1x Triton X-100 lysis buffer. 50 μl of the lysate was transferred to a fresh tube (total lysate control) and the rest was incubated with rhotekin-bound GST-beads at 4 °C for 45 min. Beads were separated by brief centrifugation and washed two times with 1x Triton X-100 lysis buffer. Finally, beads were resuspended in 1x Laemmli sample buffer (0.35 M Tris-HCl, pH = 6.8, 10% SDS, 40% glycerol, 0.012% bromophenol blue) with DTT (50 mM) and incubated at 95 °C for 10 minutes. Samples were further processed according to the immunoblotting protocol described above.

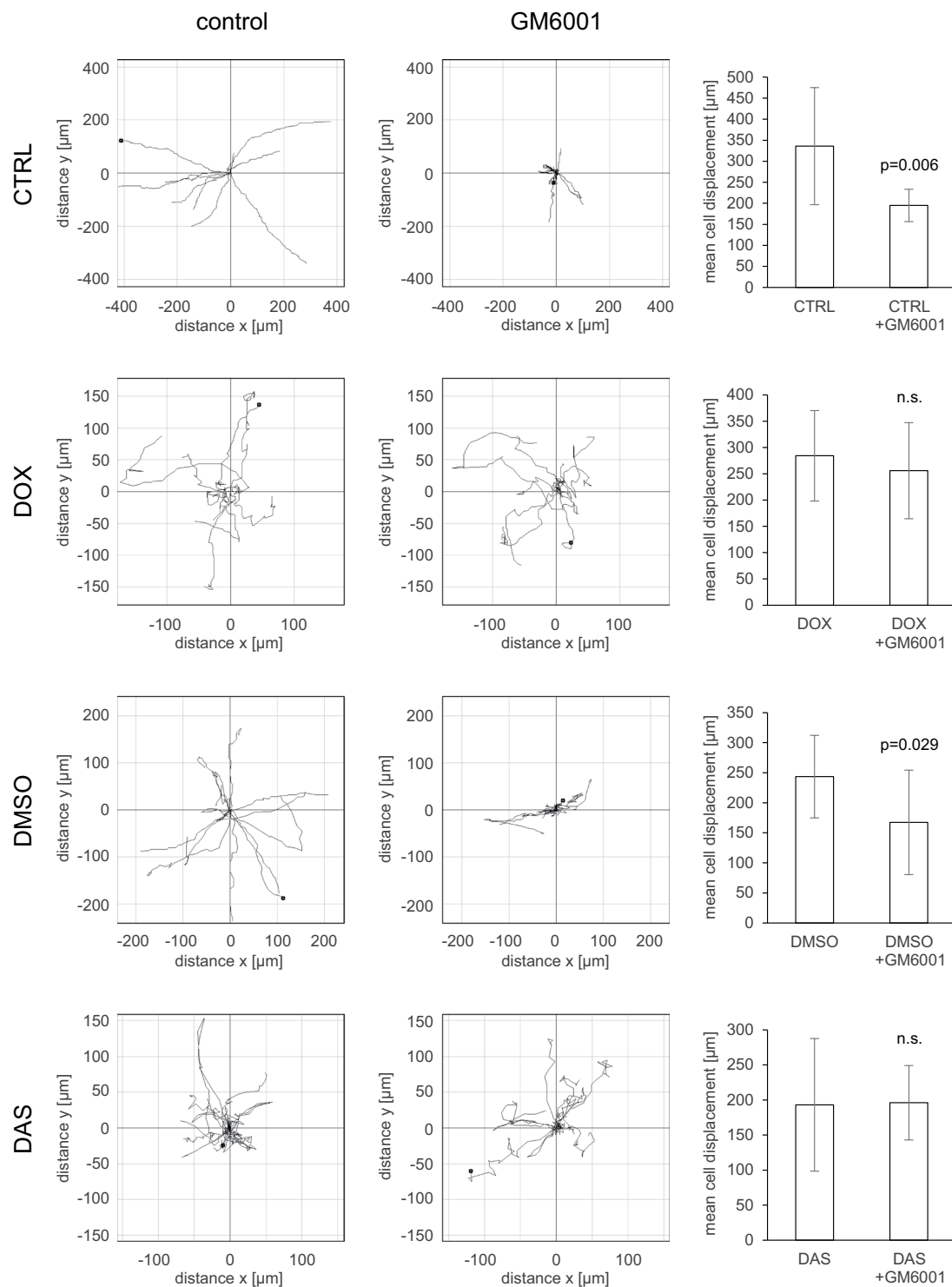


Fig. 3 Quantitative analysis of cell migration. HT1080-icaRhoA cells and HT1080 cells were embedded in rat-tail collagen (1 mg/ml) with or without GM6001. 12 hours later, migration of cells of the mesenchymal phenotype (HT1080-icaRhoA CTRL, HT1080 DMSO) and amoeboid phenotype (HT1080-icaRhoA DOX, HT1080 DAS) was monitored by wide-field microscopy for 15 hours. Track plots were generated using Chemotaxis Tool in ImageJ. Differences in the mean length of the tracks were analysed with two-tailed Student's t-test, $\alpha = 0.05$, $n = 9-13$. Error bars – standard deviation. Representative results of three independent experiments.

Statistical analysis. To estimate differential gene expression from RNA sequencing data a workflow based on the STAR aligner and DESeq2 R package was used as described previously¹⁸. Mass spectrometry data pre-processed with Proteome Discoverer 2.1 were imported into R environment and normalized with the MSnbase package³³. Differences in protein levels were estimated with moderated t-test statistics using the limma package³⁴.

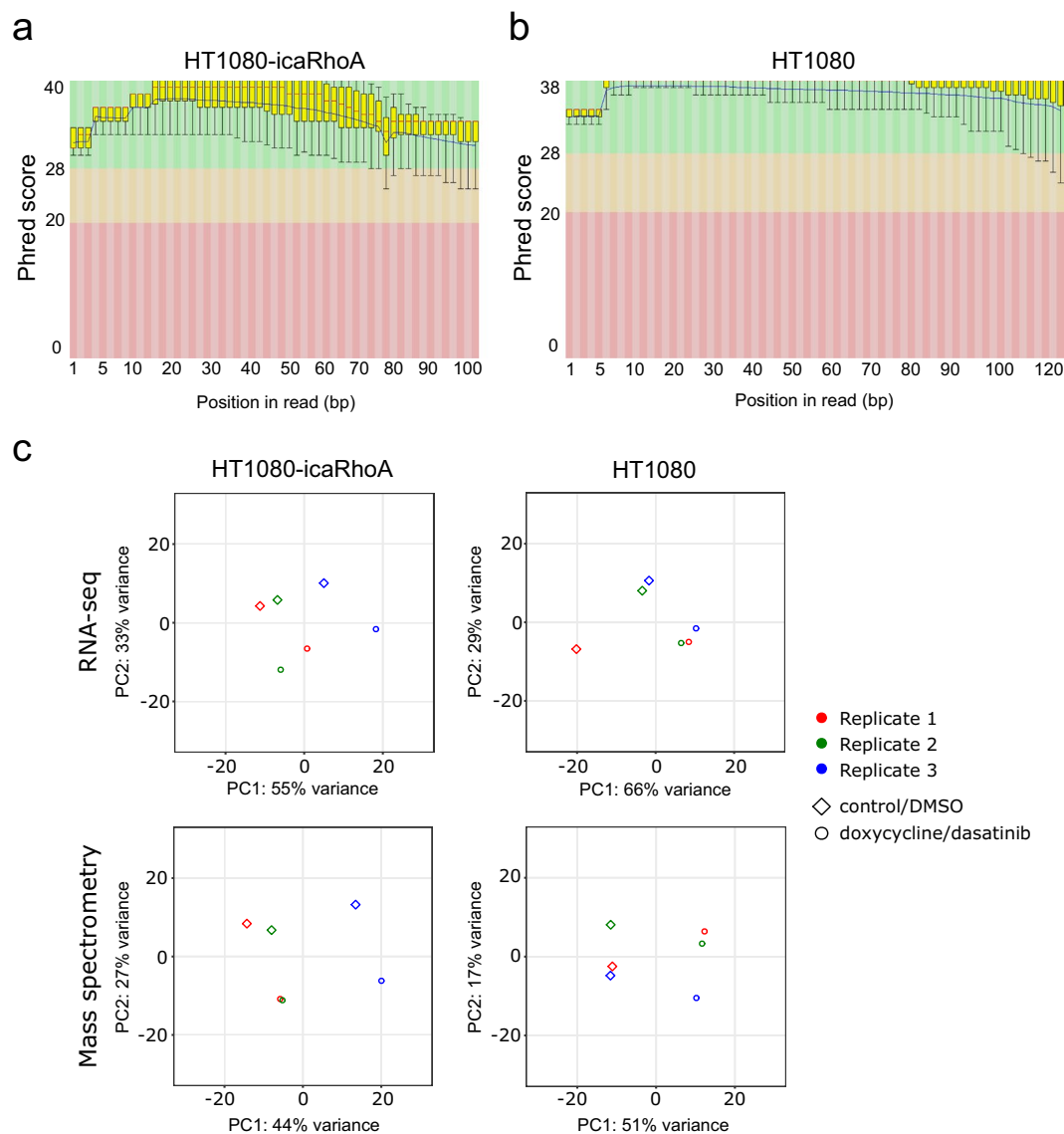


Fig. 4 Transcriptomic and proteomic profiling of HT1080 cells of mesenchymal and amoeboid migratory phenotype. **(a)** Per base sequence quality of RNA sequencing reads expressed as Phred score by position, HT1080-icaRhoA control sample 1, first reads. **(b)** Same as **(a)**, HT1080 DMSO control sample 1. **(c)** Principal component analysis of gene expression and protein abundance profiles. The normalized expression abundance of mRNAs and proteins was used. Point shapes indicate treatment; point colours mark individual pairs of biological replicates.

Data Records

Time-lapse movies documenting migratory phenotypes of the cells, uncropped immunoblot images, other supporting data referenced in the text, and complete results of differential transcript and protein level analyses were deposited in the Figshare³⁵ repository. Adapter-trimmed RNA sequencing data have been deposited in the ArrayExpress database at EMBL-EBI²⁷. Raw proteomic data have been deposited in the PRIDE database via the ProteomeXchange Consortium³². Besides the described data, the PRIDE record contains also a series of data-sets obtained from HT1080-icaRhoA cells cultured on 2D collagen (three pairs of doxycycline-untreated/treated cells).

Technical Validation

Induction of icaRhoA in otherwise mesenchymally migrating HT1080 fibrosarcoma induced effective MAT, i.e. cell rounding, membrane blebbing and amoeboid migration resistant to extracellular protease inhibitor (GM6001) in 3D collagen in the vast majority of the cell population (Figs. 2a–c, 3 and additional files available from Figshare³⁵; time-lapse Movies 1 and 2). Treatment of HT1080 cells with 1 μ M dasatinib produced very similar effects (Figs. 2a–c, 3 and time-lapse Movies 1 and 3 plus the files “Src activity in MAT-induced cells” all available from Figshare³⁵). We also tested the effect of other Src inhibitors and found that they were much weaker MAT

Sample	Cells	Treatment	Reads pairs total	Average read input length	% mapped	% multi-mapped	% too short
1	HT1080-icaRhoA	none	36,639,825	192	89.90	5.40	4.20
2	HT1080-icaRhoA	doxycycline	36,165,871	189	90.55	4.92	3.88
3	HT1080-icaRhoA	none	30,919,393	189	90.62	4.95	3.85
4	HT1080-icaRhoA	doxycycline	36,664,126	193	88.91	5.75	4.93
5	HT1080-icaRhoA	none	36,506,595	189	89.58	3.89	6.23
6	HT1080-icaRhoA	doxycycline	37,336,035	191	92.32	3.18	4.20
7	HT1080-LifeAct-mCherry	DMSO	39,167,799	245	95.18	2.83	1.85
8	HT1080-LifeAct-mCherry	dasatinib	35,644,171	235	90.21	6.67	2.84
9	HT1080-LifeAct-mCherry	DMSO	41,488,195	232	90.54	6.32	2.88
10	HT1080-LifeAct-mCherry	dasatinib	42,412,264	235	91.89	4.98	2.92
11	HT1080-LifeAct-mCherry	DMSO	42,742,403	232	88.94	7.72	3.02
12	HT1080-LifeAct-mCherry	dasatinib	45,846,680	231	89.71	6.87	3.08

Table 3. RNA sequencing raw data and mapping metrics.

inducers than dasatinib (see the file “Src inhibitors comparison” available from Figshare³⁵). The different potential of the Src inhibitors to induce MAT could be attributed to their different effect on Src structure and localization³⁶. The induction of the EGFP-RhoA G14V fusion protein in HT1080-icaRhoA cells was verified with immunoblotting (Fig. 2d). Activation of RhoA – an expected feature of the amoeboid phenotype – in dasatinib-treated cells was confirmed with GST-Rhotekin 1 Rho binding domain (RBD)-based pulldown assay (Fig. 2d, see also the file “RhoA activity in MAT-induced cells” available from Figshare³⁵). To verify that the observed membrane blebbing is not due to initiation of apoptosis, we detected Caspase-3 in protein lysates from the cells in 3D collagen. While we easily detected the non-cleaved pro-form in all samples, only a faint signal of the active, cleaved form of Caspase-3 could be detected after a very long blot exposure in all samples with no significant differences (Fig. 2e).

RNA sequencing of control and MAT-induced samples (three pairs of independent biological replicates for each treatment) yielded 31–46 million paired-end reads per sample. Raw reads trimmed of adapter sequences were quality-checked with FastQC software³⁷. FastQC’s plots of Phred scores (the standard measure of position reading confidence) by position (Fig. 4a,b) showed typical high-quality profiles with decreasing quality towards the ends of reads. Note that the inducible caRhoA series samples were sequenced with 2×100 cycles while the dasatinib treatment series samples were sequenced later with improved version of the sequencing chemistry enabling longer read length (2×125 cycles). The mapping metrics of STAR aligner showed an average paired read length of 191 bases for inducible caRhoA samples and 235 bases for dasatinib treatment series samples. In average, the aligner uniquely mapped 90.7% of the fragments to human genome, 5.3% fragments were multi-mapped, and 3.7% fragments were excluded as too short. The complete mapping metrics is listed in Table 3.

Mass spectrometry sample quality was checked with the aid of PreviewTM software, version 2.2.9 from Protein Metrics Inc. The effectiveness of tryptic digestions was verified before TMT labelling. Next, we checked for completeness of the labelling procedure. All checks were done as short 30-minute gradient with roughly 250 ng peptide injections. Missing cleavage was under 10% of all peptides and approx. 95% of all N termini and 100% of all lysines were successfully labelled with TMT tags. We identified 5,687 proteins in the icaRhoA series samples and 6,477 proteins in the dasatinib series samples. Among them there were 101 and 105 bovine proteins, respectively, coming from the fetal bovine serum used in the cell culture. For further analysis, we excluded these bovine proteins and all proteins with more than one missing intensity value in the sample series leading to 4,637 and 5,880 proteins, respectively usable for differential protein abundance analysis.

Principle component analysis of normalized gene expression and protein abundance profiles showed that the treatments, but also the biological replication are sources of significant variation (Fig. 4c). The paired character of the data thus has to be reflected in a linear model design formula in order to obtain the most accurate results from the statistical analyses of differential gene expression or differential protein abundance.

Differential gene expression analysis with DESeq²³⁸ identified 894 out of 12,030 genes (7.4%) significantly changed (with adjusted P-value < 0.1) after induction of caRhoA. Dasatinib treatment changed the expression of 996 out of 12,637 (8.1%) genes. Differential protein abundance with limma R package³⁴ revealed 410 out of 4,637 (8.8%) proteins significantly changed with adjusted P-value < 0.2 after induction of caRhoA. Dasatinib treatment changed the abundance of 674 out of 5,880 with adjusted P-value < 0.05 (11.5%) proteins. Note that we used a stricter adjusted P-value cut-off on the dasatinib data as the biological replicates were more uniform providing smaller P-values overall (with the opposite for the icaRhoA data). The differential gene and protein expression analysis results are summarized with volcano plots in Fig. 5a. Complete results are available from Figshare³⁴ as “differential_expression_analyses.xlsx” spreadsheet file. The file also presents lists of genes and proteins concordantly affected by both MAT-inducing treatments in separate sheets. Joint hierarchical clustering of affected genes across both treatment sample series showed a high similarity in the overall impact of MAT on gene expression (Fig. 5b).

To validate the results of the high-throughput analyses, we performed immunoblotting experiments with independent biological samples (different from those used for the high-throughput analyses) to measure differences in protein abundance of four proteins – C/EBP β , GDF15, MX1 and Fra-1 that were selected from those identified with both transcriptomic and proteomic profiling to be concordantly affected by both experimental

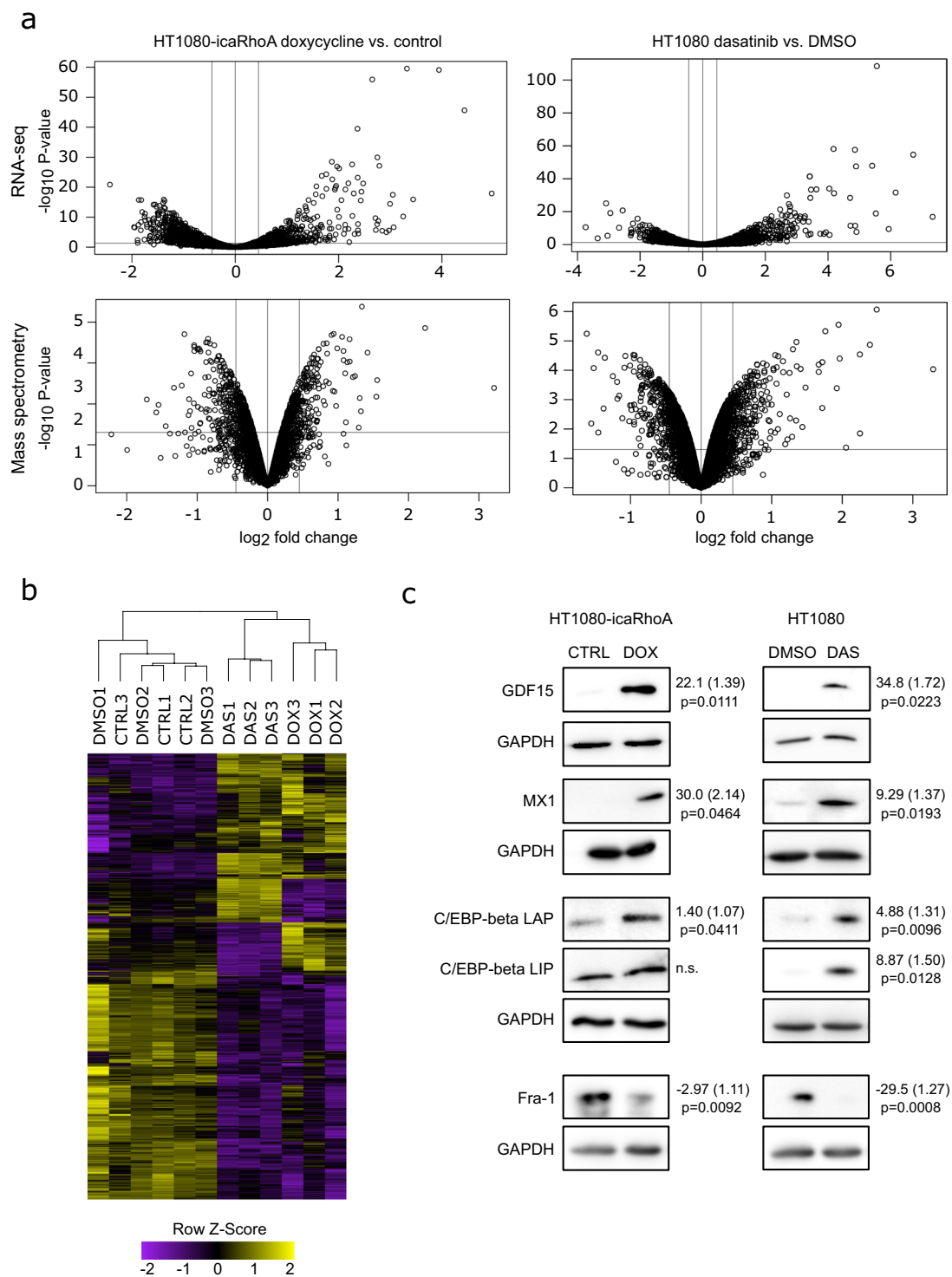


Fig. 5 Analysis and validation of transcriptomic and proteomic results. **(a)** Volcano plots of transcripts and proteins affected by MAT in each treatment group. Vertical lines mark -1.5 and 1.5 -fold change, respectively. Horizontal line marks statistical test P-value 0.05 . **(b)** Unsupervised hierarchical clustering of genes that are differentially expressed after MAT in both treatment groups ($P < 0.05$). The yellow colour scale represents a higher expression level, and the purple colour scale represents a lower expression level. **(c)** Immunoblotting validation of differential protein abundance analysis results. GAPDH was used as a loading control in all experiments. Representative results of three independent experiments. Numbers next to blots indicate average fold change, standard error (both geometric) and p-value of paired t-test.

treatments (see “Targets selected for verification” on Figshare³⁵ for the detected fold changes and corresponding adjusted P-values). The blots confirmed reproducible differences in all four proteins in agreement with the data (Fig. 5c).

Taken together, we present a valuable transcriptomic and proteomic dataset characterizing fibrosarcoma cell response to induced migration mode switching. The dataset provides a useful resource for better understanding of the mechanisms of cancer metastatic spreading. The experimental model presented here has some limitations. Both treatments used in this work to induce MAT have their specific MAT-unrelated effects. The phenotypes induced by the treatments might be not identical. The mechanisms underlying the transition in HT1080 cells might be, at least in some details, different from those described in other cell types, particularly in melanoma cells. However, we believe that only continuing accumulation of data obtained from different cell contexts and with different experimental approaches will bring a better and more general understanding of the amoeboid migratory phenotype and its importance for cancer metastasis.

Code availability

The scripts used in data processing are available from Figshare³⁵ (see “Code used in data processing”).

Received: 19 August 2019; Accepted: 21 April 2020;

Published online: 27 May 2020

References

- Hanahan, D. & Weinberg, R. A. Hallmarks of cancer: the next generation. *Cell* **144**, 646–674 (2011).
- Vaškovičová, K. *et al.* Invasive cells in animals and plants: searching for LECA machineries in later eukaryotic life. *Biol. Direct* **8**, 8 (2013).
- Tolde, O. *et al.* Quantitative phase imaging unravels new insight into dynamics of mesenchymal and amoeboid cancer cell invasion. *Sci. Rep.* **8**, 12020 (2018).
- Parsons, J. T., Horwitz, A. R. & Schwartz, M. A. Cell adhesion: integrating cytoskeletal dynamics and cellular tension. *Nat. Rev. Mol. Cell Biol.* **11**, 633–643 (2010).
- Tolde, O., Rösel, D., Veselý, P., Folk, P. & Brábek, J. The structure of invadopodia in a complex 3D environment. *Eur. J. Cell Biol.* **89**, 674–680 (2010).
- Nabeshima, K., Inoue, T., Shimao, Y. & Sameshima, T. Matrix metalloproteinases in tumor invasion: role for cell migration. *Pathol. Int.* **52**, 255–64 (2002).
- Friedl, P. & Wolf, K. Tube Travel: The Role of Proteases in Individual and Collective Cancer Cell Invasion. *Cancer Res.* **68**, 7247–7249 (2008).
- Wyckoff, J. B., Pinner, S. E., Gschmeissner, S., Condeelis, J. S. & Sahai, E. ROCK- and myosin-dependent matrix deformation enables protease-independent tumor-cell invasion *in vivo*. *Curr. Biol.* **16**, 1515–1523 (2006).
- Wolf, K. *et al.* Compensation mechanism in tumor cell migration: mesenchymal-amoeboid transition after blocking of pericellular proteolysis. *J. Cell Biol.* **160**, 267–277 (2003).
- Lämmermann, T. *et al.* Rapid leukocyte migration by integrin-independent flowing and squeezing. *Nature* **453**, 51–55 (2008).
- Charras, G. T. A short history of blebbing. *J. Microsc.* **231**, 466–478 (2008).
- Agarwal, P. & Zaidel-Bar, R. Diverse roles of non-muscle myosin II contractility in 3D cell migration. *Essays in Biochemistry* **63**, 497–508 (2019).
- Panková, K., Rösel, D., Novotný, M. & Brábek, J. The molecular mechanisms of transition between mesenchymal and amoeboid invasiveness in tumor cells. *Cell. Mol. Life Sci.* **67**, 63–71 (2010).
- Pandya, P., Orgaz, J. L. & Sanz-Moreno, V. Modes of invasion during tumour dissemination. *Mol. Oncol.* **11**, 5–27 (2017).
- Gandalovičová, A. *et al.* Migrastatics—Anti-metastatic and Anti-invasion Drugs: Promises and Challenges. *Trends in Cancer* **3**, 391–406 (2017).
- Sanz-Moreno, V. *et al.* ROCK and JAK1 Signaling Cooperate to Control Actomyosin Contractility in Tumor Cells and Stroma. *Cancer Cell* **20**, 229–245 (2011).
- Taddei, M. L. *et al.* Mesenchymal to amoeboid transition is associated with stem-like features of melanoma cells. *Cell Commun. Signal.* **12**, 24 (2014).
- Čermák, V. *et al.* RNA-seq of macrophages of amoeboid or mesenchymal migratory phenotype due to specific structure of environment. *Sci. Data* **5**, 180198 (2018).
- Kosla, J. *et al.* Metastasis of aggressive amoeboid sarcoma cells is dependent on Rho/ROCK/MLC signaling. *Cell Commun. Signal.* **11**, 51 (2013).
- MacKay, J. L. & Kumar, S. Simultaneous and independent tuning of RhoA and Rac1 activity with orthogonally inducible promoters. *Integr. Biol.* **6**, 885–894 (2014).
- Ahn, J., Sanz-Moreno, V. & Marshall, C. J. The metastasis gene NEDD9 product acts through integrin 3 and Src to promote mesenchymal motility and inhibit amoeboid motility. *J. Cell Sci.* **125**, 1814–1826 (2012).
- Logue, J. S., Cartagena-Rivera, A. X. & Chadwick, R. S. c-Src activity is differentially required by cancer cell motility modes. *Oncogene* **37**, 2104–2121 (2018).
- Riedl, J. *et al.* Lifeact: a versatile marker to visualize F-actin. *Nat. Methods* **5**, 605–607 (2008).
- Schindelin, J. *et al.* Fiji: an open-source platform for biological-image analysis. *Nat. Methods* **9**, 676–682 (2012).
- Martin, M. Cutadapt removes adapter sequences from high-throughput sequencing reads. *EMBnetjournal* **17**, 10–12 (2011).
- Dobin, A. *et al.* STAR: ultrafast universal RNA-seq aligner. *Bioinformatics* **29**, 15–21 (2013).
- Čermák, V., Gandalovičová, A., Merta, L., Rösel, D. & Brábek, J. Transcriptomic profiling of HT1080 fibrosarcoma cells of mesenchymal or amoeboid migratory phenotype. *ArrayExpress* <https://identifiers.org/arrayexpress:E-MTAB-6823> (2019).
- Erbán, T., Harant, K., Chalupnikova, J., Kocourek, F. & Stara, J. Beyond the survival and death of the deltamethrin-threatened pollen beetle *Meligethes aeneus*: An in-depth proteomic study employing a transcriptome database. *J. Proteomics* **150**, 281–289 (2017).
- Wang, Y. *et al.* Reversed-phase chromatography with multiple fraction concatenation strategy for proteome profiling of human MCF10A cells. *Proteomics* **11**, 2019–26 (2011).
- McAlister, G. C. *et al.* MultiNotch MS3 enables accurate, sensitive, and multiplexed detection of differential expression across cancer cell line proteomes. *Anal. Chem.* **86**, 7150–8 (2014).
- Vizcaíno, J. A. *et al.* 2016 update of the PRIDE database and its related tools. *Nucleic Acids Res.* **44**, D447–56 (2016).
- Harant, K., Čermák, V., Rösel, D. & Brábek, J. Proteomic profiling of HT1080 fibrosarcoma cells of mesenchymal or amoeboid migratory phenotype. *PRIDE Archive* <https://identifiers.org/pride.project:PXD010425> (2020).
- Gatto, L. & Lilley, K. S. MSnbase—an R/Bioconductor package for isobaric tagged mass spectrometry data visualization, processing and quantitation. *Bioinformatics* **28**, 288–9 (2012).
- Ritchie, M. E. *et al.* limma powers differential expression analyses for RNA-sequencing and microarray studies. *Nucleic Acids Res.* **43**, e47–e47 (2015).
- Čermák, V. *et al.* Mesenchymal-Amoeboid Transition in HT1080 Cells. *figshare* <https://doi.org/10.6084/m9.figshare.c.4623947.v4> (2020).

36. Koudelková, L. *et al.* Novel FRET-Based Src Biosensor Reveals Mechanisms of Src Activation and Its Dynamics in Focal Adhesions. *Cell Chem. Biol.* **26**, 255–268.e4 (2019).
37. Andrews, S. FastQC: a quality control tool for high throughput sequence data. [Online]. Available online at: <http://www.bioinformatics.babraham.ac.uk/projects/fastqc/> (2010).
38. Love, M. I., Huber, W. & Anders, S. Moderated estimation of fold change and dispersion for RNA-seq data with DESeq2. *Genome Biol.* **15**, 550 (2014).

Acknowledgements

The work was supported by the Kellner Family Foundation Principal Investigator Grant, Center for Tumor Ecology (reg. no. CZ.02.1.01/0.0/0.0/16_019/0000785) supported by the Operational Programme Research, Development and Education, and by the Charles University, projects GA UK No. 712217 and 1292217. The work was also funded in part by Czech Science Foundation grant 19-08410S. A part of the study was performed with the equipment for metabolomics and cell analyses (Grant no. CZ.1.05/2.1.00/19.0400) supported by the Research and Development for Innovations Operational Program, co-financed by the European regional development fund and the state budget of the Czech Republic. We acknowledge the BIOCEV Gene Core facility. We also acknowledge The Johns Hopkins University/CDI Laboratories and the Developmental Studies Hybridoma Bank (DSHB) for providing the anti-Fra-1 antibody.

Author contributions

V.Č. and A.G. designed and performed experiments, analysed the data, and contributed to manuscript writing. L.M. executed experiments and data analyses. K.H. performed the mass spectrometry proteomic analysis. D.R. and J.B. conceived the study and supervised the work.

Competing interests

The authors declare no competing interests.

Additional information

Correspondence and requests for materials should be addressed to J.B.

Reprints and permissions information is available at www.nature.com/reprints.

Publisher's note Springer Nature remains neutral with regard to jurisdictional claims in published maps and institutional affiliations.



Open Access This article is licensed under a Creative Commons Attribution 4.0 International License, which permits use, sharing, adaptation, distribution and reproduction in any medium or format, as long as you give appropriate credit to the original author(s) and the source, provide a link to the Creative Commons license, and indicate if changes were made. The images or other third party material in this article are included in the article's Creative Commons license, unless indicated otherwise in a credit line to the material. If material is not included in the article's Creative Commons license and your intended use is not permitted by statutory regulation or exceeds the permitted use, you will need to obtain permission directly from the copyright holder. To view a copy of this license, visit <http://creativecommons.org/licenses/by/4.0/>.

The Creative Commons Public Domain Dedication waiver <http://creativecommons.org/publicdomain/zero/1.0/> applies to the metadata files associated with this article.

© The Author(s) 2020

Supplementary materials: High-throughput transcriptomic and proteomic profiling of mesenchymal-amoeboid transition in 3D collagen

Vladimír Čermák^{*1,2}, Aneta Gandalovičová^{*1,2}, Ladislav Merta^{*1,2}, Karel Harant^{2,3}, Daniel Rösel^{1,2}, and Jan Brábek^{1,2}

1. Department of Cell Biology, Charles University, Viničná 7, Prague, Czech Republic
2. Biotechnology and Biomedicine Centre of the Academy of Sciences and Charles University (BIOCEV), Průmyslová 595, 25242, Vestec u Prahy, Czech Republic
3. Proteomics Core Facility, Faculty of Science, Charles University, Prague, Czech Republic

* These three authors contributed equally to the work.

Corresponding author: Jan Brábek (jan.brabek@natur.cuni.cz)

Address: Viničná 7, Prague, Czech Republic, 128 43

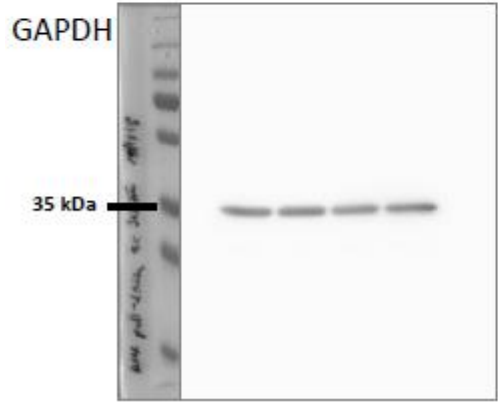
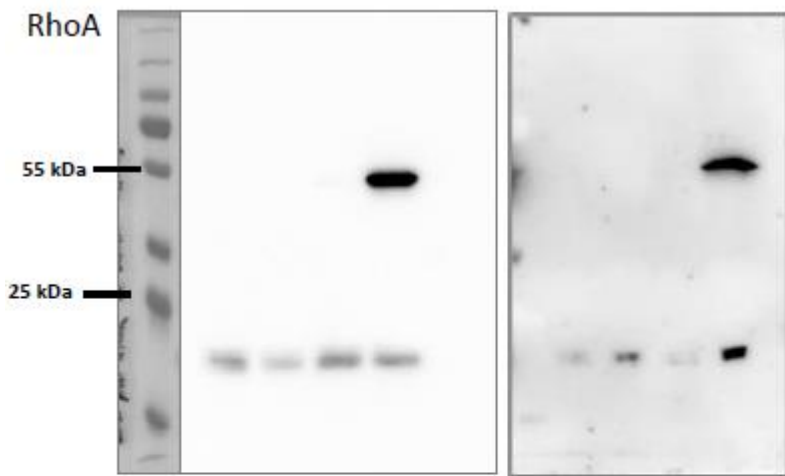
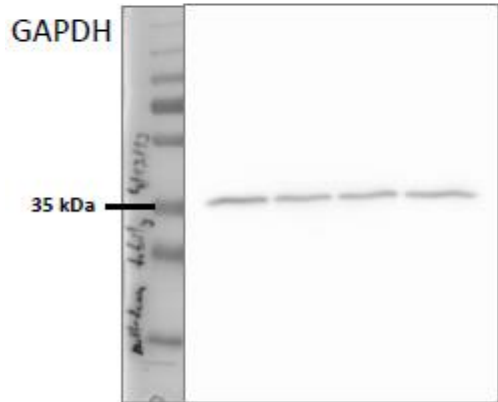
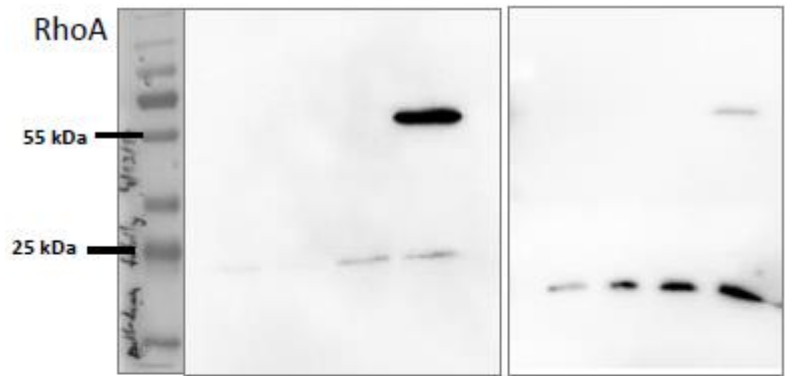
Phone/Fax: +420 325873900

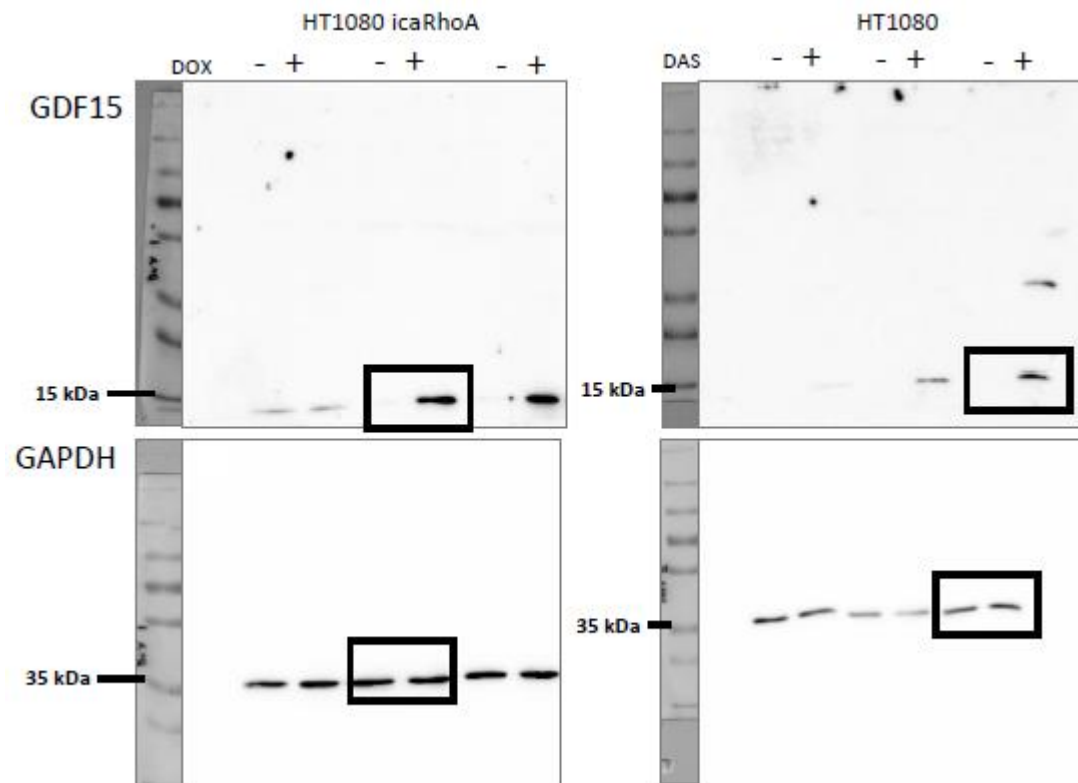
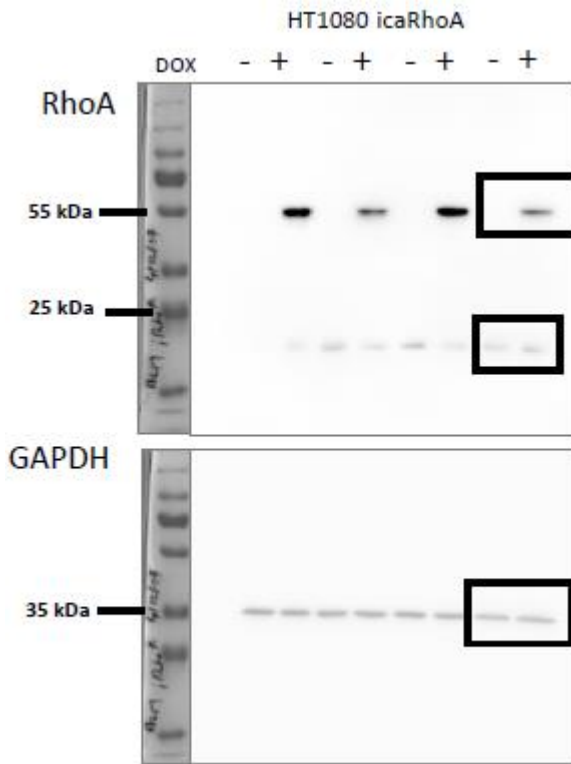
ORCID: 0000-0001-7754-7299

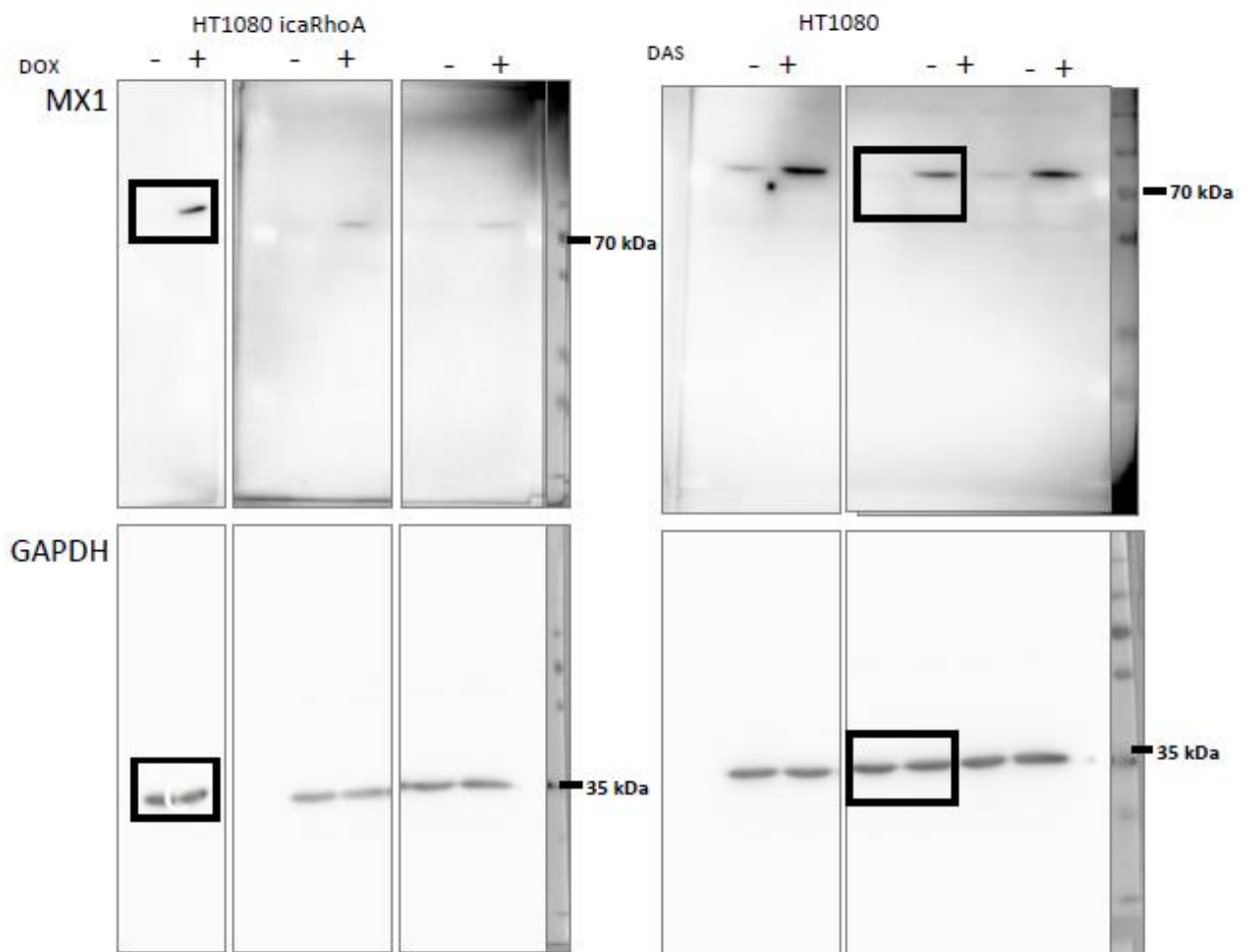
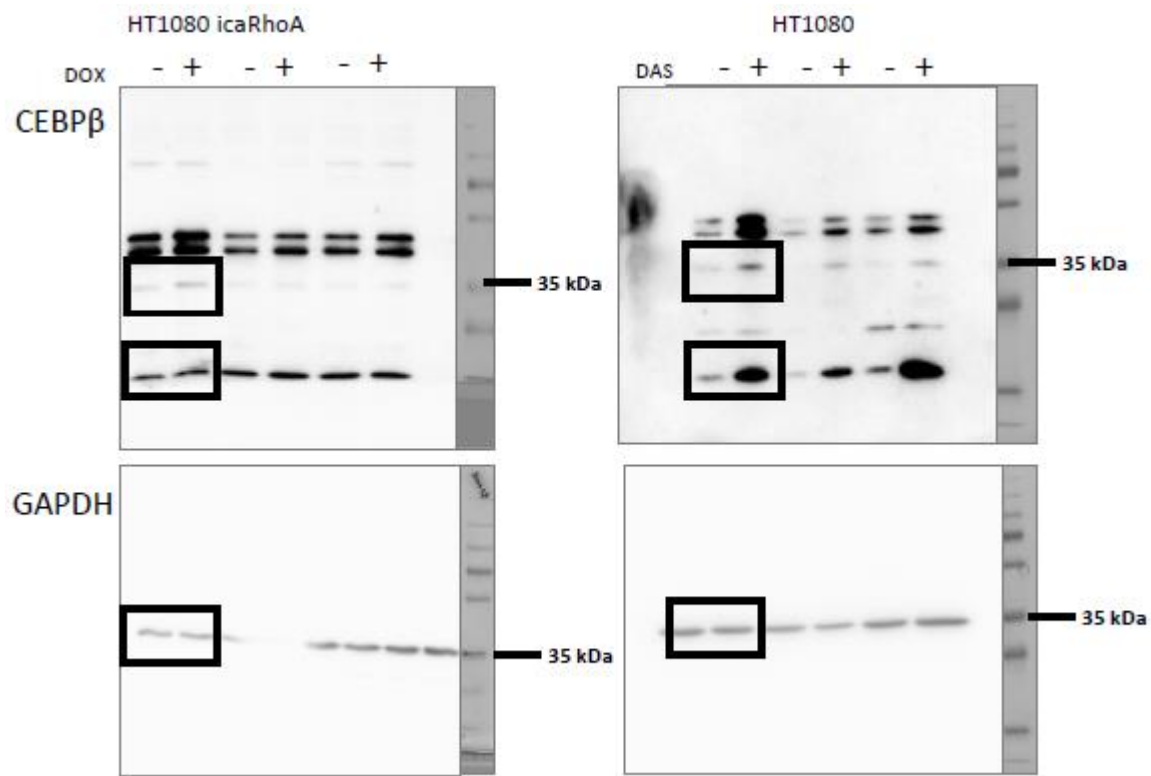
Note: Only “printable” (materials 1-5) are provided here, the full set of all Supplementary materials for the paper is available on *Figshare* <https://doi.org/10.6084/m9.figshare.c.4623947.v4>.

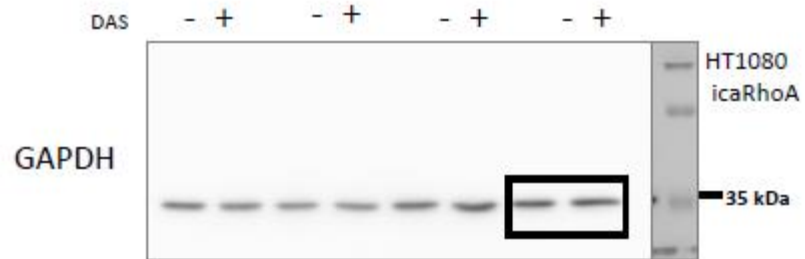
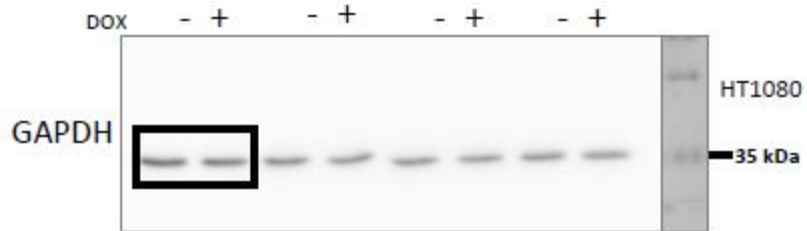
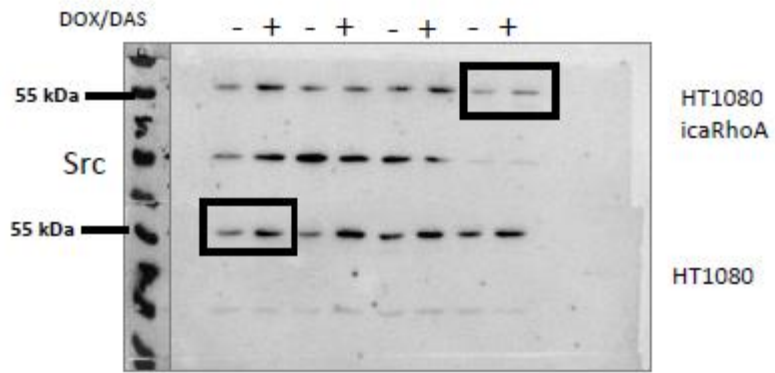
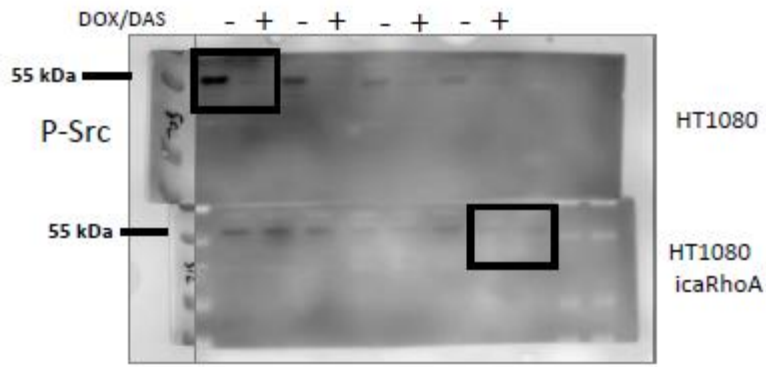
The list of all Supplementary materials available on Figshare:

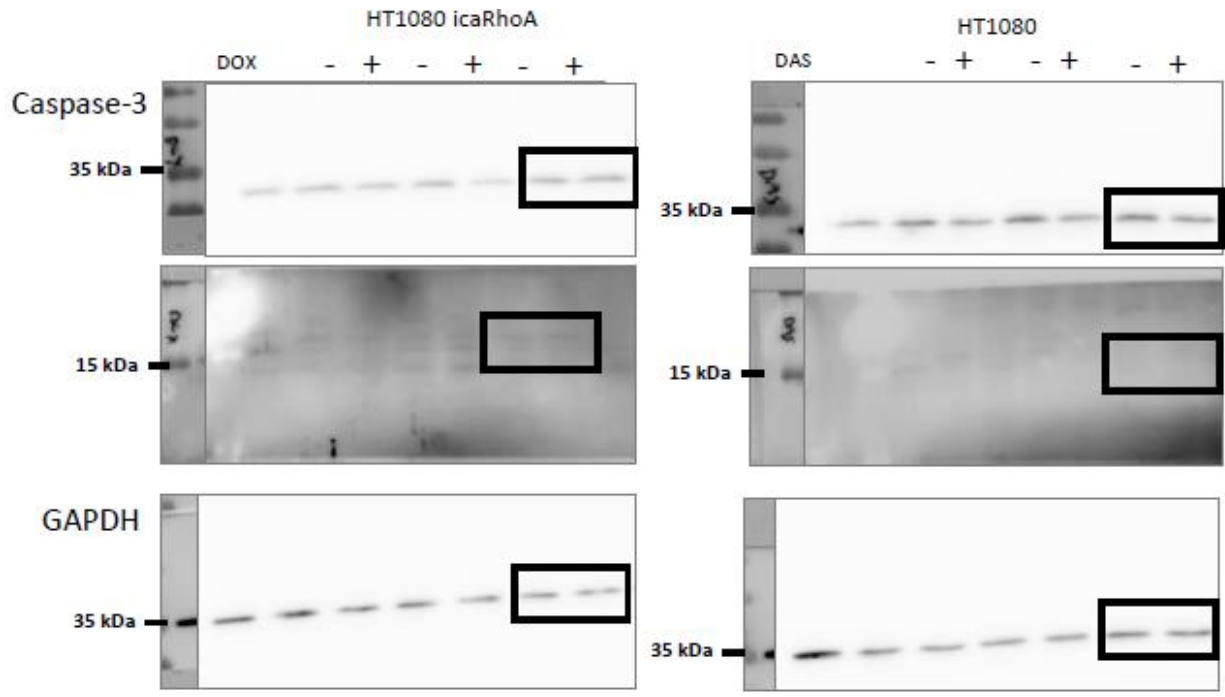
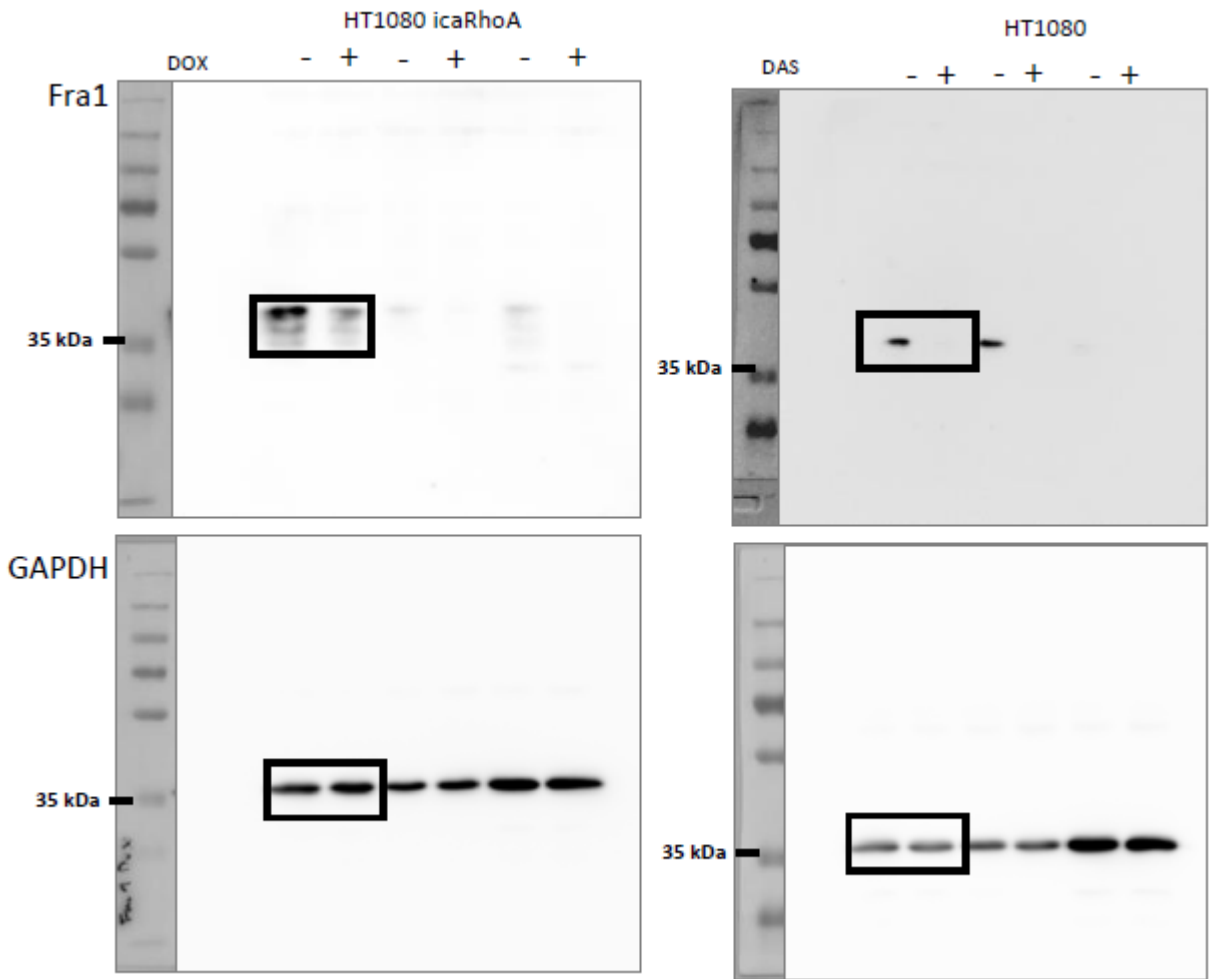
1. Uncropped western blot images
2. RhoA activity in MAT-induced cells
3. Quantitative analysis of cell migration
4. Src inhibitors comparison
5. Src activity in MAT-induced cells
6. Movie1 ... treatment effect on migratory behaviour
7. Movie2 ... caRhoA-induced amoeboid migration
8. Movie3 ... dasatinib-induced amoeboid migration
9. Dataset ... Differential expression analyses (dataset table)
10. Dataset ... Targets selected for verification
11. Software ... Code used in data processing



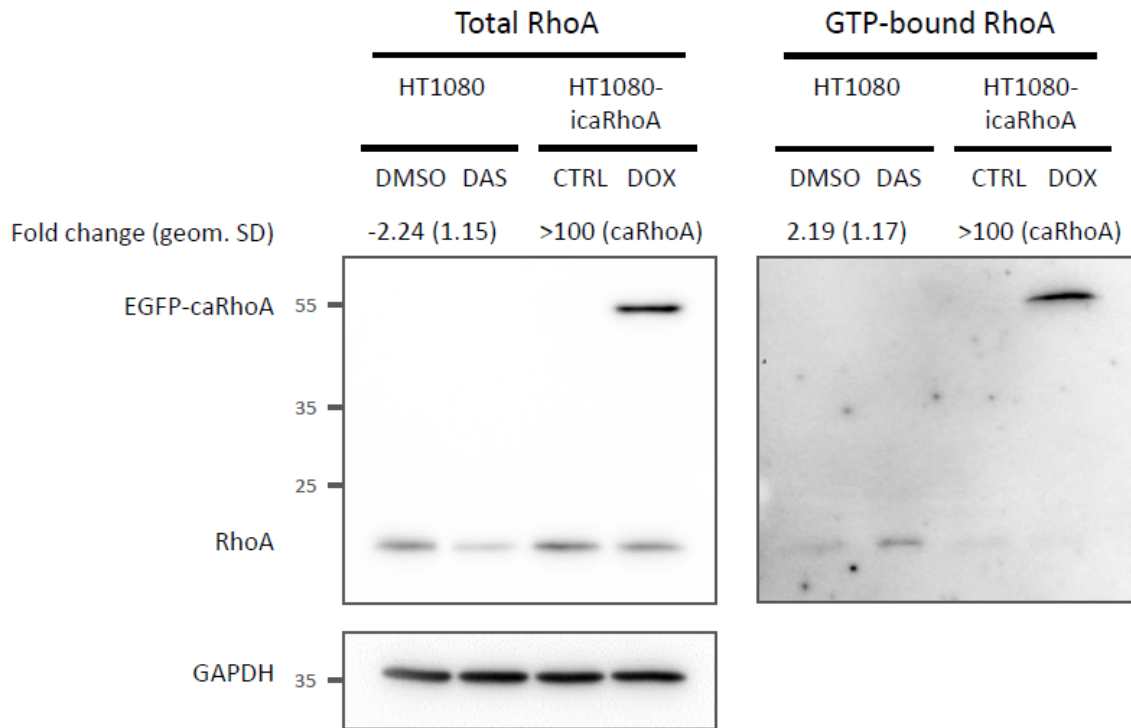




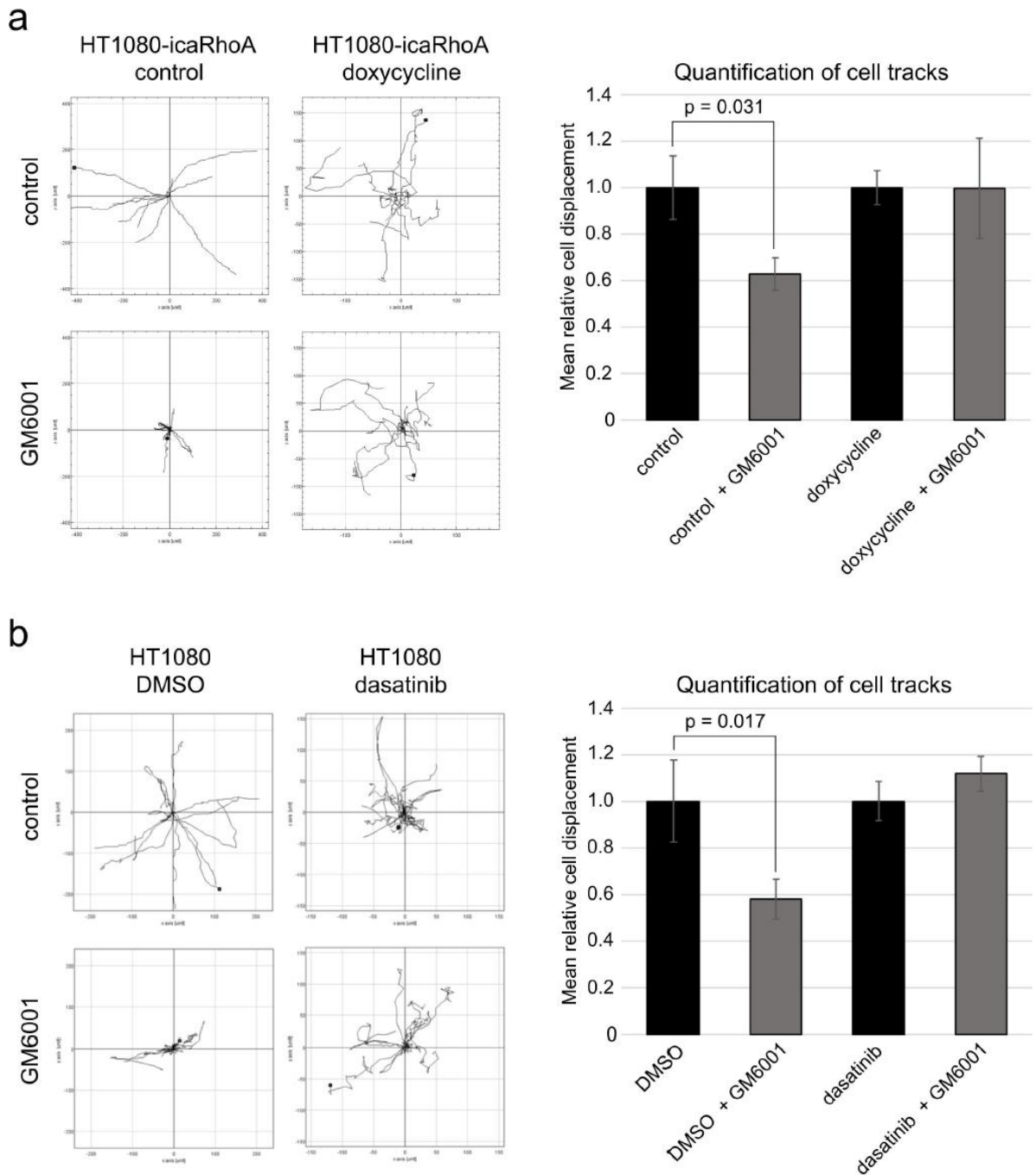




RhoA activity in MAT-induced cells



Total RhoA and GTP-bound RhoA (separated by pulldown with GST-rhotekin) were detected with immunoblotting using anti-RhoA antibody. Fold change values (treated vs. control) were estimated with densitometric quantification of band intensities. Representative results of three independent experiments. The presented fold change values are geometric averages of the three experiments. Abbreviations: CTRL – control, DOX – doxycycline, DAS – dasatinib.



Quantification of cell tracks

Treatment	Mean relative cell displacement
control	1.0
control + GM6001	~0.63 (p = 0.031)
doxycycline	~1.0
doxycycline + GM6001	~1.0

HT1080
DMSO

HT1080
dasatinib

control

dasatinib + GM6001

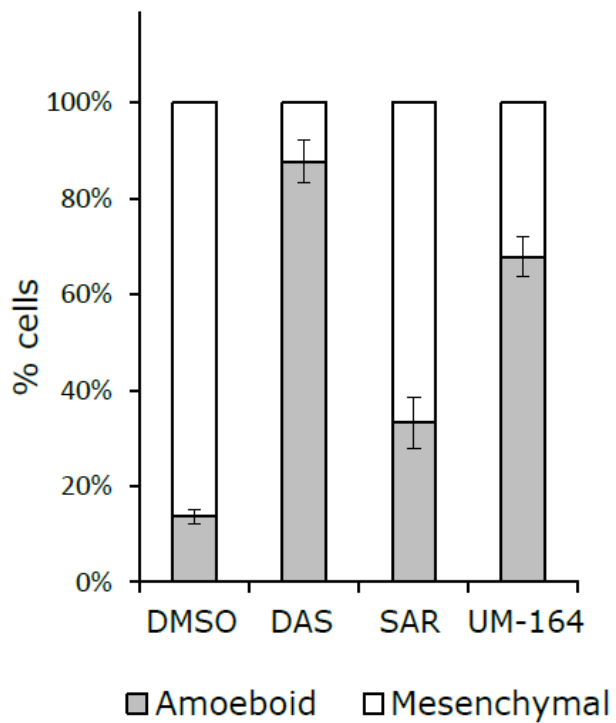
GM6001

Quantification of cell tracks

Treatment	Mean relative cell displacement
DMSO	1.0
DMSO + GM6001	~0.58 (p = 0.017)
dasatinib	~1.1
dasatinib + GM6001	~1.1

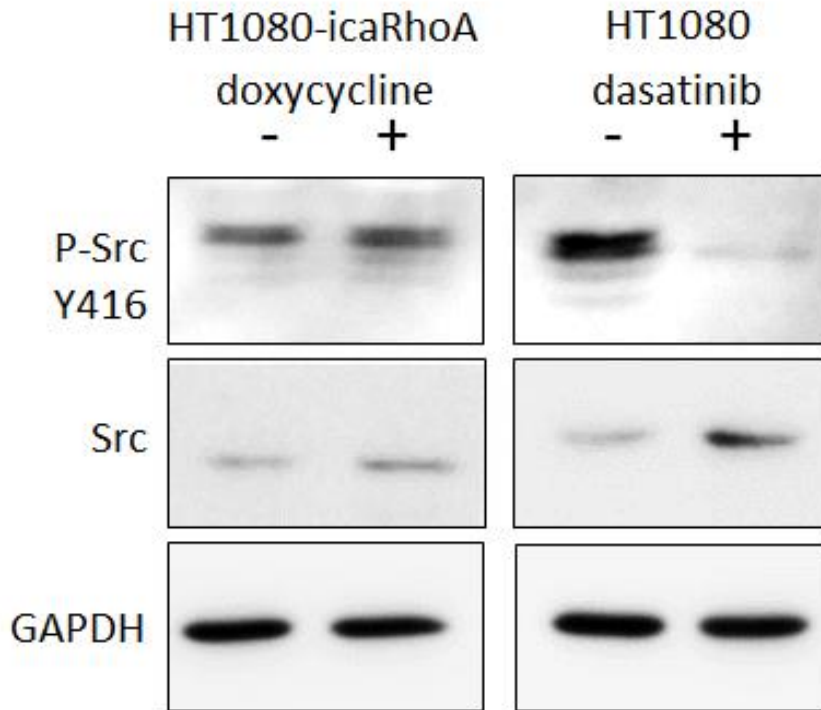
Quantitative analysis of cell migration. HT1080-icaRhoA cells (a) and HT1080 cells (b) were embedded in rat-tail collagen (1mg/ml) with or without GM6001. 12 hours later, migration of cells of the mesenchymal phenotype (HT1080-icaRhoA control, HT1080 DMSO) and amoeboid phenotype (HT1080-icaRhoA doxycycline, HT1080 dasatinib) was monitored by wide-field microscopy for 15 hours. Three independent experiments were evaluated. Track plots were generated using Chemotaxis Tool in ImageJ. For each condition, one representative track plot is shown. Relative differences in the mean length of the tracks were analyzed with two-way ANOVA (replicate + treatment group). Statistically significant differences are marked with the respective p-values.

3D cell morphology after treatment with Src inhibitors



Comparison of MAT-inducing potential of different Src inhibitors. HT1080 cells were treated with dasatinib (DAS, 1 μ M), saracatinib (SAR, 1 μ M), or UM-164 (100 nM) in 3D collagen. Statistical analysis of data from three independent experiments showed significant changes after all treatments (p-values < 0.001). Error bars - standard errors.

Src activity in MAT-induced cells



Src activity in cell lysates from 3D collagen was compared using immunoblotting detection of tyrosine 416 phosphorylated Src and total Src protein levels. GAPDH was used as a loading control.

Příloha č. 3 – Prvoautorská publikace

Merta, L.; Gandalovičová, A.; Čermák, V.; Dibus, M.; Gutschner, T.; Diederichs, S.; Rösel, D.; Brábek, J. Increased Level of Long Non-Coding RNA MALAT1 Is a Common Feature of Amoeboid Invasion. *Cancers (Basel)*. **2020**, *12*, 1136.

5-letý impakt faktor dle Web of Science: 6,433

Krátké shrnutí obsahu publikace:

V úvodu práce bylo představeno porovnání čtyřech dostupných transkriptomických datasetů získaných z buněk ve 3D prostředí podstupujících MAT/MAT. Na základě těchto porovnání byly identifikovány tři transkripty, které mají zvýšenou expresi v améboidní formě všech analyzovaných buněk – konkrétně lncRNA MALAT1 a NEAT1 a mRNA pro protein CEMIP. Zvýšená exprese MALAT1 a NEAT1 byla následně ověřována u celkem 6 modelů MAT. Konkrétně se jednalo o buněčné linie BLM (melanom), HT1080 (fibrosarkom) a MDA-MB-231 (prsni adenokarcinom) s inducibilní expresí konstitutivně aktivního RhoA (icaRhoA) a o stejné buněčné linie, u kterých bylo MAT vyvoláno farmakologicky pomocí dasatinibu (inhibitor kinázy Src).

Ve druhé části práce byl zvolen opačný přístup – snížením exprese MALAT1 bylo vyvoláno AMT. Pro tento účel byly s využitím nukleáz se zinkovými prsty připraveny klony melanomových buněk A375m2 (tato buněčná linie vykazuje více než 90% améboidní morfologii ve 3D prostředí) se sníženou expresí MALAT1. Tyto klony vykazovaly ve 3D prostředí kolagenové matrix protaženější morfologii než klony kontrolní. Zároveň u nich byla detekována vyšší proliferace a invazivita ze sferoidů. Klony byly připraveny stejným způsobem z další primárně améboidní melanomové buněčné linie A2058. Tyto klony se sníženou expresí MALAT1 nevykazovaly protaženější morfologii ani zvýšenou invazivitu oproti kontrolám, ovšem byly výrazně proliferativnější. Tento rozdíl v dosažených výsledcích mezi dvěma různými buněčnými liniemi byl připsán velice nízké invazivní plasticitě buněčné linie A2058, protože ač měly klony s nižší expresí MALAT1 vyšší aktivitu RhoA GTPázy, nepodstupovaly AMT. Stejně tak u nich AMT nevyvolal ROCK inhibitor Y27632.

Závěrem této publikace bylo zjištění, že zvýšená exprese MALAT1 je nejspíše charakteristickým prvkem améboidní invazivity.

Article

Increased Level of Long Non-Coding RNA MALAT1 Is a Common Feature of Amoeboid Invasion

Ladislav Merta ^{1,2}, Aneta Gandalovičová ^{1,2,†} , Vladimír Čermák ^{1,2,†} , Michal Dibus ^{1,2} ,
Tony Gutschner ³, Sven Diederichs ^{4,5} , Daniel Rösel ^{1,2}  and Jan Brábek ^{1,2,*}

- ¹ Department of Cell Biology, Charles University, Viničná 7, 12843 Prague, Czech Republic; ladislav.merta@natur.cuni.cz (L.M.); aneta.gandalovicova@natur.cuni.cz (A.G.); vladimir.cermak@natur.cuni.cz (V.Č.); michal.dibus@natur.cuni.cz (M.D.); daniel.rosel@natur.cuni.cz (D.R.)
- ² Biotechnology and Biomedicine Centre of the Academy of Sciences and Charles University (BIOCEV), Průmyslová 595, 25242 Vestec u Prahy, Czech Republic
- ³ Medical Faculty, Martin-Luther-University Halle-Wittenberg, Kurt-Mothes-Str. 3a, 06120 Halle (Saale), Germany; tony.gutschner@uk-halle.de
- ⁴ Department of Thoracic Surgery, Division of Cancer Research, Medical Center—University of Freiburg, Faculty of Medicine, University of Freiburg, German Cancer Consortium (DKTK)—Partner Site Freiburg, Breisacher Str. 115, 79106 Freiburg, Germany; s.diederichs@dkfz-heidelberg.de
- ⁵ Division of RNA Biology & Cancer, German Cancer Research Center (DKFZ), Im Neuenheimer Feld 280, 69120 Heidelberg, Germany
- * Correspondence: brabek@natur.cuni.cz
- † These authors contributed equally to the work.

Received: 18 March 2020; Accepted: 29 April 2020; Published: 1 May 2020



Abstract: The ability of cancer cells to adopt various migration modes (the plasticity of cancer cell invasiveness) is a substantive obstacle in the treatment of metastasis, yet still an incompletely understood process. We performed a comparison of publicly available transcriptomic datasets from various cell types undergoing a switch between the mesenchymal and amoeboid migration modes. Strikingly, lncRNA MALAT1 (metastasis-associated lung adenocarcinoma transcript 1) was one of three genes that were found upregulated in all amoeboid cells analyzed. Accordingly, downregulation of MALAT1 in predominantly amoeboid cell lines A375m2 and A2058 resulted in decrease of active RhoA (Ras homolog family member A) and was accompanied by the amoeboid-mesenchymal transition in A375m2 cells. Moreover, MALAT1 downregulation in amoeboid cells led to increased cell proliferation. Our work is the first to address the role of MALAT1 in MAT/AMT (mesenchymal to amoeboid transition/amoeboid to mesenchymal transition) and suggests that increased MALAT1 expression is a common feature of amoeboid cells.

Keywords: MALAT1; lncRNA; cancer; amoeboid invasion; mesenchymal invasion; invasion plasticity; melanoma

1. Introduction

Invasion of cancer cells leading to metastasis is responsible for the vast majority of the 9.6 million cancer-related deaths each year [1,2]. Cancer cells can migrate through the extracellular matrix (ECM) collectively or individually. In the case of individually migrating cells, two modes of invasion have been described—mesenchymal and amoeboid. Mesenchymally migrating cancer cells are characterized by an elongated shape, dependence on integrin-mediated adhesion, and secretion of proteolytic enzymes. In contrast, amoeboid cells are typically more rounded and frequently display intense membrane blebbing. Due to increased intracellular pressure and high actomyosin contractility, these cells “squeeze” themselves through pores in the ECM without the need to form strong focal

adhesions or degrade the ECM [3]. The Rho GTPase protein family (especially Rac1, Cdc42, RhoA, and RhoC) are key regulators of cytoskeletal reorganization, which is essential during cell movement. Unsurprisingly, their activity directly affects invasion modes. Upregulation of Rho-ROCK-driven actomyosin contractility promotes the amoeboid invasion mode. On the other hand, Rac1 is the key regulator of mesenchymal invasion, which drives Arp2/3-mediated actin polymerization [4–6].

A large hindrance in treatment of cancer metastasis is the ability of invading cells to switch from one mode of invasion to another in response to conditions of the environment or cancer therapy. This phenomenon is called cancer cell invasion plasticity [7] and is one of the reasons why an effective anti-metastatic treatment is still lacking [8]. Experimentally, the mesenchymal–amoeboid transition (MAT) can be induced by reduction of cell–ECM adhesion, loss of ECM proteolysis, enhanced RhoA-ROCK-driven contractility or microtubule destabilization. The reverse process—amoeboid–mesenchymal transition (AMT) is connected with increase of ECM adhesion, proteolytic ECM remodeling, and activation of Rac-induced actin assembly [9]. However, the molecular events underlying the MAT or AMT are insufficiently described. To improve our understanding of the processes, we performed a comparison of previously published datasets from AMT and MAT experiments, which identified metastasis-associated lung adenocarcinoma transcript 1 (MALAT1) to be involved in cancer cell invasion plasticity.

MALAT1, also referred to as NEAT2 (nuclear enriched abundant transcript 2), is a long non-coding RNA (lncRNA) of about 8000 nt in size [10] which shows high primary structure conservation among mammalian species [11]. It was originally discovered as a prognostic marker of metastasis in lung cancer, as its level was increased in metastatic tumors and its high level predicted poor prognosis [12]. Under physiological conditions, the MALAT1 gene is widely expressed and the transcript stays in the cell nucleus [12]. Within the nucleus, MALAT1 is localized in areas called speckles—reservoirs of splicing factors of pre-mRNA [11,13]. Functionally, MALAT1 has been shown to be involved in alternative splicing, regulation of gene expression, and to affect diverse aspects of cell behavior including proliferation and migration [14].

MALAT1 seems dispensable for normal development in mice since no abnormalities were observed after genetic knock-out [15,16]. Interestingly, however, a significant inhibition of both macro and micrometastases formation was observed in mammary carcinoma mouse model with MALAT1 knock-out, making MALAT1 a promising target in cancer therapy [17]. The upregulation of MALAT1 in cancer cells compared to the non-malignant cells was described in different types of primary tumors and also cancer cell lines derived from various tissues [18,19]. However, the role of MALAT1 in cancer is still ambiguous. In most studies, decreased level of MALAT1 is linked with lower proliferation and tumor growth [17,20,21], however, others found no difference after its knock-out [15], and in some works, MALAT1 was identified even as a suppressor of proliferation [22,23]. Moreover, in several studies, MALAT1 down-regulation resulted in a significant decrease of cancer cell migration [20,24–26], whereas in a recent study, MALAT1 suppressed the metastatic ability of breast cancer cells [27].

Taken together, MALAT1 has been shown to be an important player in cancer biology. Here, we report MALAT1 levels are differentially associated with the mesenchymal and amoeboid invasion mode, demonstrating its role in cancer cell invasion plasticity.

2. Results

2.1. Comparison of Transcriptomic Profiles of Amoeboid Cancer Cells and Macrophages Revealed Upregulation of MALAT1

The transitions between amoeboid and mesenchymal invasion modes are still incompletely understood. To identify genes with a potential role in MAT/AMT, we analyzed publicly available datasets from cells undergoing these transitions. For the comparison, we utilized only data sets from cells that have lost epithelial traits or are of mesenchymal origin. In 3D culture, they do not form aggregates and appear as single cells with clearly discernible morphological phenotype (amoeboid or mesenchymal) before and after the transition. Namely, RNA-seq data from the HT1080 fibrosarcoma

cell line undergoing MAT in 3D collagen after induction of constitutively active RhoA (icaRhoA) and after treatment with the Src inhibitor dasatinib (DAS) (manuscript in revision). Furthermore, we analyzed microarray data from constitutively amoeboid A375m2 melanoma cells cultured on top of thick, deformable collagen and treated with ROCK kinase inhibitors Y27632 and H1152 (further referred to as ROCKi) to induce AMT [28]. In addition, we included RNA-seq data from M2 macrophages of either amoeboid or mesenchymal morphology due to different stiffness of the surrounding collagen matrix [29].

To reveal the genes related to amoeboid phenotype, we performed an expression analysis and data intersection of differentially expressed transcripts to identify those genes that were downregulated after AMT (ROCKi treatment), but upregulated after MAT (induced icaRhoA, dasatinib treatment and macrophages in low concentration collagen) (Figure 1A). Strikingly, this analysis revealed only three genes showing consistent upregulation in all amoeboid cells of diverse biological backgrounds—lncRNAs MALAT1 and NEAT1, and CEMIP (Figure 1B). MALAT1 and NEAT1 are both lncRNAs shown to have complementary functions [30], which is why we have focused on these genes in subsequent analysis. CEMIP (cell migration inducing protein) is a protein involved in migration of cancer cells [31] and will be the subject of our future investigation. There was no overlap among genes downregulated in amoeboid cells in the four analyzed datasets (Figure 1C). The overlaps of upregulated/downregulated genes of only three datasets are listed in Supplementary Materials (Figure S1A,B). All data used for the comparison are available as Supplementary File S1.

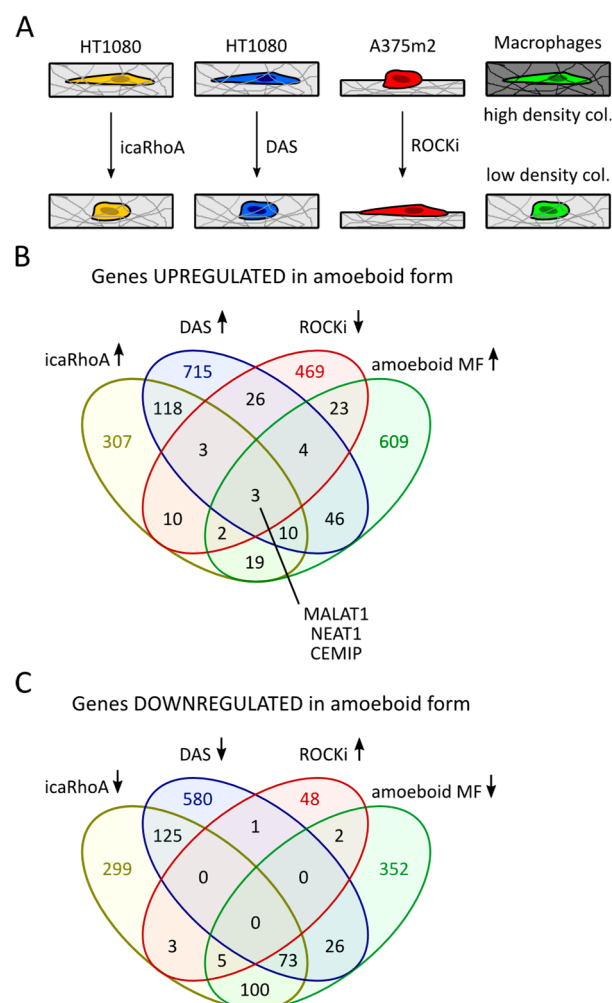


Figure 1. Comparison of published transcriptomic profiles of amoeboid cells in 3D conditions. (A) The schematic representations of experimental systems used in the comparison of datasets. (B) Venn diagram of gene sets upregulated in the amoeboid HT1080 cells (manuscript in revision) and macrophages [29],

and suppressed in A375m2 cells by ROCK inhibitors (ROCKi) [28]. (C) Venn diagram of gene sets downregulated in the amoeboid HT1080 cells and macrophages, and upregulated in A375m2 cells by ROCK inhibitors. In all cases, transcripts with adjusted *p*-value ≤ 0.25 and fold change >1.5 in either direction were considered differentially expressed.

2.2. MALAT1 Level Increases after MAT

LncRNAs MALAT1 and NEAT1 were identified as amoeboid-associated genes by comparison of available datasets. To experimentally verify this finding, we made use of previously established MAT systems in the fibrosarcoma cell line HT1080—doxycycline inducible expression of constitutively active RhoA (icaRhoA) and Src inhibitor dasatinib (DAS) treatment [32,33]. To broaden our results, we analyzed the effect of both MAT-inducing treatments in two additional cell lines with mesenchymal morphology in 3D collagen—BLM (melanoma) and MDA-MB-231 (breast adenocarcinoma). All the cell lines were able to undergo MAT after both treatments (Figure 2A–D).

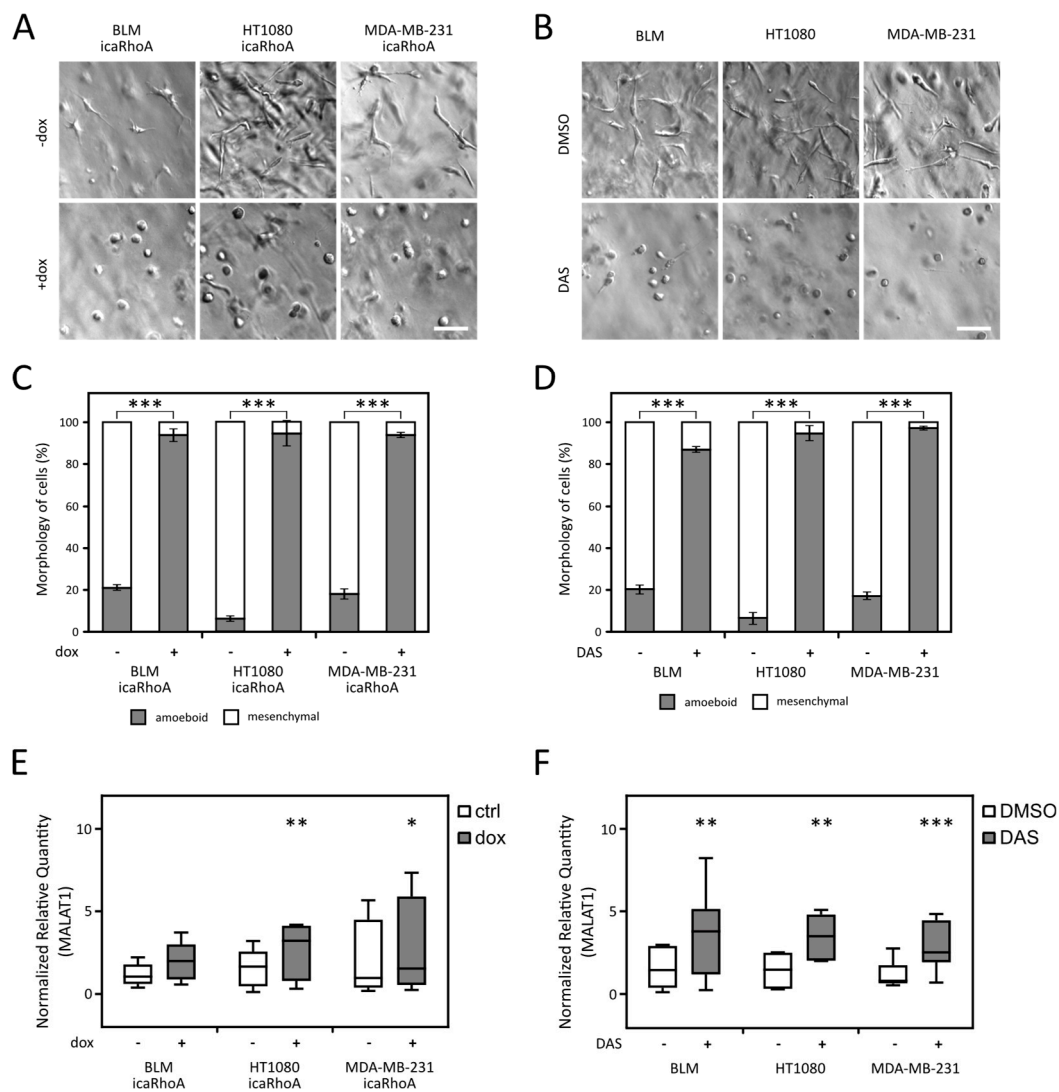


Figure 2. Morphological and RT-qPCR analysis of cell lines undergoing MAT (mesenchymal to amoeboid transition). (A,B) Representative wide-field images of cells in 3D collagen matrix with or without induction of MAT. (C,D) Quantification of cell morphology in 3D collagen. Data represent the

mean \pm SD. (E,F) RT-qPCR analysis of the MALAT1 (metastasis-associated lung adenocarcinoma transcript 1) gene expression. Median values are marked in the box plots, whiskers represent min to max range. Parts (A,C,E) depict cell lines with inducible constitutively active RhoA used for the MAT induction. (B,D,F) depict cell lines treated with dasatinib (DAS) to induce MAT. *p*-values: *** $p < 0.001$, ** $p < 0.01$, * $p < 0.05$. Scale bar 75 μ m in all cases. All data are a representation of at least 3 independent experiments.

Next, we analyzed the expression level of both lncRNAs by qPCR after induction of MAT by both treatments in all three cell lines. Interestingly, with the exception of BLM icaRhoA, all other five experimental systems exhibited significantly increased level of MALAT1 lncRNA after MAT (Figure 2E,F). Since the results of NEAT1 gene expression analyses were less consistent (Figure S2A,B), we decided to restrict our further analysis to MALAT1. To rule out the possible expression of a shorter MALAT1 transcript, we also included the analysis of MALAT1 expression using a primer pair targeting a region close to 5' end of the transcript (Figure S2C,D).

2.3. Reduction of MALAT1 Induces AMT in A375m2 Cells and Increases Invasion and Proliferation

As the increased level of MALAT1 expression might be an important feature of amoeboid cells, we further focused on analyzing the possible role of MALAT1 in the induction of the amoeboid phenotype in cancer cells. We wondered if genetic inactivation of MALAT1 can induce AMT in the well-characterized predominantly amoeboid cancer cell line A375m2 [28]. We made use of zinc-finger nucleases (ZFN) and homologous recombination to target the MALAT1 gene by insertional inactivation (Figure 3A). We prepared 35 candidate MALAT1-depleted clones derived from A375m2 cells. Of these, 15 clones showed successful integration of the EGFP expression cassette into MALAT1 locus (heterozygous clones; +/-), while other 20 kept intact MALAT1 alleles and expressed the EGFP gene due to non-specific integration of the cassette outside the MALAT1 locus (wild type clones; +/+). These MALAT wild-type clones were used as controls in subsequent experiments.

We next measured the MALAT1 transcript level in heterozygous and control clones and confirmed that heterozygous clones had significantly lower level of MALAT1 (Figure 3B and Figure S3A). To assess whether reduction of MALAT1 can suppress the amoeboid phenotype of A375m2 cells, we analyzed morphology of the clones in 3D collagen. Indeed, MALAT1+/- clones displayed significantly more elongated (mesenchymal) morphology than the control clones (Figure 3C). The representative morphology of MALAT1+/+ and +/- clones is depicted in Figure 3. To further analyze whether MALAT1+/- clones comply with mesenchymal traits, we have performed an active RhoA pulldown assay using GST-rhotekin bound to glutathione-agarose beads. We selected 5 representative clones of each genotype and pooled them into "+/+" and "+/-" samples. The active RhoA pulldown analysis clearly showed that MALAT1+/- clones had a significantly decreased level of active RhoA (Figure 3D), which is known to accompany AMT. To better characterize the phenotype of the MALAT1 heterozygous clones, we further analyzed the representative 5 clones of each genotype selected for RhoA-GTP pulldown assay. We measured proliferation in 3D collagen using a modified AlamarBlue assay (Invitrogen, Carlsbad, CA, USA) and found that proliferation of MALAT1+/- clones was significantly increased (Figure 3G) compared to control clones. Moreover, we assessed the invasive ability of the clones in 3D collagen using spheroid invasion assay, which showed that the MALAT1+/- clones were significantly more invasive than the MALAT1+/+ clones (Figure 3H,I).

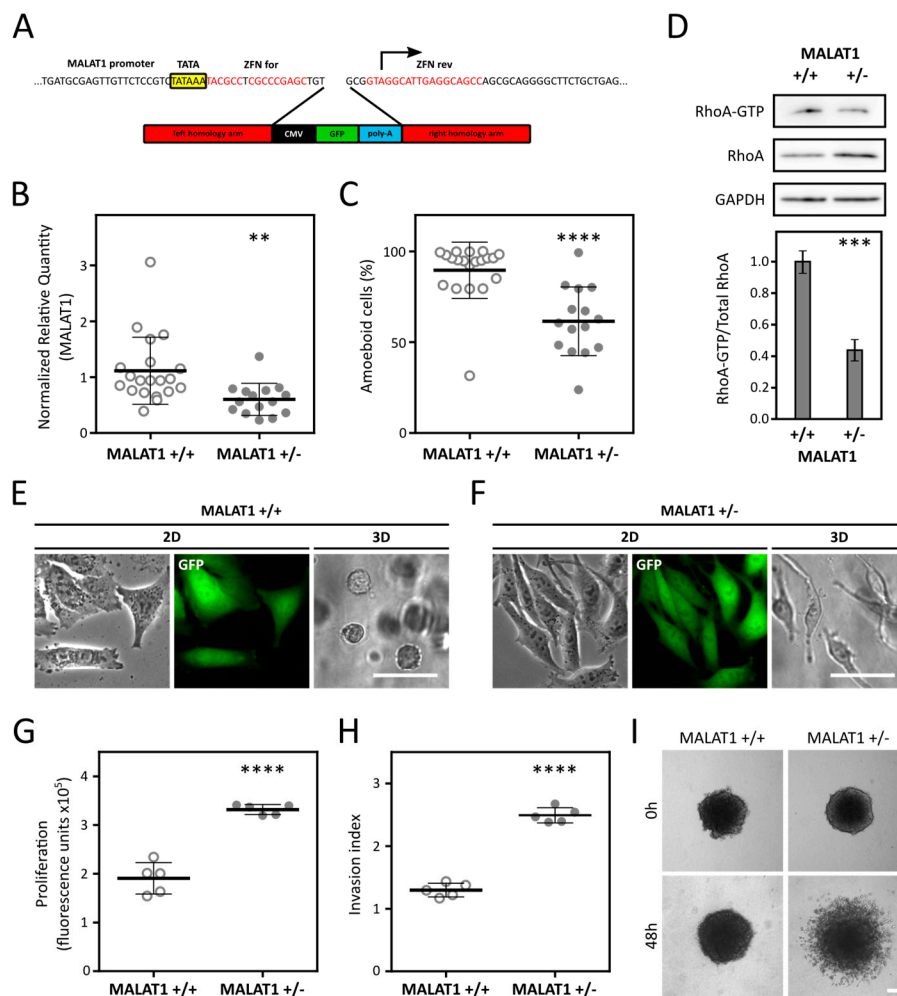


Figure 3. MALAT1 level and morphology of clones derived from the A375m2 cell line. (A) Zinc-finger nuclease (ZFN) system for MALAT1 depletion. The zinc-finger nucleases cleave between TATA box (yellow) and the site of transcription start (arrow). The binding motifs for ZFNs are depicted in red. The integration of the cassette into MALAT1 loci is mediated by homologous recombination using left and right homology arm. (B) RT-qPCR analysis of the MALAT1 gene expression in A375m2-derived clones. Data represent the mean \pm SD. (C) Quantification of clones' morphology in 3D collagen. Data represent the mean \pm SD. N MALAT1+/+ = 20 clones; N(MALAT1+/-) = 15 clones. (D) Pull-down of active RhoA from 3D samples of pooled clones. Representative immunoblots are in upper part, lower part represents the densitometry quantification. Data represent the mean \pm SEM. (E) Representative images of a control clone in 2D environment (Petri dish) and in 3D collagen matrix. (F) Representative images of a heterozygous clone in 2D environment and in 3D collagen matrix. (G) Proliferation of selected clones in 3D collagen. Data represent mean fluorescence of AlamarBlue \pm SD. (H) Quantification of cell invasion from spheroids. Data represent the mean \pm SD. (I) Representative images of invasion of control and heterozygous MALAT1 clones from spheroids. *p*-values: **** *p* < 0.0001, *** *p* < 0.001, ** *p* < 0.01. Scale bar 50 μ m in parts (E,F) and 150 μ m in part (I). Part (A) was taken and modified from [34].

2.4. Depletion of MALAT1 in A2058 Cells Decreases RhoA Activation but Is Not Followed by AMT

To broaden our results, we analyzed the effect of MALAT1 inactivation in A2058 melanoma cell line which also exhibits a prevalent amoeboid morphology in 3D collagen [35]. We used the same ZFN-based approach as in A375m2 cells to target the MALAT1 gene in A2058 cells. Interestingly, all the isolated clones that displayed decreased expression of MALAT1 were targeted in both alleles according to the PCR genotyping (MALAT1-/-). Despite the level of MALAT1 being significantly lower in A2058

MALAT1^{-/-} clones in comparison with control clones (Figure 4A), all clones maintained their amoeboid phenotype in 3D (Figure 4B). Nevertheless, using the active RhoA pull-down assay in pools of randomly selected 5 “+/+” and 5 “-/-” clones we found that, despite their unchanged morphology, the A2058 MALAT1^{-/-} clones exhibited significantly decreased levels of activated RhoA in 3D when compared to A2058 MALAT1^{+/+} clones (Figure 4C). Lower levels of active RhoA are supposed to be detected after a switch to mesenchymal phenotype. To further investigate the discrepancy between the decreased levels of Rho activation and the absence of AMT in MALAT1^{-/-} A2058 cells, we tested the response of the cells to ROCK inhibitor Y-27632, a well-defined inducer of AMT [3]. We observed no effect after ROCK inhibition (Figure S3B), suggesting that A2058 cells have, at least in part, lost invasion plasticity. Further, the invasiveness of A2058 MALAT1^{-/-} clones was not affected (Figure 4E,G) probably due to their inability to switch to mesenchymal mode of invasion. However, A2058 MALAT1^{-/-} clones were significantly more proliferative than control clones in agreement with the A375m2 results (Figure 4D).

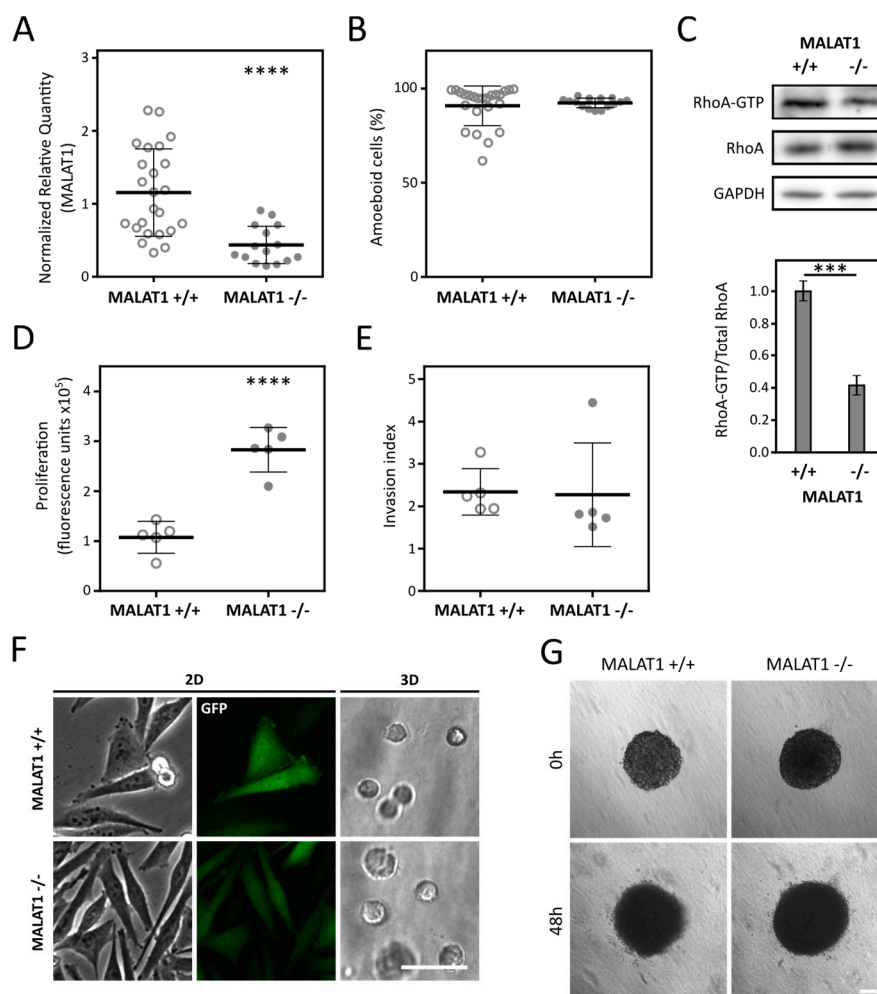


Figure 4. MALAT1 level and morphology of clones derived from the A2058 cell line. (A) RT-qPCR analysis of the MALAT1 gene expression in A2058-derived clones. Data represent the mean \pm SD. (B) Quantification of clones' morphology in 3D collagen. Data represent the mean \pm SD. N(MALAT1^{+/+}) = 24 clones; N(MALAT1^{-/-}) = 15 clones. (C) Pull-down of active RhoA from 3D samples of pooled clones. Representative immunoblots are in upper part, lower part represents the densitometry quantification. Data represent the mean \pm SEM. (D) Proliferation of selected clones in 3D collagen. Data

represent mean fluorescence of AlamarBlue \pm SD. (E) Quantification of cell invasion from spheroids. Data represent the mean \pm SD. (F) Representative images of MALAT1^{+/+} and MALAT1^{-/-} clones in 2D environment (Petri dish) and in 3D collagen matrix. (G) Representative images of invasion of control and heterozygous MALAT1 clones from spheroids. *p*-values: **** *p* < 0.0001, *** *p* < 0.001, Scale bar 50 μ m in part (F) and 150 μ m in part (G).

3. Discussion

The ability of cancer cells to switch between different modes of invasion due to characteristics of the surrounding environment or in response to therapeutic treatment [36] renders anti-metastatic therapy challenging. Despite the great effort made to explain the invasive behavior of cancer cells, our understanding of its mechanisms is still limited.

In this work we present, to our best knowledge, an unprecedented comparison of parallel mesenchymal and amoeboid transcriptomes was obtained from 3D conditions. Our comparison of publicly available datasets comprised data coming from three diverse cell types and four very different treatments. It is striking that despite the diversity of the datasets, we found an overlap of three genes upregulated in all cells of the amoeboid phenotype—CEMIP and lncRNAs MALAT1 and NEAT1 (Figure 1B). The increased level of MALAT1 after induction of MAT in three distinct cell lines (HT1080 fibrosarcoma cells, MDA-MB-231 breast cancer, and BLM melanoma cell lines) was further experimentally verified by RT-qPCR experiments (Figure 2E,F). It was also previously described in amoeboid macrophages [29].

After confirming MALAT1 upregulation in amoeboid cells, we went further and investigated whether downregulation of MALAT1 could induce AMT in A375m2 melanoma cells with a well-established amoeboid phenotype [37], and also in A2058 cells, another morphologically amoeboid melanoma cell line. We made use of zinc-finger nucleases that were previously used to knock out MALAT1 in A549 lung cancer cells [34] to deplete MALAT1 in A375m2 and A2058 cells. We obtained 15 clones with decreased MALAT1 expression from both cell lines, although, unlike the A2058 clones, we detected only MALAT1^{+/-} clones in case of A375m2 cells, suggesting that MALAT1 may be indispensable for A375m2 cells but dispensable for A2058 cells. This we derive from the fact that A2058 MALAT1^{-/-} cells do not change their phenotype in 3D, and therefore they may withstand the complete loss of MALAT1 in comparison with A375m2 cells which undergo AMT. In agreement with our previous observations of MAT, A375m2 MALAT1^{+/-} clones were significantly more mesenchymal than control ones (Figure 3C) pointing to a regulatory role of MALAT1 in the amoeboid phenotype. We did not observe any morphological change in A2058 MALAT1^{-/-} clones. However, neither did we see any change in response to ROCK inhibition (Figure S3B), commonly used to induce amoeboid-mesenchymal transition [37,38], suggesting A2058 cells, unlike A375m2 cells, do not exhibit invasive plasticity.

Notably, we detected significantly decreased levels of active RhoA in both A375m2 and A2058 clones with decreased MALAT1 expression (Figures 3D and 4C), which is in agreement with previous studies showing MALAT1 level correlates with the levels of RhoA and Rho kinases 1 and 2 [39,40], which are the key regulators of amoeboid phenotype [38]. Nevertheless, the precise role of MALAT1 in amoeboid phenotype regulation is still to be described. Many signaling pathways shown to be associated with amoeboid phenotype induction were correlated with MALAT1. MALAT1 is upregulated in response to hypoxia [41], which induces the amoeboid phenotype [42]. Interestingly, the third gene upregulated in our data analysis—CEMIP, previously described as a migration-promoting gene, was also shown to be upregulated by hypoxia [31]. Furthermore, MALAT1 might be involved in the regulation of innate immune responses as it was found to regulate the expression of interferon-responsive genes and modulate the activity of the NF- κ B signaling pathway [43,44]. It is of interest that this signaling pathway also regulates amoeboid invasion [45].

Further characterization of clones derived from both amoeboid cell lines revealed that clones with lower level of MALAT1 were significantly more proliferative compared to control ones (Figures 3G and 4D). Additionally, A375m2 MALAT1^{+/-} clones displayed increased invasion. This may be attributed

to their transition to mesenchymal invasion and mechanical properties of the rat tail collagen I which was used in the invasion assays. Rat tail collagen I forms a dense meshwork of thin collagen fibers [46] which can represent a constrictive environment for amoeboid cells but not mesenchymal cells as they actively degrade the ECM to dig their way through it and are not limited by collagen pore sizes.

MALAT1 was also shown in several studies to play a significant role in the process of epithelial to mesenchymal transition (EMT) [47]. EMT is a process during which cells switch into a more pro-invasive mesenchymal phenotype. Further, mesenchymal cells can further switch to the amoeboid phenotype, suggesting MALAT1 as one of the key regulators in the multistep process leading from the epithelial to amoeboid state through EMT and MAT. Unlike our findings, most studies report MALAT1 knockdown to decrease cell proliferation [17,20,21]. We believe that this discrepancy is due to the difference between EMT and MAT processes, and MALAT1 may have different effect on the proliferative ability of mesenchymal and amoeboid cells. The discrepancies may be also due to cell line- or tissue-specific functions of MALAT1 [48,49]. The inconsistent effect of MALAT1 on cell proliferation calls for caution when considering MALAT1 for anti-cancer therapy, as although its downregulation may prevent EMT, it can promote invasion plasticity of individually migrating cells.

Our work is the first to address the role of MALAT1 in MAT/AMT and suggests that increased MALAT1 expression represents a common feature of amoeboid cells. Further studies should be employed to elucidate the molecular mechanisms of the MALAT1 role in amoeboid invasion.

4. Materials and Methods

4.1. Comparison of Public Transcriptomic Data

Three publicly available datasets were used for analysis: GEO accession GSE23764 [28], ArrayExpress accession E-MTAB-6823 (manuscript in revision), and ArrayExpress accession E-MTAB-6643 [29]. Of the GSE23764 series, the subset of data comprising an AMT experiment was used, i.e., data from control samples and samples treated with ROCK kinase inhibitors Y-27632 and H-1152. Differentially expressed genes were identified using limma R package [50]. Only transcripts affected by both inhibitors were selected for subsequent comparisons. RNA-seq data E-MTAB-6823 and E-MTAB-6643 were analyzed for differential gene expression with the limma-voom algorithm [51]. In all cases, transcripts with adjusted p -value ≤ 0.25 were considered differentially expressed. The required minimum fold change was 1.5 in either direction for all the data. The obtained lists of genes were analyzed with Venny 2.1 online tool [52] to find data overlaps.

4.2. Cell Lines, Constructs, and Transfection

A375M2 were a kind gift of Prof. Richard Hynes lab, where this cell line was established. A2058 melanoma cells were purchased from ATCC[®] HTB-43[™] (ATCC, Teddington, UK). MDA-MB-231 cells were obtained from ECACC (ECACC, Salisbury, UK) (#92020424). BLM melanoma cell line was kindly provided by L. van Kempen and J.H.J.M. van Krieken, Department of Pathology, Radboud University, Nijmegen Medical Centre, the Netherlands. HT1080 cell line was obtained from dr. Karel Souček, The Institute of Biophysics, Brno, Czech Republic.

All cell lines were cultivated in DMEM (Dulbecco's Modified Eagle's Medium medium) supplemented by 10% FBS (fetal bovine serum) and 10 $\mu\text{g}/\mu\text{L}$ ciprofloxacin (Sigma, Piscataway, NJ, USA) in humidified atmosphere with 5% CO_2 at 37 °C. The BLM icaRhoA and MDA-MB-231 icaRhoA cell lines were prepared using pLVX Tet-On Advanced Gene expression system (Takara Bio USA, Inc., Mountain View, CA, USA) as described previously [32] (+manuscript in revision).

4.3. MALAT1 Gene Targeting with Zinc Finger Nucleases

A375m2 and A2058 cells were transfected with the ZFN and the homologous recombination construct [34] (see Figure 3A) using PEI transfection reagent (Polysciences, Inc., Warrington, PA, USA); ratio of DNA:PEI was 1:3). Next, EGFP positive cells were sorted into a 96-well plate (1 cell per well) to

obtain individual clones. All grown clones were characterized by PCR genotyping and measuring the expression level of MALAT1.

4.4. Microscopy of Cells

All images of cells were acquired using Nikon ECLIPSE TE2000-S microscope (Nikon, Tokyo, Japan). Images of cells in collagen were taken using Hoffman modulation contrast (10×/0.25 or 20×/0.40 objectives), and of spheroids using 4×/0.13 objective.

4.5. 3D Cell Culture

Cells were brought to suspension, counted, and centrifuged (4 min, 200 rcf, 25 °C). The cell pellets were resuspended, mixed with collagen solution on ice, and plated in wells. After 15 min incubation at 37 °C, the gelled samples were overlaid with cultivation medium containing 1% FBS. The resulting composition of the collagen matrix was 1 mg/mL rat-tail collagen, 1×RPMI medium, 15 mM HEPES, 1% fetal bovine serum, and 50 µg/mL gentamicin. For details about the number of cells and the amount of collagen matrix for respective approaches, see the respective part of the Methods. For induction of inducible constructs (icaRhoA), 250 nM doxycycline (Sigma, Piscataway, NJ, USA) was used. For induction of MAT by dasatinib treatment, 1 µM dasatinib (LC Laboratories, Woburn, MA, USA) was used. The concentration of ROCK inhibitor Y-27632 (Sigma, Piscataway, NJ, USA) was 10 µM.

4.6. Morphology of Cells in 3D Collagen

Cells were seeded into collagen matrix (100,000 cells/250 µL of collagen matrix) and cultivated in wells of a 48-well plate. After 48 h, cells were imaged, and morphology of the cells was analyzed using Fiji software. Cells were considered “elongated” when their length/width ratio was greater than 2, otherwise they were considered “rounded”. A minimum of 400 cells was counted per sample. The data were statistically analyzed using Cochran–Mantel–Haenszel test or logistic regression model and Wald test (in case of MALAT1+/- vs +/+ clone groups analysis). Presented data are summarized from at least 3 independent biological experiments—with the exception of morphology analysis of grouped clones (35 clones derived from A375m2 cells), which was carried out in biological triplicate.

4.7. RNA Isolation

Total RNA was extracted from one million cells cultured in 500 µL of 3D collagen gel for 48 h in a 24-well plate (3D) or a semi-confluent 6 cm Petri dish (2D). In the case of 3D isolation, gels from two wells were added to tubes containing 600 µL RNA extraction solution (60% v/v water-saturated phenol, 3.25 M guanidine thiocyanate, 400 mM sodium acetate buffer pH 4.0, 0.4% w/v N-lauroylsarcosine, 160 mM 2-mercaptoethanol), and 100 µL of 6.1 M sodium chloride. Samples were homogenized using Tissue Tearor (BioSpec Products, Bartlesville, OK, USA). For 2D isolation, 600 µL of above-mentioned RNA extraction solution + 400 µL of RNase-free water was added to the dish, incubated for 1 min, and transferred to a 2 mL tube. The following procedure was the same for both cases. Then, 200 µL of chloroform was added and samples were vortexed vigorously for 10 s. After 10-min incubation at room temperature, samples were centrifuged (18,000× g, 4 °C, 30 min), upper polar phase was transferred to a fresh tube, the volume was adjusted to 800 µL with RNase-free water, and 600 µL of isopropanol was added to precipitate the RNA. Samples were centrifuged at 18,000× g, 4 °C for 10 min, and the resulting pellets were subsequently washed three times with 800 µL of 75% ethanol and air-dried. Finally, RNA was diluted with RNase-free water to final concentration of 0.5 µg/µL.

4.8. Reverse Transcription—Quantitative Polymerase Chain Reaction (RT-qPCR)

The RT-qPCR experiments were performed according to MIQE guidelines [53]. RNA reverse transcription was performed as described previously [29] using 3 µg of total RNA in the total volume of

30 μ L. The qPCR reaction was performed as described previously [29]. For primer details, see Table S1. Cq values were calculated by setting single threshold value for each target (Bio-Rad CFX Manager 3.1). Cq values were exported and relative expression was calculated using qBase+ 3.1 software (Biogazelle, Zwijnaarde, Belgium) [54] and reference gene indexes determined by geNORM analysis for each cell line and treatment (always 2 reference genes; see Table S2). Amplification efficiencies were determined by the standard curve analysis. The obtained data were statistically analyzed in GraphPad Prism 6 (GraphPad Software, Inc., San Diego, CA, USA) using paired two-tailed *t*-test for MAT qPCR analysis (Figure 2E,F and Figure S2) and unpaired two-tailed *t*-test in the case of MALAT1+/- or -/- vs +/- clone groups analysis (Figures 3B and 4A).

4.9. 3D Invasion Spheroid Assay

Cells were grown as spheroids using a 3D Petri Dish[®] (Microtissues[®]); #12-81 large spheroids, (Sigma, Piscataway, NJ, USA) according to manufacturer's protocol for 2 days. The invasion assay was performed in 96-well plates (one spheroid per well, eight technical replicates per sample). Spheroids were embedded into 3D collagen matrix and overlaid with cultivation medium containing 1% FBS. Images of spheroids were taken immediately after embedding into collagen (0 h) and after 48 h (48 h). The area of the spheroids before and after invasion was assessed using Fiji software and the resulting "invasion index" was calculated as the ratio of the area at 48 h/0 h. The data were statistically analyzed in GraphPad Prism 6 using two-way ANOVA. Presented data are summarized from at least 3 independent biological experiments (13–27 individual spheroids per clone).

4.10. Proliferation Assay in 3D Collagen

Cell were seeded into collagen matrix (40,000 cells/100 μ L of collagen matrix; 4 technical replicates per sample) to a 96-well plate, overlaid by DMEM without phenol red containing 1% FBS (100 μ L) and cultivated for 48 h. Collagen without cells served as a blank for the experiment. After 48 h, overlaying medium was replaced by medium containing AlamarBlue reagent (Invitrogen, Carlsbad, CA, USA) in 5:1 ratio and cultivated for another 4 h. Finally, the medium containing AlamarBlue was transferred to new wells and the fluorescence (excitation 550 nm, emission 590 nm) was measured using the Infinite M200 Pro plate fluorimeter (TECAN, Männedorf, Switzerland). At least three independent experiments were performed and at least 3 technical replicates were analyzed per sample. The data were statistically analyzed in GraphPad Prism 6 using two-way ANOVA.

4.11. RhoA-GTP Pulldown Assay

Five clones for respective genotype and cell line chosen for further experiments were pooled (the same number of cells per clone) into "+/+", "+/-", and "-/-" samples. One million cells were cultured in a 500 μ L 3D collagen gel for 48 h in a 24-well plate. Gels from two wells were transferred to tubes containing 500 μ L of 2 \times Triton-X100 lysis buffer (2% Triton X-100, 100 mM Tris, 300 mM NaCl, pH = 7.1, protease inhibitors) and homogenized using Tissue Tearor (BioSpec Products, Bartlesville, OK, USA) on ice. After 10-min centrifugation (18,000 \times g, 10 $^{\circ}$ C), 800 μ L of the solution was transferred to a fresh tube, protein concentration in the lysate was determined using the DCTM Protein Assay (Bio-Rad Laboratories, Hercules, California, CA, USA) and adjusted to the same value in each series with 1 \times Triton X-100 lysis buffer. Then, 50 μ L of the lysate was transferred to a fresh tube (total lysate control) and the rest was incubated with rhotekin-bound GST-beads at 4 $^{\circ}$ C for 45 min. Beads were separated by brief centrifugation and washed two times with 1 \times Triton X-100 lysis buffer. Finally, beads were resuspended in 1 \times Laemmli sample buffer (0.35 M Tris-HCl, pH = 6.8, 10% SDS, 40% glycerol, 0.012% bromophenol blue) with DTT (50 mM) and incubated at 95 $^{\circ}$ C for 10 min. Samples were separated on 10% or 12% SDS-polyacrylamide gels and transferred onto nitrocellulose membrane. Non-specific binding was blocked by incubation of the membranes for 60 min at room temperature in Tris-buffered saline (TBS) containing 4% BSA or 5% non-fat dry milk. The membranes were incubated with a primary antibody in 4 $^{\circ}$ C overnight, washed three times in Tris-buffered saline with Tween-20 (TBST), and

incubated for 75 min with HRP-conjugated secondary antibody at room temperature. Membranes were washed with TBST two times, with TBS one time, and developed using Amersham™ Imager 600 (GE Healthcare, Chicago, IL, USA) and SuperSignal™ Femto Maximum Sensitivity Substrate (Thermo Fisher Scientific, Waltham, MA, USA) or Western Bright TMECL (Advansta, San Jose, CA, USA) HRP substrates. For probing the total protein level after a phosphoprotein detection and for loading control (GAPDH) detection, membranes were stripped in stripping buffer (200 mM NaOH) at 42 °C for 10 min. The primary antibodies used were as follows: GAPDH (Thermo Fisher Scientific MA5-15738), RhoA (Cell Signaling Technology #2117). Quantification of band signals was performed using Multi Gauge software (Fujifilm, Tokyo, Japan). Band intensities of specific proteins were normalized to the GAPDH protein signal. The data were statistically analyzed in GraphPad Prism 6 using *t*-test. The uncropped membranes are available in Figure S4.

5. Conclusions

In conclusion, we have shown that lncRNA MALAT1 might play an important role in amoeboid invasion. We have identified an increased level of MALAT1 in cells undergoing MAT in 3D collagen matrix. Furthermore, decrease of MALAT1 expression in predominantly amoeboid cells led to lowered RhoA activity (which is a well-established characteristic of AMT), an increase in cell proliferation and in A375m2 cell line also to morphologically manifested AMT with increased invasion. This is to our best knowledge the first work that analyses the role of MALAT1 in MAT/AMT.

Supplementary Materials: The following are available online at <http://www.mdpi.com/2072-6694/12/5/1136/s1>, Figure S1: Transcriptomic overlaps of only 3 datasets used for meta-analysis, Figure S2: RT-qPCR analysis of NEAT1 and second pair of primers for MALAT1 in cells undergoing MAT, Figure S3: Complementary RT-qPCR quantification of MALAT1 level in clones derived from A375m2 and A2058 cell lines and quantification of cell morphology of A2058 cells after treatment with Y-27632, Figure S4: Uncropped Western blots used in the study, Table S1: RT-qPCR primers used in the work, Table S2: Reference genes used for respective cell lines in RT-qPCR analysis, File S1: data used for the comparison of transcriptomic profiles.

Author Contributions: Conceptualization, L.M., V.Č. and J.B.; methodology, L.M., A.G. and V.Č.; validation, L.M., A.G. and M.D.; formal analysis, L.M. and V.Č.; investigation, L.M., A.G. and M.D.; writing—original draft preparation, L.M. and A.G.; writing—review and editing, L.M., A.G., V.Č., J.B., D.R., T.G. and S.D.; visualization, L.M.; supervision, J.B. and D.R.; funding acquisition, J.B. and L.M. All authors have read and agreed to the published version of the manuscript.

Funding: This research was funded by the Kellner Family Foundation Principal Investigator Grant and by the Charles University, project GA UK No. 712217.

Acknowledgments: We acknowledge the BIOCEV Gene Core facility.

Conflicts of Interest: The authors declare no conflict of interest.

References

1. Cancer Research UK Worldwide Cancer Statistics. Available online: <https://www.cancerresearchuk.org/health-professional/cancer-statistics/worldwide-cancer#heading-Zero> (accessed on 20 August 2019).
2. Sleeman, J.; Steeg, P.S. Cancer metastasis as a therapeutic target. *Eur. J. Cancer* **2010**, *46*, 1177–1180. [[CrossRef](#)]
3. Paňková, K.; Rösel, D.; Novotný, M.; Brábek, J. The molecular mechanisms of transition between mesenchymal and amoeboid invasiveness in tumor cells. *Cell. Mol. Life Sci.* **2010**, *67*, 63–71. [[CrossRef](#)] [[PubMed](#)]
4. Kosla, J.; Paňková, D.; Plachý, J.; Tolde, O.; Bicanová, K.; Dvořák, M.; Rösel, D.; Brábek, J. Metastasis of aggressive amoeboid sarcoma cells is dependent on Rho/ROCK/MLC signaling. *Cell Commun. Signal.* **2013**, *11*, 51. [[CrossRef](#)] [[PubMed](#)]
5. Pandya, P.; Orgaz, J.L.; Sanz-Moreno, V. Modes of invasion during tumour dissemination. *Mol. Oncol.* **2017**, *11*, 5–27. [[CrossRef](#)] [[PubMed](#)]
6. Lawson, C.D.; Ridley, A.J. Rho GTPase signaling complexes in cell migration and invasion. *J. Cell Biol.* **2018**, *217*, 447–457. [[CrossRef](#)]
7. Brábek, J.; Mierke, C.T.; Rösel, D.; Veselý, P.; Fabry, B. The role of the tissue microenvironment in the regulation of cancer cell motility and invasion. *Cell Commun. Signal.* **2010**, *8*, 22. [[CrossRef](#)]

8. Gandalovičová, A.; Rosel, D.; Fernandes, M.; Veselý, P.; Heneberg, P.; Čermák, V.; Petruželka, L.; Kumar, S.; Sanz-Moreno, V.; Brábek, J. Migrastatics—Anti-metastatic and Anti-invasion Drugs: Promises and Challenges. *Trends Cancer* **2017**, *3*, 391–406. [[CrossRef](#)]
9. Te Boekhorst, V.; Friedl, P. Plasticity of Cancer Cell Invasion—Mechanisms and Implications for Therapy. *Adv. Cancer Res.* **2016**, *132*, 209–264.
10. Wilusz, J.E.; Freier, S.M.; Spector, D.L. 3′ End Processing of a Long Nuclear-Retained Noncoding RNA Yields a tRNA-like Cytoplasmic RNA. *Cell* **2008**, *135*, 919–932. [[CrossRef](#)]
11. Hutchinson, J.N.; Ensminger, A.W.; Clemson, C.M.; Lynch, C.R.; Lawrence, J.B.; Chess, A. A screen for nuclear transcripts identifies two linked noncoding RNAs associated with SC35 splicing domains. *BMC Genom.* **2007**, *8*, 39. [[CrossRef](#)]
12. Ji, P.; Diederichs, S.; Wang, W.; Böing, S.; Metzger, R.; Schneider, P.M.; Tidow, N.; Brandt, B.; Buerger, H.; Bulk, E.; et al. MALAT-1, a novel noncoding RNA, and thymosin β 4 predict metastasis and survival in early-stage non-small cell lung cancer. *Oncogene* **2003**, *22*, 8031–8041. [[CrossRef](#)] [[PubMed](#)]
13. Miyagawa, R.; Tano, K.; Mizuno, R.; Nakamura, Y.; Ijiri, K.; Rakwal, R.; Shibato, J.; Masuo, Y.; Mayeda, A.; Hirose, T.; et al. Identification of cis- and trans-acting factors involved in the localization of MALAT-1 noncoding RNA to nuclear speckles. *RNA* **2012**, *18*, 738–751. [[CrossRef](#)] [[PubMed](#)]
14. Sun, Y.; Ma, L. New Insights into Long Non-Coding RNA MALAT1 in Cancer and Metastasis. *Cancers* **2019**, *11*, 216. [[CrossRef](#)] [[PubMed](#)]
15. Eißmann, M.; Gutschner, T.; Hämmerle, M.; Günther, S.; Caudron-Herger, M.; Groß, M.; Schirmacher, P.; Rippe, K.; Braun, T.; Zörnig, M.; et al. Loss of the abundant nuclear non-coding RNA MALAT1 is compatible with life and development. *RNA Biol.* **2012**, *9*, 1076–1087. [[CrossRef](#)]
16. Zhang, B.; Arun, G.; Mao, Y.S.; Lazar, Z.; Hung, G.; Bhattacharjee, G.; Xiao, X.; Booth, C.J.; Wu, J.; Zhang, C.; et al. The lncRNA Malat1 Is Dispensable for Mouse Development but Its Transcription Plays a cis-Regulatory Role in the Adult. *Cell Rep.* **2012**, *2*, 111–123. [[CrossRef](#)]
17. Arun, G.; Diermeier, S.; Akerman, M.; Chang, K.-C.; Wilkinson, J.E.; Hearn, S.; Kim, Y.; MacLeod, A.R.; Krainer, A.R.; Norton, L.; et al. Differentiation of mammary tumors and reduction in metastasis upon Malat1 LncRNA loss. *Genes Dev.* **2016**, *30*, 34–51. [[CrossRef](#)]
18. Lin, R.; Maeda, S.; Liu, C.; Karin, M.; Edgington, T.S. A large noncoding RNA is a marker for murine hepatocellular carcinomas and a spectrum of human carcinomas. *Oncogene* **2007**, *26*, 851–858. [[CrossRef](#)]
19. Ying, L.; Chen, Q.; Wang, Y.; Zhou, Z.; Huang, Y.; Qiu, F. Upregulated MALAT-1 contributes to bladder cancer cell migration by inducing epithelial-to-mesenchymal transition. *Mol. Biosyst.* **2012**, *8*, 2289–2294. [[CrossRef](#)]
20. Guo, F.; Li, Y.; Liu, Y.; Wang, J.; Li, Y.; Li, G. Inhibition of metastasis-associated lung adenocarcinoma transcript 1 in CaSki human cervical cancer cells suppresses cell proliferation and invasion. *Acta Biochim. Biophys. Sin. Shanghai* **2010**, *42*, 224–229. [[CrossRef](#)]
21. Michalik, K.M.; You, X.; Manavski, Y.; Doddaballapur, A.; Zörnig, M.; Braun, T.; John, D.; Ponomareva, Y.; Chen, W.; Uchida, S.; et al. Long Noncoding RNA MALAT1 Regulates Endothelial Cell Function and Vessel Growth. *Circ. Res.* **2014**, *114*, 1389–1397. [[CrossRef](#)]
22. Han, Y.; Wu, Z.; Wu, T.; Huang, Y.; Cheng, Z.; Li, X.; Sun, T.; Xie, X.; Zhou, Y.; Du, Z. Tumor-suppressive function of long noncoding RNA MALAT1 in glioma cells by downregulation of MMP2 and inactivation of ERK/MAPK signaling. *Cell Death Dis.* **2016**, *7*, e2123. [[CrossRef](#)] [[PubMed](#)]
23. Kwok, Z.H.; Roche, V.; Chew, X.H.; Fadieieva, A.; Tay, Y. A non-canonical tumor suppressive role for the long non-coding RNA MALAT1 in colon and breast cancers. *Int. J. Cancer* **2018**, *143*, 668–678. [[CrossRef](#)] [[PubMed](#)]
24. Gutschner, T.; Hämmerle, M.; Eissmann, M.; Hsu, J.; Kim, Y.; Hung, G.; Revenko, A.; Arun, G.; Stentrup, M.; Gross, M.; et al. The noncoding RNA MALAT1 is a critical regulator of the metastasis phenotype of lung cancer cells. *Cancer Res.* **2013**, *73*, 1180–1189. [[CrossRef](#)] [[PubMed](#)]
25. Schmidt, L.H.; Spieker, T.; Koschmieder, S.; Humberg, J.; Jungen, D.; Bulk, E.; Hascher, A.; Wittmer, D.; Marra, A.; Hillejan, L.; et al. The Long Noncoding MALAT-1 RNA Indicates a Poor Prognosis in Non-small Cell Lung Cancer and Induces Migration and Tumor Growth. *J. Thorac. Oncol.* **2011**, *6*, 1984–1992. [[CrossRef](#)]
26. Huang, J.; Ma, L.; Song, W.; Lu, B.; Huang, Y.; Dong, H.; Ma, X.; Zhu, Z.; Zhou, R. MALAT1 promotes the proliferation and invasion of thyroid cancer cells via regulating the expression of IQGAP1. *Biomed. Pharmacother.* **2016**, *83*, 1–7. [[CrossRef](#)]

27. Kim, J.; Piao, H.L.; Kim, B.J.; Yao, F.; Han, Z.; Wang, Y.; Xiao, Z.; Siverly, A.N.; Lawhon, S.E.; Ton, B.N.; et al. Long noncoding RNA MALAT1 suppresses breast cancer metastasis. *Nat. Genet.* **2018**, *50*, 1705–1715. [[CrossRef](#)]
28. Sanz-Moreno, V.; Gaggioli, C.; Yeo, M.; Albregues, J.; Wallberg, F.; Viros, A.; Hooper, S.; Mitter, R.; Féral, C.C.; Cook, M.; et al. ROCK and JAK1 signaling cooperate to control actomyosin contractility in tumor cells and stroma. *Cancer Cell* **2011**, *20*, 229–245. [[CrossRef](#)]
29. Čermák, V.; Gandalovičová, A.; Merta, L.; Fučíková, J.; Špíšek, R.; Rösel, D.; Brábek, J. RNA-seq of macrophages of amoeboid or mesenchymal migratory phenotype due to specific structure of environment. *Sci. Data* **2018**, *5*, 1–8. [[CrossRef](#)]
30. West, J.A.; Davis, C.P.; Sunwoo, H.; Simon, M.D.; Sadreyev, R.I.; Wang, P.I.; Tolstorukov, M.Y.; Kingston, R.E. The Long Noncoding RNAs NEAT1 and MALAT1 Bind Active Chromatin Sites. *Mol. Cell* **2014**, *55*, 791–802. [[CrossRef](#)]
31. Evensen, N.A.; Li, Y.; Kuscu, C.; Liu, J.; Cathcart, J.; Banach, A.; Zhang, Q.; Li, E.; Joshi, S.; Yang, J.; et al. Hypoxia promotes colon cancer dissemination through up-regulation of cell migration-inducing protein (CEMIP). *Oncotarget* **2015**, *6*, 20723–20739. [[CrossRef](#)]
32. Tolde, O.; Gandalovičová, A.; Křížová, A.; Veselý, P.; Chmelík, R.; Rosel, D.; Brábek, J. Quantitative phase imaging unravels new insight into dynamics of mesenchymal and amoeboid cancer cell invasion. *Sci. Rep.* **2018**, *8*, 12020. [[CrossRef](#)] [[PubMed](#)]
33. Čermák, V.; Gandalovičová, A.; Merta, L.; Harant, K.; Rösel, D.; Brábek, J. High-throughput transcriptomic and proteomic profiling of mesenchymal-amoeboid transition in 3D collagen. *Scientific Data* **2020**. accepted.
34. Gutschner, T.; Baas, M.; Diederichs, S. Noncoding RNA gene silencing through genomic integration of RNA destabilizing elements using zinc finger nucleases. *Genome Res.* **2011**, *21*, 1944–1954. [[CrossRef](#)] [[PubMed](#)]
35. Benbow, U.; Schoenermark, M.P.; Mitchell, T.I.; Rutter, J.L.; Shimokawa, K.I.; Nagase, H.; Brinckerhoff, C.E. A novel host/tumor cell interaction activates matrix metalloproteinase I and mediates invasion through type I collagen. *J. Biol. Chem.* **1999**, *274*, 25371–25378. [[CrossRef](#)] [[PubMed](#)]
36. Petrie, R.J.; Yamada, K.M. Multiple mechanisms of 3D migration: The origins of plasticity. *Curr. Opin. Cell Biol.* **2016**, *42*, 7–12. [[CrossRef](#)]
37. Sahai, E.; Marshall, C.J. Differing modes of tumour cell invasion have distinct requirements for Rho/ROCK signalling and extracellular proteolysis. *Nat. Cell Biol.* **2003**, *5*, 711–719. [[CrossRef](#)]
38. Sanz-Moreno, V.; Gadea, G.; Ahn, J.; Paterson, H.; Marra, P.; Pinner, S.; Sahai, E.; Marshall, C.J. Rac activation and inactivation control plasticity of tumor cell movement. *Cell* **2008**, *135*, 510–523. [[CrossRef](#)]
39. Cai, X.; Liu, Y.; Yang, W.; Xia, Y.; Yang, C.; Yang, S.; Liu, X. Long noncoding RNA MALAT1 as a potential therapeutic target in osteosarcoma. *J. Orthop. Res.* **2016**, *34*, 932–941. [[CrossRef](#)]
40. Wang, Y.; Zhang, Y.; Yang, T.; Zhao, W.; Wang, N.; Li, P.; Zeng, X.; Zhang, W. Long non-coding RNA MALAT1 for promoting metastasis and proliferation by acting as a ceRNA of miR-144-3p in osteosarcoma cells. *Oncotarget* **2017**, *8*, 59417–59434. [[CrossRef](#)]
41. Kölling, M.; Genschel, C.; Kaucsar, T.; Hübner, A.; Rong, S.; Schmitt, R.; Sörensen-Zender, I.; Haddad, G.; Kistler, A.; Seeger, H.; et al. Hypoxia-induced long non-coding RNA Malat1 is dispensable for renal ischemia/reperfusion-injury. *Sci. Rep.* **2018**, *8*, 3438. [[CrossRef](#)]
42. Lehmann, S.; te Boekhorst, V.; Odenthal, J.; Bianchi, R.; van Helvert, S.; Ikenberg, K.; Ilina, O.; Stoma, S.; Xandry, J.; Jiang, L.; et al. Hypoxia Induces a HIF-1-Dependent Transition from Collective-to-Amoeboid Dissemination in Epithelial Cancer Cells. *Curr. Biol.* **2017**, *27*, 392–400. [[CrossRef](#)]
43. Li, J.; Wei, L.; Han, Z.; Chen, Z.; Zhang, Q. Silencing of Long Non-Coding RNA MALAT1 Prevents Inflammatory Injury after Lung Transplant Ischemia-Reperfusion by Downregulation of IL8 through Recruiting p300. *Mol. Ther. Nucleic Acids* **2019**, *18*, 285–297.
44. Zhou, H.-J.; Wang, L.-Q.; Wang, D.-B.; Yu, J.-B.; Zhu, Y.; Xu, Q.-S.; Zheng, X.-J.; Zhan, R.-Y. Long noncoding RNA MALAT1 contributes to inflammatory response of microglia following spinal cord injury via the modulation of a miR-199b/IKK β /NF- κ B signaling pathway. *Am. J. Physiol. Physiol.* **2018**, *315*, C52–C61. [[CrossRef](#)] [[PubMed](#)]
45. Georgouli, M.; Herraiz, C.; Crosas-Molist, E.; Fanshawe, B.; Maiques, O.; Perdrix, A.; Pandya, P.; Rodriguez-Hernandez, I.; Ilieva, K.M.; Cantelli, G.; et al. Regional Activation of Myosin II in Cancer Cells Drives Tumor Progression via a Secretory Cross-Talk with the Immune Microenvironment. *Cell* **2019**, *176*, 757–774. [[CrossRef](#)] [[PubMed](#)]

46. Wolf, K.; Te Lindert, M.; Krause, M.; Alexander, S.; Te Riet, J.; Willis, A.L.; Hoffman, R.M.; Figdor, C.G.; Weiss, S.J.; Friedl, P. Physical limits of cell migration: Control by ECM space and nuclear deformation and tuning by proteolysis and traction force. *J. Cell Biol.* **2013**, *201*, 1069–1084. [[CrossRef](#)] [[PubMed](#)]
47. Chen, M.; Xia, Z.; Chen, C.; Hu, W.; Yuan, Y. LncRNA MALAT1 promotes epithelial-to-mesenchymal transition of esophageal cancer through Ezh2-Notch1 signaling pathway. *Anticancer Drugs* **2018**, *29*, 767–773. [[CrossRef](#)]
48. Gutschner, T.; Hämmerle, M.; Diederichs, S. MALAT1—A paradigm for long noncoding RNA function in cancer. *J. Mol. Med.* **2013**, *91*, 791–801. [[CrossRef](#)]
49. Arun, G.; Spector, D.L. MALAT1 long non-coding RNA and breast cancer. *RNA Biol.* **2019**, *16*, 860–863. [[CrossRef](#)]
50. Ritchie, M.E.; Phipson, B.; Wu, D.; Hu, Y.; Law, C.W.; Shi, W.; Smyth, G.K. Limma powers differential expression analyses for RNA-sequencing and microarray studies. *Nucleic Acids Res.* **2015**, *43*, e47. [[CrossRef](#)]
51. Law, C.W.; Chen, Y.; Shi, W.; Smyth, G.K. voom: Precision weights unlock linear model analysis tools for RNA-seq read counts. *Genome Biol.* **2014**, *15*, R29. [[CrossRef](#)]
52. Oliveros, J.C. Venny 2.1. An Interactive Tool for Comparing Lists with Venn’s Diagrams. Available online: <https://bioinfogp.cnb.csic.es/tools/venny/> (accessed on 1 March 2020).
53. Bustin, S.A.; Benes, V.; Garson, J.A.; Hellemans, J.; Huggett, J.; Kubista, M.; Mueller, R.; Nolan, T.; Pfaffl, M.W.; Shipley, G.L.; et al. The MIQE Guidelines: Minimum Information for Publication of Quantitative Real-Time PCR Experiments. *Clin. Chem.* **2009**, *55*, 611–622. [[CrossRef](#)] [[PubMed](#)]
54. Hellemans, J.; Mortier, G.; De Paepe, A.; Speleman, F.; Vandesompele, J. qBase relative quantification framework and software for management and automated analysis of real-time quantitative PCR data. *Genome Biol.* **2007**, *8*, R19. [[CrossRef](#)] [[PubMed](#)]



© 2020 by the authors. Licensee MDPI, Basel, Switzerland. This article is an open access article distributed under the terms and conditions of the Creative Commons Attribution (CC BY) license (<http://creativecommons.org/licenses/by/4.0/>).

Article

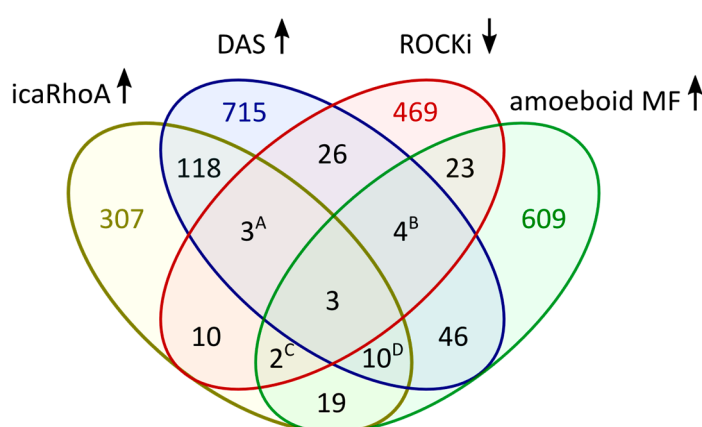
Increased Level of Long Non-Coding RNA MALAT1 is a Common Feature of Amoeboid Invasion

Ladislav Merta, Aneta Gandalovičová, Vladimír Čermák, Michal Dibus, Tony Gutschner, Sven Diederichs, Daniel Rösel and Jan Brábek

Supplementary Materials

A

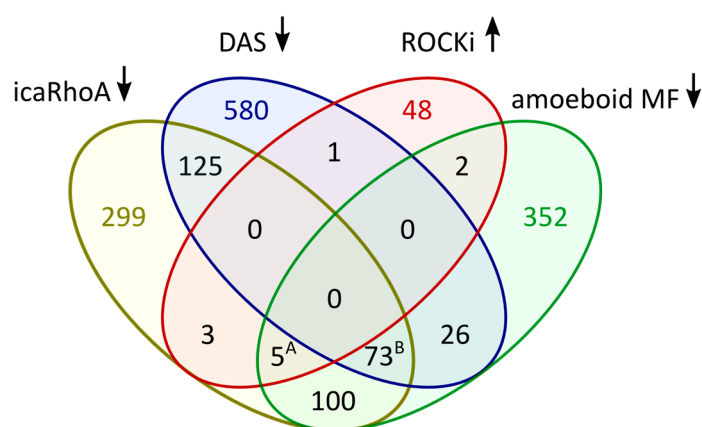
Genes UPREGULATED in amoeboid form



List A:	List B:	List C:	List D:
CPEB4	ITGA1	FSTL1	KYNU
IL24	MMP1	SLAMF7	LAMA1
SLC30A1	NR4A2		MCTP2
	NR4A3		SCG5
			SERPINB2
			SLC12A8
			STC2
			SULT1C2
			TMTC1
			WDR66

B

Genes DOWNREGULATED in amoeboid form



List A:	List B:	List C:	List D:	List E:
BIRC5	ANLN	CEP55	MAD2L1	SGO1
CDCA3	APOBEC3B	CIT	MELK	SKA1
SPC24	BUB1	CKAP2L	MND1	SKA3
TK1	BUB1B	CKS1B	NCAPG	STIL
TROAP	C4orf46	DEPDC1	NDC80	STMN1
	CCNA2	DEPDC1B	NEIL3	TCF19
	CCNB1	DIAPH3	NEK2	TMEM106C
	CCNB2	DLGAP5	NUF2	TMEM97
	CDC25C	DTL	NUSAP1	TPX2
	CDC45	FBXO5	PLK4	TRIP13
	CDC6	GINS2	POLE2	TTK
	CDCA7	HELLS	PRC1	TUBA1A
	CDK1	HJURP	PRIM1	UBE2C
	CDKN3	HMMR	PRR11	UBE2T
	CENPH	IQGAP3	PTTG1	WDR76
	CENPI	KIF15	RAD51	ZNF367
	CENPK	KIF2C	RAD51AP1	
	CENPQ	KNL1	RMI2	
	CENPU	LMNB1	RPA3	

Figure 1. Transcriptomic overlaps of only 3 datasets used for meta-analysis. (A) Venn diagram of gene sets upregulated in the amoeboid HT1080 cells and macrophages, and suppressed in A375m2 cells by ROCK inhibitors (ROCKi). (B) Venn diagram of gene sets downregulated in the amoeboid HT1080 cells and macrophages, and upregulated in A375m2 cells by ROCK inhibitors. Lists of the genes are provided for overlaps of 3 gene sets.

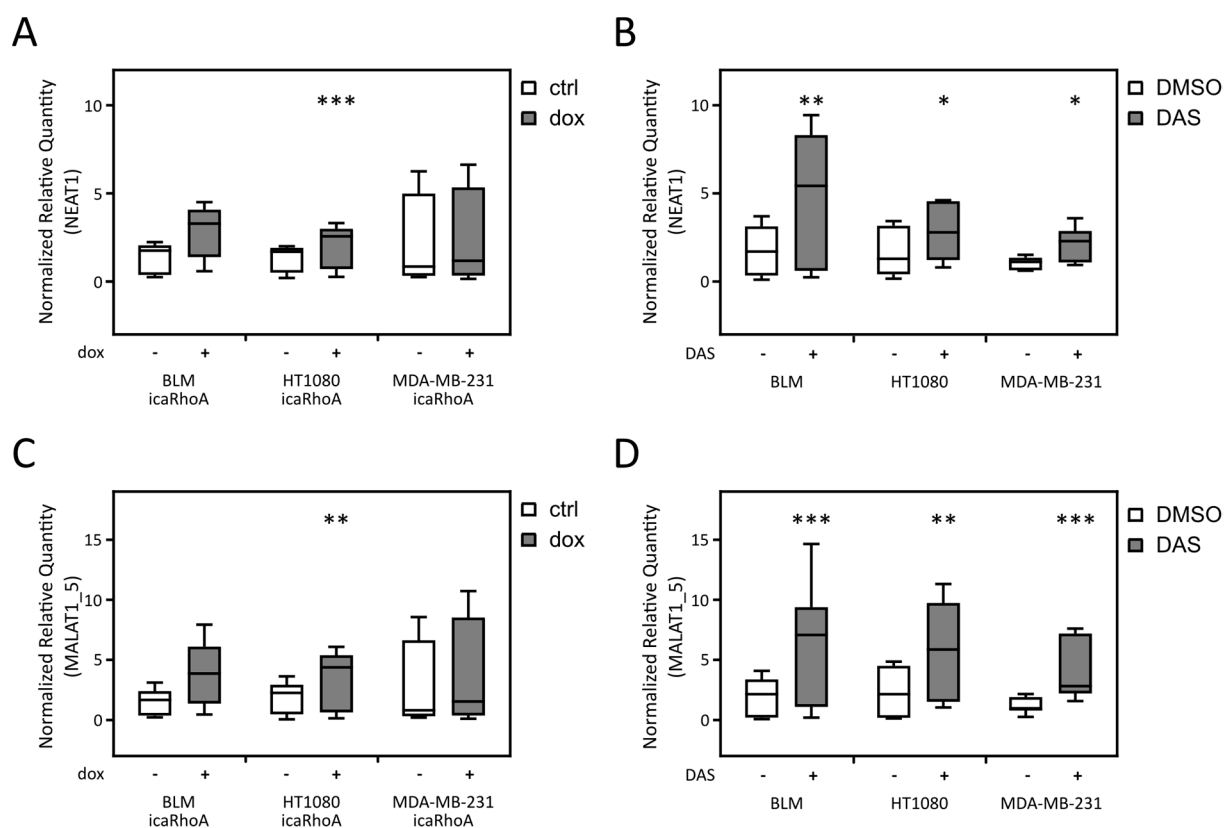


Figure 2. RT-qPCR analysis of NEAT1 and second pair of primers for MALAT1 in cells undergoing MAT. (A-B) Analysis of the NEAT1 gene expression in cells undergoing MAT by induction of constitutively active RhoA (A) or by dasatinib treatment (B). (C-D) Analysis of the MALAT1 gene expression (using primer pair pairing with 5' end of the transcript) in cells undergoing MAT by induction of constitutively active RhoA (C) or by dasatinib treatment (D). Median values are marked in the box plots, whiskers represent min to max value. P-values: *** $p < 0.001$, ** $p < 0.01$, * $p < 0.05$. All data are a representation of at least 3 independent experiments.

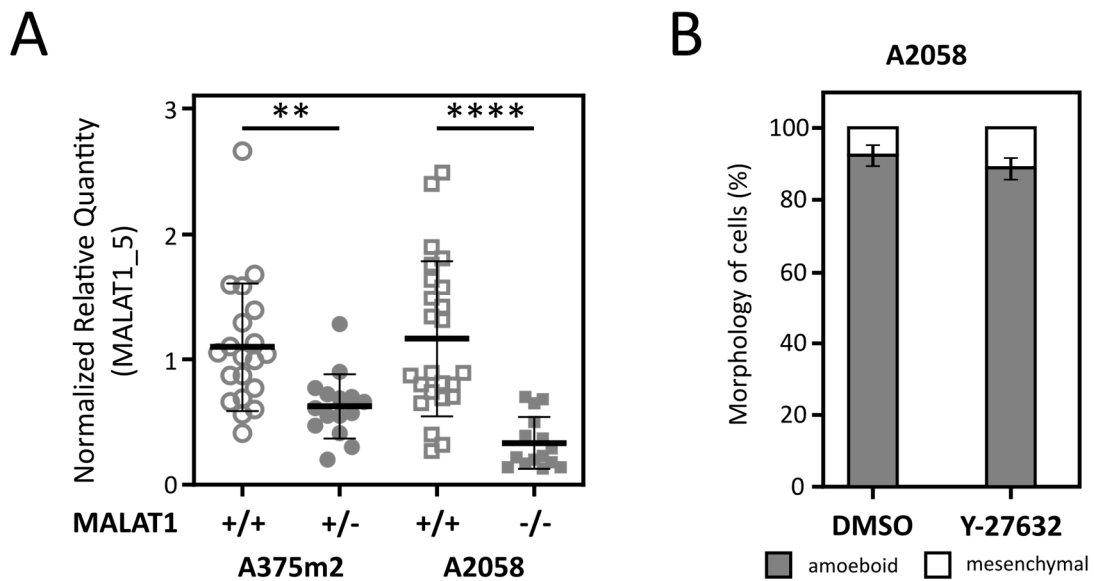


Figure 3. Complementary RT-qPCR quantification of MALAT1 level in clones derived from A375m2 and A2058 cell lines and quantification of cell morphology of A2058 cells after treatment with Y-27632. (A) RT-qPCR analysis of MALAT1 level in clones derived from the A375m2 and A2058 cell lines using second pair of primers pairing with the 5' end of MALAT1 transcript. N(A375m2 MALAT1 +/+) = 20 clones; N(A375m2 MALAT1 +/-) = 15 clones; N(A2058 MALAT1 +/+) = 24 clones; N(A2058 MALAT1 -/-) = 15 clones. Data represent mean \pm SD. (B) morphology of A2058 cells after treatment with ROCK inhibitor Y-27632. Data represent mean \pm SD. P-values: **** $p < 0.0001$, ** $p < 0.01$. All data are a representation of at least 3 independent experiments.

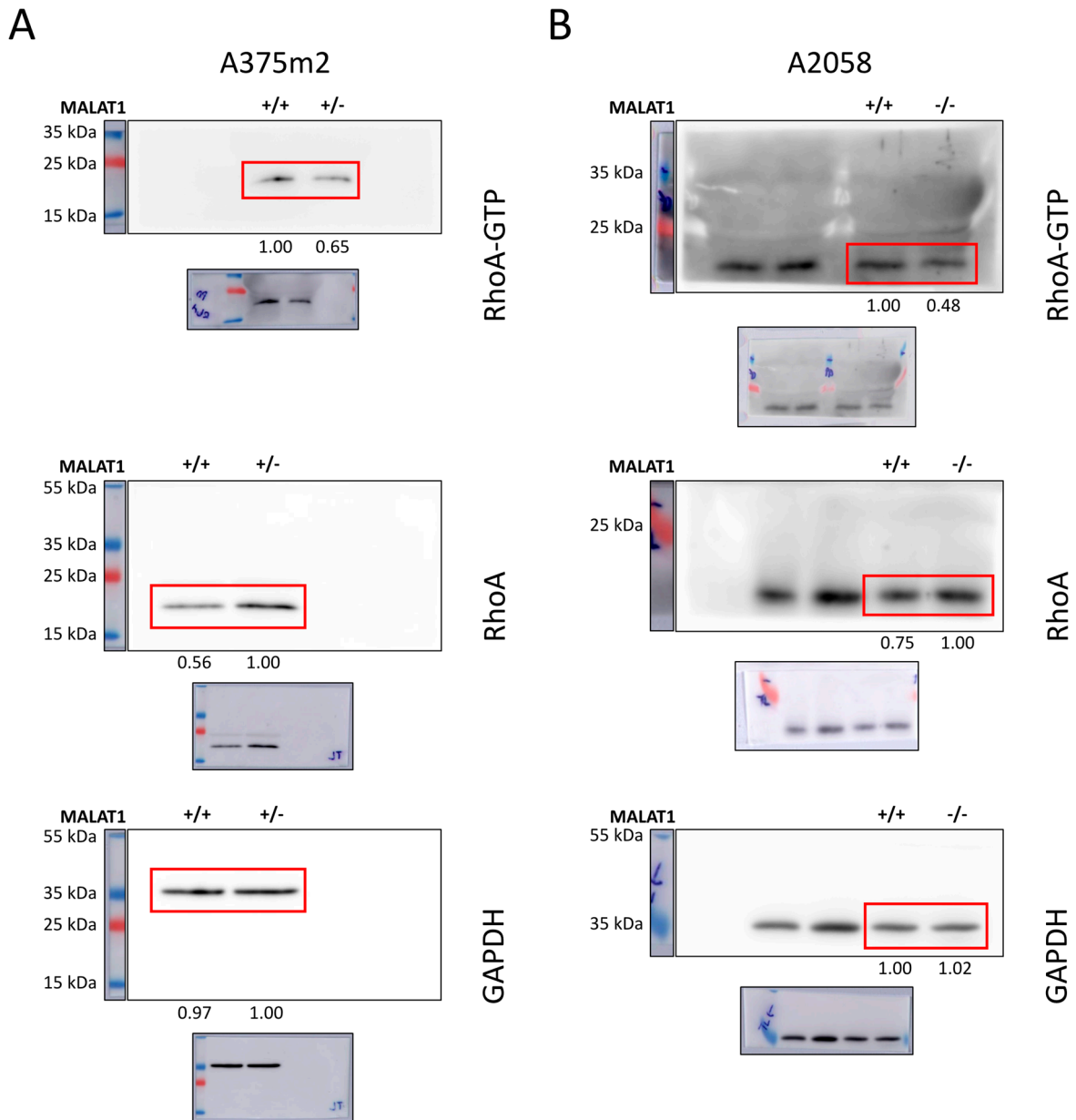


Figure 4. Uncropped Western blots used in the study. (A) Uncropped blots used in Figure 3D. (B) Uncropped blots used in Figure 4C. Red rectangle marks the area presented in the main text. The numbers below the bands represent the intensity ratio. Because the machine used to visualize the blots uses different channels of photo acquisition, each part consists of the HRP signal (the channel from which the cropped images were made) + added marker (upper part) and the whole membrane HRP signal and transmitted light composite channel (lower part).

Table 1. RT-qPCR primers used in the work.

TRANSCRIPT	ACC. NUMBER	PRIMER	SEQUENCE	nt	%GC	T _m (°C)	PRODUCT (bp)	Eff
EIF4H	NM_022170	EIF4Ha	CCTTCTGGCTACGGGAACCAT	21	57.1	63.3	95	1.977
		EIF4Hs	CTTCGACACCTACGACGATCG	21	57.1	63.3		
GAPDH	NM_002046	GAPDH _a	GCATGGACTGTGGTCATGAG	20	55.0	60.5	87	2.012
		GAPDH _s	CTGCACCACCAACTGCTTAG	20	55.0	60.5		
HNRNPL	NM_001533	HNRNPL _a	GCGCTCACTTTTGCCTGAGAA	21	52.4	61.3	96	1.993
		HNRNPL _s	CTGGAGGTGACCGAGGAGAA	20	60.0	62.5		
MALAT1	NR_002819	MALAT1_3 _a	GGTCTGTGCTAGATCAAAAGG	21	47.6	59.4	71	2.010
		MALAT1_3 _s	AAAGCAAGGTCTCCCCACAAG	21	52.4	61.3		
MALAT1_5	NR_002819	MALAT1_5 _a	GTTTCATCCTACCACTCCCAAT	22	45.5	60.3	85	1.992
		MALAT1_5 _s	GAATTGCGTCATTTAAAGCCTA	22	36.4	56.5		
NEAT1	NR_131012	5NEAT1 _f	GTGGTAGGAAATGCAGGTTGA	21	47.6	59.4	122	1.904
		5NEAT1 _r	CCAAGCAACAACCTTAACCAACA	22	40.9	58.4		
PPIA	NM_021130	PPIA _f	GCCGAGGAAAACCGTGACTA	21	52.4	61.3	106	1.941
		PPIA _r	CTGCAAACAGCTCAAAGGAGAC	22	50.0	62.1		
PSMA1	NM_148976	PSMA1 _a	AGACCAACTGTGGCTGAACCT	21	52.4	61.3	95	1.945
		PSMA1 _s	GACAATGATGTCACTGTTGGAG	23	43.5	61.1		

Nt; Number of nucleotides, T_m; Melting temperature, Eff; Amplification efficiency determined by standard curve analysis.

Table 2. Reference genes used for respective cell lines in RT-qPCR analysis.

Cell line/clones derived from cell line	Reference genes
BLM (DMSO/DAS)	EIF4H, GAPDH
BLM icaRhoA (-dox/+dox)	EIF4H, HNRNPL
HT1080 (DMSO/DAS)	EIF4H, GAPDH
HT1080 icaRhoA (-dox/+dox)	EIF4H, GAPDH
MDA-MB-231 (DMSO/DAS)	HNRNPL, PSMA1
MDA-MB-231 (-dox/+dox)	EIF4H, HNRNPL
A375m2 clones	EIF4H, PPIA
A2058 clones	PPIA, PSMA

Tabulka P1 | Primery použité v RT-qPCR experimentech

nt = nukleotidy, T_m = teplota tání, bp = pár bází, Eff = účinnost PCR amplifikace

TRANSKRIPT	REF. SEKVENCE V NCBI	PRIMER	SEKVENCE	nt	%GC	T_m (°C)	PRODUKT (bp)	Eff
C3	NM_000064	C3f	TGTGAGCCAGGAGTGGACTA	20	55,0	60,5	114	2,005
		C3r	ATCCGAGCCTGACTTGATGG	20	55,0	60,5		
CEBPB	NM_005194	CEBPBf	CAAACCAACCGCACATGCAGA	21	52,4	61,3	103	2,064
		CEBPBr	CAGAGGGAGAAGCAGAGAGTTTAT	24	45,8	63,5		
CEBPD	NM_005195	CEBPDf	GCGCGAGCGCAACAACAT	18	61,1	58,4	77	2,034
		CEBPDr	ACTTCTGCTGCATCTCTGGT	21	52,4	61,3		
CEBPG	NM_001806	CEBPGf	GGGCTAGAGGAGCAGGTACAT	21	57,1	63,3	107	1,978
		CEBPGr	GCACTCTCCCTTGCCAACACA	21	57,1	63,3		
DIAPH3	NM_001042517.1	DIAPH3f	ACCGATGCCAAAAGATGTTTCG	21	47,6	59,4	114	1,979
		DIAPH3r	TGTGAACGTGACCCCTTCTGTC	21	52,4	61,3		
EIF4H	NM_022170	EIF4Ha	CCTTCTGGCTACGGGAACCAT	21	57,1	63,3	95	1,977
		EIF4Hs	CTTCGACACCTACGACGATCG	21	57,1	63,3		
FOSL1	NM_005438	FOSL1f	GCCTTGTAACAGATCAGCC	20	55,0	60,5	134	1,939
		FOSL1r	GTTTGTCACTCTCCGCCTG	19	57,9	59,5		
GAPDH	NM_002046	GAPDHa	GCATGGACTGTGGTCATGAG	20	55,0	60,5	87	2,012
		GAPDHs	CTGCACCACCAACTGCTTAG	20	55,0	60,5		
HNRNPL	NM_001533	HNRNPLa	GCGCTCACTTTTGCCTGAGAA	21	52,4	61,3	96	1,993
		HNRNPLs	CTGGAGGTGACCGAGGAGAA	20	60,0	62,5		
IFI6	NM_002038	IFI6f2	GCTGGTCTGCGATCCTGAATG	21	57,1	63,3	101	1,890
		IFI6r2	ATTACCTATGACGACGCTGCTG	22	50,0	62,1		
IL6	NM_000600	IL6f	GTTCTGCAGAAAAAGGCAAAGA	23	43,5	61,1	75	1,999
		IL6r	GTCAGCAGGCTGGCATTGT	20	55,0	60,5		
IL11	NM_000641	IL11f	ATGAACTGTGTTTGCCGCCT	20	50,0	58,4	108	1,912
		IL11r	CCGAGGGTCTGGGGAAACT	19	63,2	61,6		

Tabulka P1 | Primery použité v RT-qPCR experimentech – pokračování

nt = nukleotidy, T_m = teplota tání, bp = pár bází, Eff = účinnost PCR amplifikace

TRANSKRIPT	REF. SEKVENCE V NCBI	PRIMER	SEKVENCE	nt	%GC	T _m (°C)	PRODUKT (bp)	Eff
IL24	NM_006850	IL24f	CCTGTGGACTTTAGCCAGACC	21	57,1	63,3	95	1,951
		IL24r	GCAGGGTAAAACCCAGGCAA	20	55,0	60,5		
ISG15	NM_005101	ISG15f	GAGAGGCAGCGAACTCATCT	20	55,0	60,5	157	2,008
		ISG15r	CTTCAGCTCTGACACCGACA	20	55,0	60,5		
MALAT1	NR_002819	MALAT1_3a	GGTCTGTGCTAGATCAAAAGG	21	47,6	59,4	71	2,010
		MALAT1_3s	AAAGCAAGGTCTCCCCACAAG	21	52,4	61,3		
MALAT1	NR_002819	MALAT1_5a	GTTTCATCCTACCACTCCCAAT	22	45,5	60,3	85	1,992
		MALAT1_5s	GAATTGCGTCATTTAAAGCCTA	22	36,4	56,5		
NEAT1	NR_131012	5NEAT1f	GTGGTAGGAAATGCAGGTTGA	21	47,6	59,4	122	1,904
		5NEAT1r	CCAAGCAACAACCTTAACCAACA	22	40,9	58,4		
NNMT	NM_006169	NNMTf	TTGAAGGGAACAGAGTCAAGGG	22	50,0	62,1	82	1,971
		NNMTTr	GTCACATCACACTTCAGCACC	21	52,4	61,3		
OAS1	NM_016816	OAS1f	CTTTGATGCCCTGGGTCAGTT	21	52,4	61,3	77	1,992
		OAS1r	TGCACTCCTCGATGAGCTTGA	21	52,4	61,3		
POLR2A	NM_000937	POLR2Aa	GTCATTCCACTCCCAACTG	21	52,4	61,3	88	1,941
		POLR2As	GTGGAATCTCTCCTGCCATGA	21	52,4	61,3		
PPIA	NM_021130	PPIAf	GCCGAGGAAAACCGTGTACTA	21	52,4	61,3	106	1,941
		PPIAr	CTGCAAACAGCTCAAAGGAGAC	22	50,0	62,1		
PSMA1	NM_148976	PSMA1a	AGACCAACTGTGGCTGAACCT	21	52,4	61,3	95	1,945
		PSMA1s	GACAATGATGTCCTGTTGGAG	23	43,5	61,1		
STAT1	NM_007315.3	STAT1f	CTGAATTCGGCACCTGCAAT	21	47,6	59,4	84	1,992
		STAT1r	GCTCTTCAGTAACGATGAGAGGA	23	47,8	62,9		

Příloha č. 5 – Geny se zvýšenou/sníženou expresí v buňkách podstupujících mezenchymálně-améboidní přechod

Tabulka P2 | Geny se zvýšenou expresí v buňkách HT1080 podstupujících MAT

Tabulka zachycuje seznam všech genů, jejichž exprese byla signifikantně zvýšena jak při indukci MAT pomocí exprese icaRhoA, tak pomocí přidání dasatinibu. Zeleně jsou zvýrazněny geny, které byly následně analyzovány pomocí RT-qPCR.

Seznam genů se zvýšenou expresí po indukci MAT v buňkách HT1080 expresí icaRhoA i přidáním DAS				
ADAMTS9	COL8A1	IFITM3	NPC1	SLC2A12
ADAR	CPEB4	IL11	OAS1	SLC30A1
AHR	CREG1	IL17RA	OAS2	SP110
AKAP6	DHX58	IL1R1	OAS3	SREBF1
AKR1B1	DTX3L	IL24	OTUD1	SRGN
APOL1	EPAS1	IL6	PARP10	STAT1
ATP6V0A4	ERV3-1	KCNJ2	PARP14	STAT2
BAMBI	FBXO32	LAMA1	PARP9	STC2
BATF2	FTH1	LAP3	PBXIP1	SULT1C2
BCL2L11	FUCA1	LINC01359	PLSCR1	TENT5A
BICC1	GDF15	LINC02015	PRKD2	TGFB2
BST2	GPNMB	LIPH	RASEF	TMEM140
C1R	HELZ2	LOC100506178	RPLP0P2	TMEM86A
C1S	HERC5	LOC644135	RSAD2	TMTC1
C3	HERC6	MALAT1	SAA1	TNFSF13B
CASP1	IFI27	MAP7	SAT1	TRANK1
CASP10	IFI35	MCTP2	SCG5	TRIM38
CCDC30	IFI44L	MT1E	SDC2	USP18
CEBPB	IFI6	MX1	SEMA3B	VASN
CEBPD	IFIH1	MX2	SEMA3F	WDR66
CEMIP	IFIT1	N4BP2L1	SERINC5	ZNF117
CLCA2	IFIT2	NEAT1	SERPINB2	
CLSTN3	IFIT3	NID2	SIDT2	
CMPK2	IFITM1	NLRC5	SLC12A8	
COL4A5	IFITM2	NNMT	SLC22A23	

Tabulka P3 | Geny se sníženou expresí v buňkách HT1080 podstupujících MAT

Tabulka zachycuje seznam všech genů, jejichž exprese byla signifikantně snížena jak při indukci MAT pomocí exprese icaRhoA, tak pomocí přidání dasatinibu. Zeleně jsou zvýrazněny geny, které byly následně analyzovány pomocí RT-qPCR.

Seznam genů se sníženou expresí po indukci MAT v buňkách HT1080 expresí icaRhoA i přidáním DAS

ACTL6A	CIP2A	ITGA6	NUSAP1	SGO2
AKAP12	CIT	IVNS1ABP	OSBPL10	SKA1
ANKRD36	CKAP2L	JUN	OSBPL6	SKA3
ANLN	CKS1B	KCNQ5	PARP2	SLC8A1
ANOS1	CLMP	KHDRBS3	PARPBP	SLF1
ANTXR2	CNTRL	KIAA1549L	PBX3	SMC2
APOBEC3B	CRNDE	KIF14	PCLAF	SMC4
ARHGAP11A	CSE1L	KIF15	PDE5A	SPDL1
ARMC4	DBF4	KIF20B	PLCE1	STAC
ARNTL2	DEPDC1	KIF23	PLEKHA8P1	STIL
ASPM	DEPDC1B	KIF2C	PLK4	STK39
ATAD2	DIAPH3	KIF4A	POLD3	STMN1
ATAD5	DLGAP5	KLF7	POLE2	SVIP
ATP2B4	DPYSL3	KNL1	PRC1	TAGLN3
B4GALT6	DTL	KNTC1	PRDM8	TCF19
BARD1	ECI2	KRT15	PRIM1	TMC7
BLM	ECT2	LAMC2	PRIMPOL	TMEM106C
BRCA1	EME1	LMNB1	PRR11	TMEM97
BRCA2	EMP1	LOXL1-AS1	PSIP1	TMPO
BUB1	ERRF1	LRRC8C	PTTG1	TPX2
BUB1B	ESM1	MAD2L1	RACGAP1	TRHDE
C11orf80	EXOSC8	MANCR	RAD18	TRHDE-AS1
C18orf54	EZH2	MAP1B	RAD51	TRIP13
CAMK4	FANCB	MAST4	RAD51AP1	TTK
CCDC15	FANCD2	MBNL3	RBL1	TUBA1A
CCDC18	FANCI	MCM4	REXO5	TUBA1B
CCNB1	FBXO4	MCM6	RFC4	UBE2C
CCNB2	FBXO5	MCUB	RFC5	UBE2T
CDC45	FOSL1	MELK	RMI2	UBR7
CDC6	FRMD4A	MIR924HG	RPA3	USP1
CDC7	GINS1	MIS18BP1	RRM1	VAT1L
CDCA7	GINS2	MMS22L	RTKN2	VEPH1
CDK1	GPSM2	MND1	S100A10	VRK1
CDKN3	HELLS	NCAPG	S100A2	WDHD1
CENPE	HERC3	NDC80	SACS	WDR76
CENPF	HHIP	NEFL	SAMD5	XRCC2
CENPH	HJURP	NEIL3	SCLT1	YEATS4
CENPI	HMGB1	NEK2	SEMA3D	YWHAH
CENPK	HMGB2	NSD2	SEMA7A	ZGRF1
CENPQ	HMMR	NSMCE4A	SERTAD4	ZNF367
CENPU	IQGAP3	NTNG1	SERTAD4-AS1	ZNF804A
CEP128	ITGA2	NUF2	SFR1	ZWILCH
CEP55	ITGA4	NUP205	SGO1	

Tabulka P4 | Překryv genů se sníženou expresí v buňkách HT1080 podstupujících MAT a améboidní formě makrofágů

Tabulka zachycuje seznam všech genů, jejichž exprese byla signifikantně snížena při indukci MAT pomocí exprese icaRhoA a pomocí přidání dasatinibu v buňkách HT1080 a zároveň v améboidní formě makrofágů.

Seznam genů se sníženou expresí po indukci MAT v buňkách HT1080 expresí icaRhoA i přidáním DAS a zároveň i v améboidní formě makrofágů

ANLN	CENPI	FDFT1	MND1	TCF19
APOBEC3B	CENPK	HJURP	NDC80	TMEM106C
ASPM	CENPQ	HMMR	NEK2	TMEM97
BUB1B	CENPU	IQGAP3	NUF2	TPX2
CCNA2	CEP55	KIF15	PLK4	TRIP13
CCNB1	CIT	KIF2C	PRC1	TTK
CDCA7	CKAP2L	KNL1	PRIM1	TUBA1A
CDK1	DIAPH3	LMNB1	PRR11	UBE2C
CDKN3	DLGAP5	MAD2L1	RAD51AP1	ZNF367
CENPH	DTL	MELK	STMN1	